VILNIUS UNIVERSITY

CENTER FOR PHYSICAL SCIENCES AND TECHNOLOGIES

VILMA VENCKUTĖ

INVESTIGATION OF THE CRYSTAL STRUCTURE, ELEMENTAL COMPOSITION AND PECULIARITIES OF IONIC TRANSPORT IN Li^+ SOLID ELECTROLYTES

Doctoral dissertation

Technological Sciences, Materials Engineering (08T)

Vilnius 2015

The dissertation was prepared at Vilnius University in 2011 – 2015.

Academic supervisor - prof. habil. dr. Antanas Feliksas Orliukas (Vilnius University, technological sciences, materials engineering - 08T).

VILNIAUS UNIVERSITETAS

FIZINIŲ IR TECHNOLOGIJOS MOKSLŲ CENTRAS

VILMA VENCKUTĖ

Li^+ KIETŲJŲ ELEKTROLITŲ KRISTALINIŲ STRUKTŪRŲ, ELEMENTINĖS SUDĖTIES IR JONŲ PERNAŠOS YPATUMŲ TYRIMAS

Daktaro disertacija

Technologijos mokslai, medžiagų inžinerija (08T)

Vilnius 2015

Disertacija rengta 2011 – 2015 metais Vilniaus universitete.

Mokslinis vadovas - prof. habil. dr. Antanas Feliksas Orliukas (Vilniaus universitetas, technologijos mokslai, medžiagų inžinerija – 08T).

Acknowledgements

This work was done in Vilnius University Laboratory of Solid State Ionics, but it wouldn't be possible to complete all the tasks without the help of colleagues in other institutions.

First of all, I would like to thank to my scientific supervisor prof. habil. dr. Antanas Feliksas Orliukas for inveigling me into the field of solid state ionics and his sincere help with all my works in the Laboratory of Solid State Ionics.

Furthermore, sincere gratitude to all colleagues of Laboratory of Solid State Ionics (prof. Algimantas Kežionis, dr. Tomas Šalkus, dr. Edvardas Kazakevičius, Saulius Kazlauskas, Dalius Petrulionis) for interesting discussions, collaboration and friendly atmosphere in the laboratory. I also wish to express my sincere thanks to all collective from Department of Radiophysics for their help and support. Also advices given by the reviewers dr. Bonifacas Vengalis and dr. Robertas Grigalaitis were a great help in improving the dissertation.

I would like to thank dr. Antonija Dindune, dr. Zaiga Kanepe and prof. Kuan-Zong Fung for the materials. Sincere gratitude to dr. Martynas Lelis and dr. Janis Ronis for XRD analysis. Also I would like to thank dr. Vida Kazlauskienė and dr. Juozas Miškinis for XPS spectra. Sincere thanks to dr. Andrius Maneikis for SEM/EDX measurements.

I am particularly grateful to my family for the support and understanding during my PhD studies.

CONTENTS

Abbreviations used in this thesis

DSC: differential scanning calorimetry

EDX: Energy Dispersive X-ray Spectroscopy

IS: Impedance Spectroscopy

LTO: $Li_4Ti_5O_{12}$

LTO+Nb: $Li_4Ti_{4.95}Nb_{0.05}O_{12}$

LTO+Ta: $Li_4Ti_{4.95}Ta_{0.05}O_{12}$

NASICON: Na Superionic Conductor

s. g.: space group

SEM: Scanning Electron Microscopy

TGA: thermogravimetric analysis

XPS: X-ray Photoelectron Spectroscopy

XRD: X-ray Diffraction

1. INTRODUCTION

Solid electrolytes are materials which possess high ionic conductivity due to their crystallographic properties. They are also called fast ion conductors or superionic conductors. Different ions can be mobile in the structure, for example Li^+, Ag^+, Na^+, H^+, F^-, Cl^-, O^{2-}, $V_o^{\bullet\bullet}$ and others. Solid electrolytes can be applied in fuel cells, sensors, batteries and etc.

In this work Li^+ ion conductors, which can be used as functional materials in lithium ion batteries, were investigated. Main parts of lithium ion battery are cathode, anode and lithium solid electrolyte. Materials which are targeted as functional materials for lithium ion batteries must have suitable electrical properties besides their electrochemical properties, stability and etc. Solid electrolyte should be pure lithium ion conductor, whereas cathode and anode should be mixed electronic-ionic conductors. Low electrical conductivity of one of the main parts of the battery can be a limiting factor of batteries operation. So it is very important to find materials with high ionic or mixed ionic-electronic conductivities and to investigate their electrical properties. Electrical conductivity of particular compounds can be increased by composition modification when some ions with a particular valence state in the compound are substituted by various metal ions with different valence state. Electronic part of electrical conductivity can be increased by mixing ionic conductor with compounds, which have high electronic conductivity (for example carbon).

Investigation of the materials by impedance spectroscopy also can give valuable information about the properties of the materials. Electrical conductivity of solid electrolytes usually increases with the temperature according to Arrhenius law. If a material undergoes phase transition or some disordering in the unit cell (for example occupation coefficients of the sites, which are partly or fully occupied by lithium ions, change), anomaly (change)

of activation energy of electrical conductivity can be observed at the transition temperature.

In this work, several groups of materials were synthesized for the investigation. Lithium ion conducting NASICON-type materials are interesting as solid electrolytes for Li ion batteries. Total and bulk conductivity values of $LiTi_2(PO_4)_3$ ceramic are about $2.5 \cdot 10^{-6}$ and $6.3 \cdot 10^{-5}$ Scm^{-1} respectively [1]. In order to increase its electrical conductivity modified NASICON-type compounds $Li_{1+4x}Ti_{2-x}(PO_4)_3$ (x = 0.2, 0.5), $Li_{1.3}Al_yY_{x-y}Ti_{1.7}(PO_4)_3$ (x = 0.3; y = 0.1, 0.2), $Li_{1+4x}Ti_{2-x}Nb_yP_{3-y}O_{12}$ (x = 0.1, 0.2, 0.3 and y = 0, 0.1, 0.2, 0.3) were synthesized. Also several cathode materials for Li ion batteries were prepared. Lately pyrophosphates gain more and more attention as possible cathode materials [2]. In this work $Li_{1-x}Fe_{1-x}Ti_xP_2O_7$ (x = 0, 0.1) and new $Li_{4x}Ti_{1-x}P_2O_7$ (x = 0, 0.06, 0.1, 0.2) pyrophosphates were synthesized. $LiFePO_4$ and $LiFePO_4$/C cathode materials with olivine structure were also synthesized. Spinel $Li_4Ti_5O_{12}$ is a well-known anode material. In order to increase its electronic conductivity Ti can be substituted by different metal ions. In this work $Li_4Ti_5O_{12}$ and $Li_4Ti_{1-x}A_xO_{12}$ (A = Nb, Ta; x = 0, 0.05) were prepared. Electrical properties of the ceramics were investigated by impedance spectroscopy in the frequency range (10 Hz – 3 GHz) and temperature range 300 to 780 K. Two and four-probe methods were employed for electrical properties investigation. Microstructure and elemental composition of the ceramics were investigated by SEM/EDX technique. Surface analysis of the prepared ceramics was conducted by XPS. Crystal structures of the compounds were investigated by XRD.

The **aim** of the dissertation is to prepare Li^+ solid electrolytes and to investigate the relationship between the crystal structure, elemental composition and ionic transport in the prepared materials.

The main tasks of this thesis:

1) To synthesize $Li_{1+4x}Ti_{2-x}(PO_4)_3$, $Li_{1.3}Al_yY_{x-y}Ti_{1.7}(PO_4)_3$, $Li_{1+4x}Ti_{2-x}Nb_yP_{3-y}O_{12}$, $Li_{4x}Ti_{1-x}P_2O_7$, $Li_{1-x}Fe_{1-x}Ti_xP_2O_7$, $Li_4Ti_{5-x}A_xO_{12}$, $LiFePO_4$ and $LiFePO_4$/C powders with different parameters x and y and to prepare ceramics.

2) To investigate crystal structure and microstructure of the prepared ceramics with different stoichiometric parameters.

3) To analyze ceramics surfaces by X-ray photoelectron spectroscopy.

4) To investigate electrical properties of the prepared lithium solid electrolyte ceramics by impedance spectroscopy in the frequency range 10 Hz – 3 GHz and temperature range 300 K – 780 K.

Scientific novelty:

1) For the first time, $Li_{1+4x}Ti_{2-x}(PO_4)_3$ (x = 0.06, 0.1, 0.2) were synthesized by solid state reaction and dependence of their crystal structure on parameter x was investigated.
2) For the first time, Ti^{3+} and Ti^{4+} valence states were detected on the surfaces of $Li_{1+4x}Ti_{2-x}(PO_4)_3$, $Li_{1+4x}Ti_{2-x}Nb_yP_{3-y}O_{12}$, $Li_4Ti_{5-x}A_xO_{12}$ ceramics.
3) For the first time, electrical properties of some NASICON, spinel, pyrophosphate and olivine materials were investigated in the broad frequency range (10 - $3\cdot10^9$) Hz and temperature range (300 – 780) K.
4) For the first time, the influence of partial substitution of P^{5+} by Nb^{5+} in lithium titanium phosphate on the lattice parameters and electrical properties was investigated.

Statements presented for defense:

1) The lattice parameters are changing, but crystal symmetry remains the same, when stoichiometric parameters x and y are varied in

$Li_{1+4x}Ti_{2-x}(PO_4)_3$, $Li_{1.3}Al_yY_{x-y}Ti_{1.7}(PO_4)_3$, $Li_{1+4x}Ti_{2-x}Nb_yP_{3-y}O_{12}$ and $Li_{4x}Ti_{1-x}P_2O_7$ compounds.

2) On the surfaces of $Li_{1+4x}Ti_{2-x}(PO_4)_3$, $Li_{1.3}Al_yY_{x-y}Ti_{1.7}(PO_4)_3$, $Li_{1+4x}Ti_{2-x}Nb_yP_{3-y}O_{12}$ and $Li_4Ti_{5-x}A_xO_{12}$ ceramics titanium exists in Ti^{4+} and Ti^{3+} valence states.
3) The anomalies of activation energy of total conductivity of $Li_{4x}Ti_{1-x}P_2O_7$ (x = 0.06, 0.1, 0.2) and $Li_{1-x}Fe_{1-x}Ti_xP_2O_7$ (x = 0, 0.1) compounds in the temperature range from 520 to 580 K were found and they can be related to disordering in the unit cells.
4) Total and bulk conductivity values and their activation energies of $Li_{1+4x}Ti_{2-x}(PO_4)_3$, $Li_{1.3}Al_yY_{x-y}Ti_{1.7}(PO_4)_3$ and $Li_{1+4x}Ti_{2-x}Nb_yP_{3-y}O_{12}$ change with the variation of stoichiometric parameters x and y in the compounds.

Practical importance of the dissertation:

In this work several new lithium ion conducting materials were synthesized and investigated. Investigated NASICON-type materials can be used as solid electrolytes in lithium ion batteries. Also pyrophosphate and olivine materials can serve as cathode materials. Investigated materials with spinel structure can be used as anode materials.

Authors' contribution

The author of this dissertation has sintered the ceramics, prepared samples for impedance spectroscopy and X-ray photoelectron spectroscopy measurements and carried out the impedance spectroscopy measurements. She has also analyzed the results and prepared manuscripts of most publications. The author has prepared presentations for the conferences and half of them she has presented herself.

A part of the results were obtained in collaboration with partners from other institutions. The synthesis of pyrophosphates, NASICON-type structure materials and $LiFePO_4$/C was conducted in Institute of Inorganic Chemistry,

Riga Technical University (Latvia). $Li_4Ti_{1-x}A_xO_{12}$ and $LiFePO_4$ were synthesized in the Department of Materials Science and Engineering, National Cheng Kung University (Taiwan). Microstructure and elemental composition of the ceramics were investigated in the Semiconductor Physics Institute, Center for Physical Sciences and Technology (Lithuania). Surface analysis of the prepared ceramics was conducted in the Institute of Applied Research, Vilnius University (Lithuania) by XPS. Crystal structures of the compounds were investigated in the Center for Hydrogen Technologies, Lithuanian Energy Institute (Lithuania) and Institute of Inorganic Chemistry, Riga Technical University (Latvia) by XRD.

List of publications on the theme of the thesis:

A1. V. Venckutė, J. Banytė, V. Kazlauskienė, J. Miškinis, T. Šalkus, A. Kežionis, E. Kazakevičius, A. Dindune, Z. Kanepe, J. Ronis, A.F. Orliukas, *Preparation, structure and electrical properties of $Li_{1+4x}Ti_{2-x}Nb_yP_{3-y}O_{12}$ (x = 0.1, 0.2, 0.3; y = 0, 0.1, 0.2, 0.3) ceramics*, Lithuanian Journal of Physics 50 (2010) 435-443.

A2. A.F. Orliukas, T. Šalkus, A. Kežionis, A. Dindune, Z. Kanepe, J. Ronis, V. Venckutė, V. Kazlauskienė, J. Miškinis, A. Lukauskas, *Structure and broadband impedance spectroscopy of $Li_{1.3}Al_yY_{x-y}Ti_{1.7}(PO_4)_3$ (x = 0.3; y = 0.1, 0.2) solid electrolyte ceramics*, Solid State Ionics 225 (2012) 620-625.

A3. A.F. Orliukas, V. Venckutė, J. Miškinis, V. Kazlauskienė, D. Petrulionis, T. Šalkus, A. Dindune, Z. Kanepe, J. Ronis, T. Žukauskas, A. Maneikis, A. Kežionis, *X-ray photoelectron and broadband impedance spectroscopy of $Li_{1+4x}Ti_{2-x}(PO_4)_3$ solid electrolyte ceramics*, Lithuanian Journal of Physics 53 (2013) 244-254.

A4. A.F. Orliukas, K.-Z. Fung, V. Venckutė, V. Kazlauskienė, J. Miškinis, A. Dindune, Z. Kanepe, J. Ronis, A. Maneikis, T. Šalkus, A. Kežionis, *SEM/EDX, XPS and impedance spectroscopy of $LiFePO_4$ and $LiFePO_4$/C ceramics*, Lithuanian Journal of Physics 54 (2014) 106-113.

A5. V. Venckutė, J. Miškinis, V. Kazlauskienė, T. Šalkus, A. Dindune, Z. Kanepe, J. Ronis, A. Maneikis, M. Lelis, A. Kežionis, A.F. Orliukas, *XRD, XPS, SEM/EDX and broadband impedance spectroscopy study of pyrophosphate ($LiFeP_2O_7$ and $Li_{0.9}Fe_{0.9}Ti_{0.1}P_2O_7$) ceramics*, Phase Transitions 87 (2014) 438-451.

A6. V. Venckutė, P. Dobrovolskis, T. Šalkus, A. Kežionis, A. Dindune, Z. Kanepe, J. Ronis, K.-Z. Fung, A.F. Orliukas, *Preparation and characterization of solid electrolytes based on TiP_2O_7 pyrophosphate*, Ferroelectrics, 479 (2015) 101-109.

A7. A.F. Orliukas, K.-Z. Fung, V. Venckutė, V. Kazlauskienė, J. Miškinis, M. Lelis, *Structure, surface and broadband impedance spectroscopy of $Li_4Ti_5O_{12}$ based ceramics with Nb and Ta*, Solid State Ionics 271 (2015) 34-41.

List of other publications:

A8. A.F. Orliukas, T. Šalkus, A. Kežionis, V. Venckutė, V. Kazlauskienė, J. Miškinis, G. Laukaitis, J. Dudonis, *XPS and impedance spectroscopy of some oxygen vacancy conducting solid electrolyte ceramics*, Solid State Ionics 188 (2011) 36-40.

A9. A.F. Orliukas, T. Šalkus, A. Kežionis, A. Dindune, Z. Kanepe, J. Ronis, O. Bohnke, V. Venckutė, M. Lelis, *Structure and electrical properties of $Li_{3-x}Sc_{2-x}Zr_x(PO_4)_3$ (x=0, 0.1, 0.2) ceramics*, Ferroelectrics 418 (2011) 34-44.

A10. A.F. Orliukas, O. Bohnke, A. Kežionis, S. Kazlauskas, V. Venckutė, D. Petrulionis, T. Žukauskas, T. Šalkus, A. Dindune, Z. Kanepe, J. Ronis, V. Kunigėlis, *Broadband impedance spectroscopy of some Li^+ and $V_O^{\bullet\bullet}$ conducting solid electrolyte ceramics*, Advanced Electromagnetics 1 (2012) 70-75.

A11. E. Kazakevičius, T. Šalkus, A. Selskis, A. Selskienė, A. Dindune, Z. Kanepe, J. Ronis, J. Miškinis, V. Kazlauskienė, V. Venckutė, A. Kežionis, A.F. Orliukas, *Preparation and characterization of*

$Li_{1+x}Al_ySc_{x-y}Ti_{2-x}(PO_4)_3$ (x = 0.3, y = 0.1, 0.15, 0.2) ceramics, Solid State Ionics 188 (2011) 73-77.

A12. A.F. Orliukas, E. Kazakevičius, J. Reklaitis, R. Davidonis, A. Dindune, Z. Kanepe, J. Ronis, D. Baltrūnas, V. Venckutė, T. Šalkus, A. Kežionis, *XRD, impedance, and Mossbauer spectroscopy study of the $Li_3Fe_2(PO_4)_3$+Fe_2O_3 composite for Li ion batteries*, Ionics 21 (2015) 2127-2136.

Abstracts in scientific conferences:

C1. V. Venckutė, T. Šalkus, A. Kežionis, E. Kežionis, E. Kazakevičius, A. Dindune, Z. Kanepe, J. Ronis, V. Kazlauskienė, J. Miškinis, A.F. Orliukas, *Structure and electrical properties of $Li_{1.3}Al_{0.3-y}Y_yTi_{1.7}(P_2O_7)_{2.25}$ (y = 0.15, 0.1, 0.2) pyrophosphate in the broadband frequency range*, 39-oji Lietuvos Nacionalinė Fizikos Konferencija, October 6-8, 2011, Vilnius, Lithuania

C2. V. Venckutė, D. Petrulionis, T. Žukauskas, T. Šalkus, A. Dindune, Z. Kanepe, J. Ronis, V. Kazlauskienė, J. Miškinis, A. Kežionis, A.F. Orliukas, *Structure and electrical properties of $Li_{3-4x}Ti_{1,5+x}(PO_4)_3$ (x = 0, 0.1, 0.2, 0.3) compounds in microwave region*, 39-oji Lietuvos Nacionalinė Fizikos Konferencija, October 6-8 , 2011, Vilnius, Lithuania

C3. T. Šalkus, D. Petrulionis, T. Žukauskas, S. Kazlauskas, V. Venckutė, V. Kunigėlis, A. Kežionis, V. Kazlauskienė, J. Miškinis, A.F. Orliukas, *Preparation and investigation of ceramic electrodes for fuel cells*, 39-oji Lietuvos Nacionalinė Fizikos Konferencija, October 6-8 , 2011, Vilnius, Lithuania

C4. A. Orliukas, O. Bohnke, A. Kežionis, S. Kazlauskas, V. Venckutė, D. Petrulionis, T. Žukauskas, T. Šalkus, A. Dindune, Z. Kanepe, J. Ronis, V. Kunigėlis, *Broadband impedance spectroscopy of some Li^+ and $V_O^{\bullet\bullet}$ conducting solid electrolytes*, Advanced Electromagnetic Symphosium AES 2012, April 16-19, 2012, Paris, France

C5. V. Venckute, T. Šalkus, A. Kežionis, A.F. Orliukas, A. Dindune, Z. Kanepe, J. Ronis, *Preparation and characterization of* $Li_{1-x}Fe_{1-x}Ti_xP_2O_7$ *(where x = 0, 0.1) diphosphate ceramics*, 10th International Symposium on Systems with Fast Ionic Transport ISSFIT10, July 1-4, 2012, Chernogolovka, Russia

C6. A.F. Orliukas, V. Venckutė, J. Miškinis, V. Kazlauskienė, D. Petrulionis, T. Šalkus, A. Dindune, Z. Kanepe, J. Ronis, T. Žukauskas, A. Kežionis, *XPS and broadband impedance spectroscopy of* $Li_{1+4x}Ti_{2-x}(PO_4)_3$ *(where x = 0.2, 0.3, 0.4)*, 10th International Symposium on Systems with Fast Ionic Transport ISSFIT10, July 1-4, 2012, Chernogolovka, Russia

C7. A.F. Orliukas, O. Bohnke, M. Barre, V. Venckute, T. Šalkus, D. Petrulionis, A. Kežionis, A. Dindune, Z. Kanepe, J. Ronis, J. Miškinis, V. Kazlauskienė, *XPS and broadband impedance spectroscopy of some Li-ion conducting solid electrolyte ceramics*, 2nd NANOLICOM seminar, October 15-17, 2012, Le Mans, France

C8. V. Venckutė, A. Dindune, Z. Kanepe, J. Ronis, T. Šalkus, A. Kežionis, A.F. Orliukas, *Preparation and characterization of* $Li_{4x}Ti_{1-x}(P_2O_7)$ *(x = 0.06, 0.1, 0.2) ceramics*, 2nd NANOLICOM seminar, October 15-17, 2012, Le Mans, France

C9. A.F. Orliukas, K.-Z. Fung, V. Venckutė, T. Šalkus, D. Petrulionis, A. Kežionis, A. Dindune, Z. Kanepe, J. Ronis, J. Miškinis, V. Kazlauskienė, A. Maneikis, *Surface, Compositions and Electrical Properties of Some Li-ion Conducting Solid Electrolyte Ceramics*, 2012 The First International Workshop on Advanced Li Batteries for Scientific Cooperation between Latvia, Lithuania and Taiwan, November 8, 2012, Tainan, Taiwan

C10. P. Dobrovolskis, V. Venckutė, Electrical properties of $Li_{4x}Ti_{1-x}P_2O_7$ (x=0.06, 0.1) compound ceramics, Open Readings 2013, March 20-22, 2013, Vilnius, Lithuania

C11. A.F. Orliukas, K.-Z. Fung, V. Venckutė, V. Kazlauskienė, J. Miškinis, A. Maneikis, T. Šalkus, A. Kežionis, *SEM/EDX, XPS and impedance spectroscopy of $LiFePO_4$ ceramics*, The 19th International Conference on Solid State Ionics, June 2-7, 2013, Kyoto, Japan

C12. V. Venckutė, T. Šalkus, V. Kazlauskienė, J. Miškinis, A. Kežionis, A. Dindune, Z. Kanepe, J. Ronis, M. Lelis, A. Maneikis, A.F. Orliukas, *Synthesis, structure and broadband impedance spectroscopy of $Li_{4x}Ti_{1-x}P_2O_7$ (x=0, 0.06, 0.1, 0.2) ceramics*, The 19th International Conference on Solid State Ionics, June 2-7, 2013, Kyoto, Japan

C13. V. Venckutė, K.-Z.Fung, V. Kazlauskienė, J. Miškinis, A. Dindune, Z. Kanepe, J. Ronis, A. Maneikis, T. Šalkus, A.Kežionis, A.F. Orliukas, *LiFePO4 keramikų gamyba, XRD, SEM/EDX tyrimai bei XPS ir impedanso spektroskopija*, 40-oji Lietuvos Nacionalinė Fizikos Konferencija, June 10-12, 2013, Vilnius, Lithuania

C14. V. Venckutė, J. Miškinis, V. Kazlauskienė, T. Šalkus, A. Dindune, Z. Kanepe, J. Ronis, A. Maneikis, M. Lelis, A.Kežionis, A.F. Orliukas, *Pirofosfatų ($LiFeP_2O_7$ ir $Li_{0,9}Fe_{0,9}Ti_{0,1}P_2O_7$) keramikų XRD, XPS, SEM/EDX ir impedanso spektroskopijos tyrimai*, 40-oji Lietuvos Nacionalinė Fizikos Konferencija, June 10-12, 2013, Vilnius, Lithuania

C15. P. Dobrovolskis, V. Venckutė, V. Jasulaitienė, V. Kazlauskienė, J. Miškinis, A. Dindune, Z. Kanepe, J. Ronis, A. Maneikis, M. Lelis, T. Šalkus, A.Kežionis, A.F. Orliukas, *Li laidžiųjų pirofosfatų XRD, SEM/EDX, XPS ir jų elektrinės savybės*, 40-oji Lietuvos Nacionalinė Fizikos Konferencija, June 10-12, 2013, Vilnius, Lithuania

C16. D. Baltrūnas, A.F. Orliukas, J. Reklaitis, R. Davidonis, V. Venckutė, *Kai kurių superjonikų tyrimas ^{57}Fe Mesbauerio efektu*, 40-oji Lietuvos Nacionalinė Fizikos Konferencija, June 10-12, 2013, Vilnius, Lithuania

C17. V. Venckutė, K.-Z. Fung, M. Lelis, A. Maneikis, V. Kazlauskienė, J. Miškinis, A. Kežionis, A.F. Orliukas, *XRD, SEM/EDX, XPS and electrical properties investigation of Nb, Ta doped and pure lithium*

titanate, 15th International Conference-School Advanced Materials and Technologies, August 27-31, 2013, Palanga, Lithuania

C18. A. Kežionis, S. Kazlauskas, D. Petrulionis, V. Venckutė, T. Šalkus, E. Kazakevičius, A. Orliukas, *Broadband impedance spectrometry at high temperatures*, Workshop "Superionic Materials for Advanced Applications", October 20-23, 2013, Vilnius, Lithuania

C19. A.F. Orliukas, K.-Z. Fung, G. Bajars, V. Venckutė, A. Kežionis, T. Šalkus, E. Kazakevičius, V. Kazlauskienė, J. Miškinis, A. Maneikis, M. Lelis, *Preparation and characterization of* $Li_4Ti_{5-x}A_xO12$ *(x = 0, 0.05; A = Nb, Ta) ceramics*, Workshop "Superionic Materials for Advanced Applications", October 20-23, 2013, Vilnius, Lithuania

C20. V. Venckutė, M. Lelis, A. Dindune, V. Kazlauskienė, A. Maneikis, Z. Kanepe, J. Ronis, J. Miškinis, T. Šalkus, A. Kežionis, A.F. Orliukas, *Anomalous behaviour of structural and electrical properties of* $LiFeP_2O_7$ *and* $Li_{0.9}Fe_{0.9}Ti_{0.1}P_2O_7$ *pyrophosphates*, Workshop "Superionic Materials for Advanced Applications", October 20-23, 2013, Vilnius, Lithuania

C21. V. Venckutė, A.F. Orliukas, K.-Z. Fung, *Synthesis and characterization of* $Li_{1.3}Al_{0.15}Y_{0.15}Ti_{1.7}(PO_4)_3$ *solid electrolyte*, 16th International Conference – School Advanced Materials And Technologies 2014, August 27-31, 2014, Palanga, Lithuania

C22. A.F. Orliukas, K.-Z. Fung, V. Venckutė, *Structure, surface and broadband impedance spectroscopy of* $Li_4Ti_{5-x}A_xO_{12}$ *(x = 0, 0.05, A = Nb, Ta) ceramics*, 11th International Symposium on Systems with Fast Ionic Transport, June 25-29, 2014, Gdansk-Sobieszewo, Poland

C23. V. Venckutė, A. Dindune, V. Kazlauskienė, M. Lelis, V. Jasulaitienė, A. Kežionis, A.F. Orliukas, *Synthesis and investigation of* $Li_{4x}Ti_{1-x}P_2O_7$ *pyrophosphates*, 11th International Symposium on Systems with Fast Ionic Transport, June 25-29, 2014, Gdansk-Sobieszewo, Poland

C24. V. Venckutė, V. Kazlauskienė, J. Miškinis, A. Dindune, Z. Kanepe, J. Ronis, A. Maneikis, M. Lelis, V. Jasulaitienė, P. Dobrovolskis,

T. Šalkus, A. Kažionis, A.F. Orliukas, *Preparation and characterization of solid electrolytes based on TiP_2O_7 pyrophosphate*, Conference on Application of Polar Dielectrics 2014, July 7-11, 2014, Vilnius, Lithuania

C25. A. Dindune, D. Valdniece, Z. Kanepe, J. Ronis, V. Venckute, A.F. Orliukas, *$Li_{1-x}Fe_{1-x}Ti_xP_2O_7$ (x=0, 0.1) - attractive cathode materials for lithium secondary batteries*, Institute of Solid State Physics University of Latvia - Abstracts of the 30th scientific Conference, February 19-21, 2014, Riga, Latvia

2. OVERVIEW

2.1. Structure and lithium ion transport in NASICON-type solid electrolytes

NASICON - type (*Na^+ superionic conductor*) structure compounds family has greatly increased after discovery of $Na_{1+x}Zr_2P_{3-x}Si_xO_{12}$ by Goodenough et al. in 1976 [3] and now it is one of the best known families of solid electrolytes. The general formulae of NASICON can be written as $AMM'(PO_4)_3$. The A site can be occupied by many different alkali, alkaline earth and other ions or even be empty [4]. M and M' sites can be occupied by di, tri, tetra and penta valent transition metal ions [4]. Due to a wide variety of different NASICON compositions, NASICON compounds can have rhombohedral, monoclinic, triclinic, orthorhombic and other crystal structures [4]. The main feature of NASICON family is the so called "skeleton structure", which consists of rigid negatively charged framework and interstitial space, where the movement of A ions is possible in all three directions [3, 5]. Interstitial space has cavities, which are partly occupied by A ions, and these cavities are interconnected by tunnels. "Bottlenecks" are the narrowest parts of the tunnels. The skeleton structure in $AZr_2(PO_4)_3$ remains rigid with various A ions with different ionic radius, but the unit cell volume increases with increasing ionic radius of A: Li (V = 1518.8 $Å^3$), Na (V = 1530.5 $Å^3$), Ag (V = 1539.8 $Å^3$), K (V = 1566.5 $Å^3$)[5]. In spite of the fact that $NaZr_2(PO_4)_3$ and $LiZr_2(PO_4)_3$ have the same skeleton structure, the room temperature conductivity of $NaZr_2(PO_4)_3$ is about 10^{-7} S/cm [6], while the one of $LiZr_2(PO_4)_3$ is lower than 10^{-9} S/cm [7] The conductivity of $LiZr_2(PO_4)_3$ can be increased by substituting Zr by Ti, which has smaller ionic radii than Zr. The conductivity of $LiZr_{2-x}Ti_x(PO_4)_3$ increases with increasing parameter x and reaches its highest value ($8.5 \cdot 10^{-8}$ S/cm) when x = 1.8 [7]. Subramanian et. al. concludes that conductivity increment is determined by several factors such, as the size of the cavities in which the Li^+ resides; the size of the bottlenecks to

diffusion and the strengths of the Li – lattice oxygen bonds[7]. So by variation of M and M' ion pairs in $AMM'(PO_4)_3$ it is possible to achieve the best skeleton structure for A ions transport.

Aono et al. investigated lithium ion transport peculiarities of solid electrolytes based on Lithium Titanium Phosphate. They continued to investigate relationship between lattice constant and electrical conductivity by changing M and x in $Li_{1+x}M_xTi_{2-x}(PO_4)_3$ (M = Al, Cr, Ga, Fe, Sc, In, Lu, Y, La) [8-11]. Ionic conductivity has increased for all compounds. The authors noticed, that substitution does not occur for the Lu, Y, La ions [8, 9, 11]. The obtained materials was a mix of two phases: $LiTi_2(PO_4)_3$ and $Li_3M_2(PO_4)_3$ (M = Lu, Y, La). The lattice constants of these materials were the same as for pure $LiTi_2(PO_4)_3$, but electrical conductivity had increased [11]. The authors noticed a relationship between pellets porosity and conductivity. The second phase of $Li_3M_2(PO_4)_3$ has lower conductivity, but it increases the sinterability (the capacity to be sintered) of the pellet as the second phase fills the pores. Also it was noticed that all $Li_{1+x}M_xTi_{2-x}(PO_4)_3$ compounds, except with Cr, had porosity lower than 15%, but pure $LiTi_2(PO_4)_3$ had porosity of 34%. Authors concluded that the determinant factor for conductivity increase wasn't the increment of the lattice constant, but rather the higher density of sintered pellets [8, 9, 11].

Kreuer et al. have investigated electrical properties of $Na_{1+x+4y}Zr_{2-y}Si_xP_{3-x}O_{12}$ (x = 0 – 3, y = 0 – 0.2) single crystals and ceramics. They concluded that grain boundaries should have some influence on the electrical properties of the ceramics, as grain boundaries are less densely packed as compared to the grains, and this should influence the activation energy for Na ion transport [12]. Aono et al. have investigated influence of Li_3PO_4 and Li_3BO_3 lithium salts addition to $LiTi_2(PO_4)_3$ on conductivity and sinterability of $LiTi_2(PO_4)_3$. The porosity of $LiTi_2(PO_4)_3$ has decreased with lithium salts addition. The decrement was the most intense up to mole ratio (Li salt/ $LiTi_2(PO_4)_3$) 0.1 [1]. Microstructure of $LiTi_2(PO_4)_3$ with lithium salts had less pores, no cracks and

better interconnection between grains. Also electrical conductivity had increased with the addition of lithium salts. It was noticed that total conductivity was almost the same as grain boundary conductivity, which is lower than grain conductivity, therefore total conductivity was determined by grain boundary conductivity. The activation energy of grain boundaries has decreased with the addition of lithium salts, while the activation energy for grains remained the same as for pure $LiTi_2(PO_4)_3$. This showed that lithium salts were in grain boundaries and didn't react with $LiTi_2(PO_4)_3$ during the synthesis. However the grain conductivity itself also increased with the addition of lithium salts in a similar manner as grain boundary conductivity. This hinted the authors at the idea that conductivity in the grains depends on the conductivity grain boundaries. Two grains are connected through grain boundary, so an ion migrating from one grain to another neighboring grain has to pass through grain boundary, hence grain boundary conductivity becomes a limiting factor for conductivity in the grains [1].

Optimal microstructure for a particular composition can be obtained by choosing synthesis route and sintering conditions. Kang and Cho investigated the effect of sintering conditions on the properties of $Na_3Zr_2Si_2PO_{12}$ and $Na_{3.2}Zr_{1.3}Si_{2.2}P_{0.8}O_{10.5}$. These compounds normally contain certain amounts of ZrO_2 second phase. The density of the samples sintered between 1160°C and 1360°C for 1 h increased with increasing sintering temperature. Relative density variation with sintering time was also investigated. The relative density of $Na_3Zr_2Si_2PO_{12}$ sintered at 1280°C increased with sintering time and reached its maximum value after 8 hours and then exhibits little change with time. Meanwhile the relative density of $Na_{3.2}Zr_{1.3}Si_{2.2}P_{0.8}O_{10.5}$ sintered at 1300°C reached its maximum value after 2 h and even lowered with longer sintering times. The electrical conductivity was higher in denser samples [13]. Fuentes et al. have investigated influence of sintering conditions on the properties of $Na_3Si_2Zr_{1.88}Y_{0.12}PO_{12}$ ceramics. One series of samples was sintered in air during 10 h for different temperatures between 1190°C and 1235°C and second

series of samples was sintered at 1220°C for 2, 10, 40 and 80 h. Even so grain size distribution was significant, the average grain sizes increased with increasing sintering temperature and increasing sintering time. SEM micrographs showed liquid phase in samples sintered for 80 h, but lower amounts of liquid phase could also be present in samples sintered for shorter times. Electrical properties investigation showed only small variations of grain conductivity with varying sintering conditions. Clear minima were present in grain boundary resistivity dependences on sintering temperature or sintering time. At first the resistivity of grain boundaries decreases with increasing sintering temperature, as density of the ceramics and grain sizes increase. Further increment of sintering temperature causes segregation of resistive zirconia liquid phase, which increases resistivity of grain boundaries. Some increment of grain resistivity is visible, which is due to Zr-deficiency in the grains. The resistance of grain boundaries dependence on sintering time exhibit a minimum, which can be explained analogously [14]. Kosova et al. investigated electrical properties of $LiTi_2(PO_4)_3$ and $Li_{1.3}Al_{0.3}Ti_{1.7}(PO_4)_3$ obtained by means of solid-phase synthesis from the activated and non-activated mixtures of initial reagents. Ceramics were sintered at 800°C, 900°C and 1000°C for 4 h. Electrical conductivity values at 25°C for both mechanically activated and non-activated samples were higher for ceramics sintered at temperature 800°C than for ceramics sintered at 900°C, but further increment of sintering temperature to 1000°C has determined lower values of electrical conductivity. Also conductivity values were highly enhanced for the mechanically activated samples compared with non-activated ones: the conductivity values of $LiTi_2(PO_4)_3$ sintered at 900°C for mechanically activated and non-activated samples were $2.0 \cdot 10^{-5}$ and $3.6 \cdot 10^{-8}$ S/cm respectively and the electrical conductivity values of $Li_{1.3}Al_{0.3}Ti_{1.7}(PO_4)_3$ sintered at 900°C for mechanically activated and non-activated samples were $6.2 \cdot 10^{-5}$ and $3.4 \cdot 10^{-7}$ S/cm respectively [15]. Also mechanical activation has determined lower activation energy of electrical conductivity. Authors suggested, that the reasons for electrical conductivity improvement by

mechanical activation could be the decrease in the concentration of dielectric impurities in the surface layer, an increase in the number of contacts between the particles, an increase in concentration and acceleration of the diffusion of lithium ions in the sub-surface layer due to an increase in vacancy disordering [15]. One of the modern ways to modify ceramics microstructure is spark plasma sintering [16, 17]. Chang et al. compared $LiTi_2(PO_4)_3$, $Li_{1.3}Al_{0.3}Ti_{1.7}(PO_4)_3$ and $Li_{1.3}Al_{0.3}Ti_{1.7}(PO_4)_{2.9}(VO_4)_{0.1}$ ceramics sintered by conventional sintering and spark plasma sintering methods. The densities of ceramics were greatly improved for ceramics sintered by spark plasma sintering. For example, the relative densities of $LiTi_2(PO_4)_3$ ceramics sintered by conventional sintering and spark plasma sintering were ~76% and ~94% respectively. Electrical conductivities of $Li_{1.3}Al_{0.3}Ti_{1.7}(PO_4)_3$ and $Li_{1.3}Al_{0.3}Ti_{1.7}(PO_4)_{2.9}(VO_4)_{0.1}$ were higher by one order of magnitude than in $LiTi_2(PO_4)_3$. This has shown, that densification can't be the only factor , which determines electrical conductivity, but also bottleneck size variation by ion substitution in $LiTi_2(PO_4)_3$ [17].

2.2. The dominant crystal structures and phase transitions in Li^+ conducting pyrophosphates

Pyrophosphates gain more and more interest as potential cathode materials for lithium ion batteries. One of the attractions is a promise of high redox potential of pyrophosphate compounds. For example, it was shown that $Li_{2-x}CoP_2O_7$ electrode is electrochemically active with a redox potential of 4.9 V [18]. Robust structure composed of P_2O_7 diphosphate units' grants good chemical and thermal stability. Furthermore pyrophosphates are easy to prepare by conventional solid-state synthesis [2].

Both lithium iron pyrophosphates with divalent ($Li_2Fe(II)P_2O_7$) and trivalent ($LiFe(III)P_2O_7$) iron have gained attention as a possible cathode material for lithium ion batteries. $LiFeP_2O_7$ has 113 mAh/g theoretical capacity [19]. One of the advantages of lithium iron phosphates is low cost. Padhi et al.

have investigated electrochemical properties of several lithium iron phosphates, including $LiFeP_2O_7$. Fe^{3+}/Fe^{2+} redox couple in $LiFeP_2O_7$ was located at 2.9 eV below the Fermi level of lithium giving cell voltage of 2.9 V. $LiFeP_2O_7$ had specific capacity of ~50 mAh/g [20]. Wurm et al. have also reported of not being able to obtain more than 65% (~73 mAh/g) of theoretical capacity [19]. $Li_2FeP_2O_7$ was reported to have 110 mAh/g theoretical capacity [21]. Different authors managed to obtain the reversible capacity of 85 mAh/g [22] and 100 mAh/g [18].

The crystal structure of $Li_2Fe(II)P_2O_7$ and $LiFe(III)P_2O_7$ is different. The lattice parameters of both lithium iron pyrophosphates and some isostructural compounds obtained by different authors are summarized in Table 2.2.1. $LiFeP_2O_7$ belongs to monoclinic symmetry (S.g. $P2_1$). The framework is built of corner-sharing FeO_6 octahedra and P_2O_7 groups. Lithium cations reside in the interstitial space. The structure of $LiFeP_2O_7$ is shown in Figure 2.2.1 [19, 23]. Other pyrophosphate compounds, as $LiInP_2O_7$ [24], $LiVP_2O_7$ [25] and $LiScP_2O_7$ [26] are known to be isotructural with $LiFeP_2O_7$.

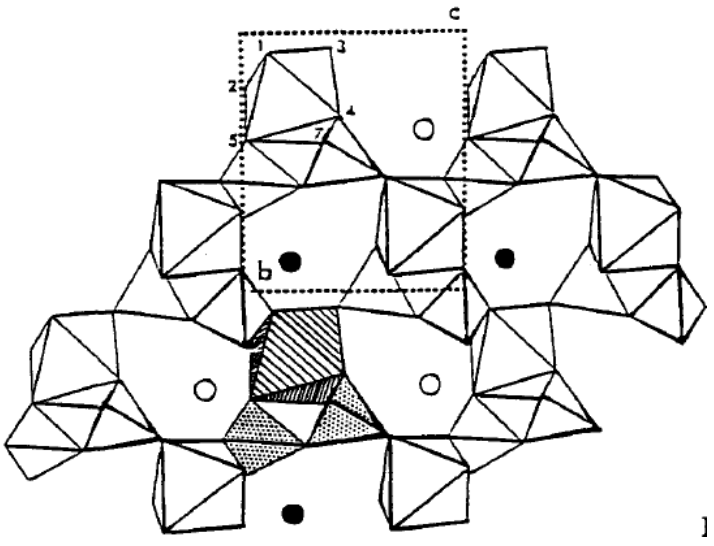

Figure 2.2.1 Structure of $LiFeP_2O_7$ [23].

$Li_2FeP_2O_7$ has a very similar structure as $Li_2MnP_2O_7$. Adam et al. have reported, that $Li_2MnP_2O_7$ crystallizes in the monoclinic space group $P2_1/a$ [27]. $Li_2FeP_2O_7$ was reported to crystallize in the monoclinic space group $P2_1/c$

(Nishimura et. al. [21]) or $P2_1/a$ (Zhou et. al. [22]). MO_6 (M = Mn, Fe) octahedron and MO_5 pyramid share a common edge to form M_2O_9 unit. The framework is built of M_2O_9 units connected by P_2O_7 units. Lithium ions are located in the tunnels of this framework [21, 27]. All compounds in the system $Li_2Mn_{1-y}Fe_yP_2O_7$ (y = 0, 0.2, 0.5, 0.8, 0.9, 1), which were reported by Zhou et al., belong to monoclinic system space group $P2_1/a$. Gradual decrease of lattice parameters a and c was observed with increasing iron content up to 80%. Sharp decrease in the lattice parameters a, b and c were observed above 80% of iron content. High-energy synchrotron XRD analysis showed that system crystallizes in the same space group $P2_1/a$ irrespective of iron content. However, MO_6 octahedrons are more symmetric and M-O bonds are slightly shorter in $Li_2FeP_2O_7$ than in $Li_2MnP_2O_7$ [22].

Tamaru et al. have prepared $Li_2FeP_2O_7$ (discharged state) by conventional solid-state synthesis. To obtain $LiFeP_2O_7$ (charged state) samples were placed in acetonitrile (CH_3CN) with NO_2BF_4 as oxidizer. Oxidation reaction can be written as follows: $Li_2FeP_2O_7 + NO_2BF_4 \rightarrow LiFeP_2O_7 + LiBF_4 + NO_2$. The reduction reaction can be carried out with LiI as reductant. This reaction can be written as follows: $LiFeP_2O_7 + x(3/2)LiI \rightarrow Li_{2-x}FeP_2O_7 + x(1/2)LiI_3$. DSC results of $LiFeP_2O_7$ obtained from chemical oxidation show two exothermic peaks at 250°C and 540°C. TGA shows no weight loss at these temperatures. Thermal in situ XRD analysis shows, that $LiFeP_2O_7$ below 250°C belongs to $P2_1/c$ symmetry. In the temperature range 250-450°C peaks in the XRD patterns start to broaden, showing intermediate phase. New peaks start to emerge around 540°C. This transformation ends at around 600°C. High temperature phase of $LiFeP_2O_7$ belongs to $P2_1$ symmetry [28]. Kim et al. have obtained similar result: DSC of chemically delithiated $LiFeP_2O_7$ show high exothermal peak above 510°C [18].

Despite of growing interest in pyrophosphate compounds, the literature on their electrical properties is still slender. Vitinš et al. have reported investigation of electrical properties of $LiFeP_2O_7$ in the temperature range 200-

720°C and in the frequency range 100 Hz to 20 MHz. Anomaly of activation energy of conductivity is observed at 417°C. At this temperature the activation energy of conductivity reduces from 1.23 to 0.80 eV. Besides DTA analysis doesn't show any thermal effects at this temperature [26].

Investigation of $LiTiP_2O_7$ single crystal by XRD has shown that it is isostructural with $LiFeP_2O_7$. $LiTiP_2O_7$ crystallize in monoclinic symmetry (s.g. $P2_1$) (see Table 2.2.1) [29]. On the other hand, TiP_2O_7 crystallizes in cubic symmetry (s.g. $Pa\bar{3}$) with 3×3×3 superstructure. The framework is built up from cornersharing TiO_6 octahedra and P_2O_7 groups. P_2O_7 groups are formed from PO_4 tetrahedra [30, 31].

TiP_2O_7 initially has no lithium ions in the structure. So at first lithium has to be inserted into the structure for electrochemical properties investigation. Li/TiP_2O_7 cell showed voltage of around 2.6 V and the discharge capacity for the first cycle was 95 mAh/g [30]. This is about 79% of theoretical capacity, which is 121 mAh/g [32].

Chernorukov et al. have reported that TiP_2O_7 undergoes phase transition from cubic α-phase (a = 23.52 Å) to cubic β-phase (a = 7.80 Å) at 730°C [33, 34]. This phase transition from the superstructure to small cubic structure is also typical for other AB_2O_7 materials [31]. Kim and Yim also have found dielectric phase transitions at about 200-300°C and 600°C in TiP_2O_7.The angle change of P-O-P components was suggested as a possible explanation for the dielectric transition at 200-300°C [35]. Electrical properties investigation has shown that TiP_2O_7 is almost pure proton conductor. The proton conductivity of TiP_2O_7 at 900°C in wet atmosphere was found to be $5 \cdot 10^{-4}$ S/cm. The temperature dependences of TiP_2O_7 conductivity show bends at ~695°C. These bends indicate phase transition in the material and they probably can be related with the same phase transitions that were reported by Chernorukov et al. [34, 36].

Table 2.2.1 Lattice parameters of some pyrophosphates.

Compound	Space group	a, Å	b, Å	c, Å	β	V, Å^3	Ref.
$LiFeP_2O_7$	$P2_1$	4.825(1)	8.079(2)	6.938(2)	109.38(2)	255.14	[37]
$LiFeP_2O_7$	$P2_1$	4.8229(2)	8.0813(5)	6.9419(6)	109.39	255.22(4)	[23]
$LiInP_2O_7$*	$P2_1$	7.084(2)	8.436(2)	4.908(3)	110.75(2)	274.3(1)	[24]
$LiVP_2O_7$	$P2_1$	4.8102(7)	8.1208(5)	6.9465(10)	109.006(10)		[25]
$Li_2FeP_2O_7$	$P2_1/c$	11.01847(4)	9.75536(3)	9.80517(3)	101.5416(2)	1033	[21]
$Li_2MnP_2O_7$	$P2_1/a$	9.8941(6)	9.8111(1)	11.1597(8)	102.48	1057.7	[22]
$Li_2MnP_2O_7$	$P2_1/a$	9.8945(1)	9.8113(1)	11.1596(1)	102.485(1)		[27]
$Li_2MnP_2O_7$*	$P2_1/a$	9.9158(6)	9.8289(6)	11.1800(7)	102.466(5)	1063.9(1)	[27]
$LiTiP_2O_7$	$P2_1$	4.8882(10)	8.209(2)	6.9550(10)	108.80(3)	264.18(9)	[29]
TiP_2O_7	Pa	23.626(4)					[30]
TiP_2O_7	Pa	23.5340(5)					[31]

* - data for single crystal

2.3. Peculiarities of structure and electrical properties of Spinel-type LTO and LTO based materials

It is known, that $Li_4Ti_5O_{12}$ is a suitable material for the anodes of lithium ion batteries. It has a theoretical capacity of 175 mAh/g [38]. The experimental capacity varies in the range 150-160 mAh/g [38-40]. $Li_4Ti_5O_{12}$ is a zero-strain insertion material. This means that the lattice parameter does not change during the insertion/extraction of lithium ions. The lattice parameter remained the same within an experimental error (a = 8.370±0.005Å) for samples having different degrees of reduction ranging from x = 0 to x = 0.91. The absence of dimensional changes in the unit cell would also prevent electrode crumbling and particle fracture in the battery [39].

$Li_4Ti_5O_{12}$ is a spinel-type material. It belongs to cubic symmetry with space group $Fd\bar{3}m$. At room temperature three-fourths of the Li^+ ions fully occupy tetrahedral 8a positions. One-fourth of the Li^+ ions and all Ti^{4+} ions occupy octahedral 16d positions. This can be written as $(Li)_{8a}[Li_{1/3}Ti_{5/3}]_{16d}O_4$. Upon heating redistribution of Li^+ ions in the structure starts and $Li_4Ti_5O_{12}$ undergoes two successive order-disorder phase transitions. Li^+ ions transfer from 8a positions to 16c positions and so vacancies in 8a positions are formed, allowing situation $[Li□]_{16c}[Li_{1/3}Ti_{5/3}]_{16d}O_4$, where □ denotes vacancies. Formation of vacancies determines increase in conductivity above 450 K. Another drastic increase of electrical conductivity is observed above 800 K. It is a subsequence of the transfer of Li^+ ions from 16d positions to vacant 16c positions ($[Li_{4/3}□_{2/3}]_{16c}[Ti_{5/3}□_{1/3}]_{16d}O_4$) [41, 42].

$Li_4Ti_5O_{12}$ is a lithium ion conductor with a very low electronic conductivity [42, 43]. As has been mentioned, it undergoes several phase transitions in the temperature range 300 – 1230 K. The results of Leonidov et al. has shown show 4 abrupt changes of activation energy of electrical conductivity at around 460 K, 560 K, 800 K and 1100 K [42]. Fehr et al. have distinguished two slope changes in the temperature dependences of the

conductivity in the temperature range 300 K to 690 K at about 580 K and 690 K. The activation energies for the three sections were 1.35 eV (475-605 K), 0.54 eV (605-715 K) and 0.98 eV (715-960 K). The authors have also pointed out, that big differences between conductivities obtained by different authors can be influenced by experimental conditions, as not all the authors mention heating and cooling rates during electrical measurements [41].

Insulating properties of $Li_4Ti_5O_{12}$ is important drawback for its application as anode in lithium ion batteries. Doping of Ti, O or Li sites by different metal ions was chosen as one of the ways to increase electronic conductivity of $Li_4Ti_5O_{12}$ [44]. Wolfenstine and Allen have investigated electrical properties of $Li_4Ti_5O_{12}$ and $Li_4Ti_{4.95}Ta_{0.05}O_{12}$ sintered in air (oxidizing) or 3vol.% H_2/Ar (reducing) atmosphere. $Li_4Ti_5O_{12}$ and $Li_4Ti_{4.95}Ta_{0.05}O_{12}$ ceramics sintered in air were predominately ionic conductors and ionic conductivities at room temperature of both compounds were about $3 \cdot 10^{-8}$ Scm^{-1}. Electronic conductivities for $Li_4Ti_5O_{12}$ and $Li_4Ti_{4.95}Ta_{0.05}O_{12}$ ceramics sintered in air were $8 \cdot 10^{-10}$ Scm^{-1} and $1 \cdot 10^{-9}$ Scm^{-1} respectively. Ceramics sintered in reducing atmospheres were mixed ionic and electronic conductors. Under reducing conditions some of the Ti^{4+} ions were reduced to Ti^{3+} ions to compensate for extra charge of Ta^{5+} ions in $Li_4Ti_{4.95}Ta_{0.05}O_{12}$. In consequence of the increased number of electrons, the electronic conductivity is increased and it is equal to $1 \cdot 10^{-3}$ Scm^{-1}. In case of $Li_4Ti_5O_{12}$ some of Ti^{4+} ions were reduced to Ti^{3+} ions under reducing atmosphere too. Oxygen vacancies are generated to compensate charges. Electronic conductivity for $Li_4Ti_5O_{12}$ was $2 \cdot 10^{-5}$ Scm^{-1} [45].

2.4. **Structure and electrical properties of $LiFePO_4$**

$LiFePO_4$ has olivine crystal structure orthorhombic symmetry with space group Pnma. Olivine crystal structure is shown in Figure 2.4.1. M_2XO_4 olivine structure is composed of MO_6 - octahedra and XO_4 - tetrahedra. There are two crystallographically distinct octahedral sites, which usually are occupied by M

and M' ions with different size and charge. In case of $LiFePO_4$, lithium ions occupy M1 sites and iron ions occupy M2 sites [46, 47].

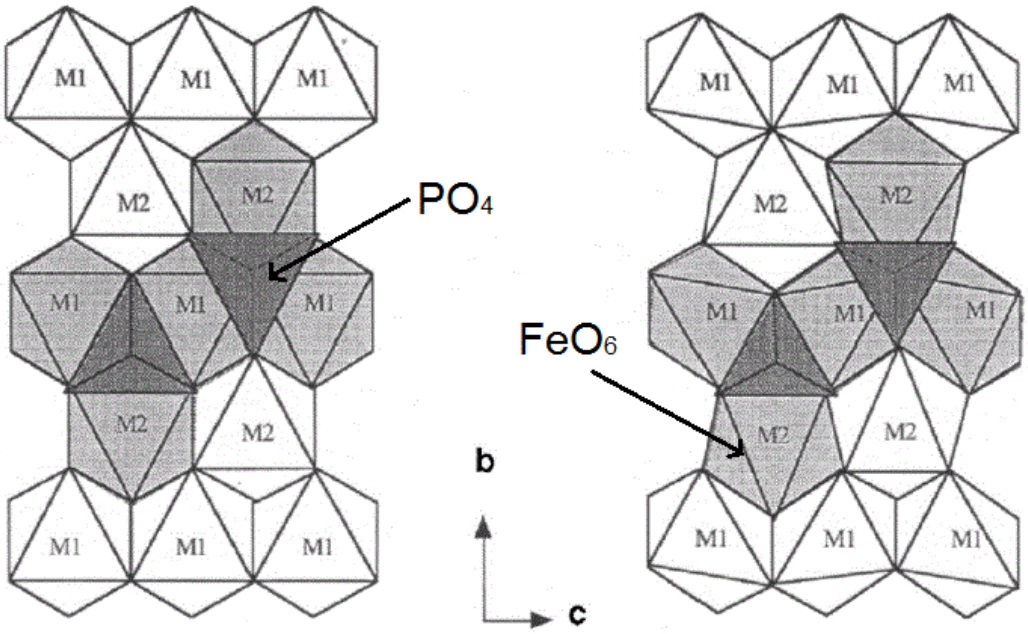

Figure 2.4.1 Olivine crystal structure: a) ideal hcp model and b) actual structure. Adapted from [47].

$LiFePO_4$ is pure ionic conductor. J. Li et al. have investigated Li ion conductivity in single crystal $LiFePO_4$. In the temperature range 300 K to 527 K, the highest conductivity values were obtained along b-axis. At 325 K conductivity value along b-axis was $7.93 \cdot 10^{-9}$ Scm^{-1} [48]. It is known, that lithium ions arrange in linear chains along b-axis of olivine structure. First principles calculations have also shown that Li ion conduction takes place through lithium chains along b-axis [49]. According to J. Li et al. activation energies for lithium diffusion along a, b, and c-axis were 0.636 eV, 0.54 eV and 0.669 eV respectively [48]. Wang and Hong have shown, that at temperature 25°C electronic and ionic contributions to total conductivity value in polycrystalline $LiFePO_4$ ceramics are $3.7 \cdot 10^{-9}$ and $5.0 \cdot 10^{-5}$ Scm^{-1} respectively [50].

In order to apply $LiFePO_4$ as cathode material in lithium ion batteries, its electronic conductivity has to be enhanced. Several modification of $LiFePO_4$ ways are known in the literature. One of the modification ways is doping. S.-Y. Chung et al. have obtained conductivity increase by substituting Li by Mg, Al, Ti, Nb or W. Conductivity values obtained for $Li_{1-x}M_xFePO_4$ (M = Mg, Al, Ti, Nb, W) were greater than 10^{-3} Scm^{-1} [51]. Wang and Hong have doped iron by Ni or Mg. Iron doping by nickel in $LiFePO_4$ has increased electronic conductivity value at 25°C to $6.40 \cdot 10^{-3}$ Scm^{-1} in $LiFe_{0.95}Ni_{0.05}PO_4$, while ionic conductivity value remained nearly as in pure $LiFePO_4$ and was equal to $5.04 \cdot 10^{-5}$ Scm^{-1} [50]. Iron doping by manganese has varied both electronic and ionic conductivity values in $LiFe_{0.95}Mg_{0.05}PO_4$ and they were equal to $1.65 \cdot 10^{-4}$ Scm^{-1} and $1.79 \cdot 10^{-4}$ Scm^{-1} respectively [50]. Electronic conductivity value variation in pure $LiFePO_4$ and doped iron phosphates ($LiFe_{0.95}Ni_{0.05}PO_4$ and $LiFe_{0.95}Mg_{0.05}PO_4$) was explained by different carbon content in the compounds because of carbon-containing precursors and different heat treatment [50].

3. EXPERIMENTAL

3.1. **X-ray diffraction**

Structural investigation of the materials was carried out with **X-ray diffraction (XRD) technique**. The structure parameters at room temperature were obtained from the X-ray powder diffraction using Brucker D8 Advance equipment in the region 2θ = 10-70 degree, step 0.01-0.02 degree, time per step 1-8 sec., CuKα_1 radiation. The lattice parameters were deduced by fitting the XRD patterns with software TOPAS v. 4.1 and SCANIX v. 2.16 (Matpol).

X-ray diffraction measurements at elevated temperatures were carried out under vacuum using Θ–Θ goniometer modification (X-ray tube and detector had 250 mm radius) of Bruker D8 instrument equipped with CuKα radiation source, Mri heating chamber and Lynx eye linear PSD detector. The channel width of the used PSD detector was approximately 0.015°, scanning step size was set to 0.01°, scanning speed was 2 s per step and divergence slit was set to 0.1°. In the heating chamber, sample powders were thinly spread directly on the heating element (PtRh foil). The temperature was measured and adjusted by the readings of the thermocouple which was welded at the backside of the heating element. After reaching each temperature the sample was left idle for 1800 s to reach thermal equilibrium with the heating element.

3.2. **X-ray Photoelectron Spectroscopy**

X-ray Photoelectron Spectroscopy (XPS) or Electron Spectroscopy for Chemical Analysis (ESCA) is a powerful surface analysis method. It collects information about surface layer of approximately 10 nm. Surface of the material is irradiated with Mg Kα (hν = 1253.6 eV) or Al Kα (hν = 1486.6 eV) radiation. This causes photoelectrons to be emitted from the samples surface. Kinetic energy of excited electron can be calculated according to formula

$$E_K = h\nu - E_B - \varphi, \qquad (3.2.1)$$

where $h\nu$ is energy of X-rays, E_B is binding energy and φ is work function.

In this work, XPS were recorded by LAS-3000 (ISA-Riber) surface analysis equipment. The instrument was equipped with double-pass cylindrical mirror analyzer MAC2. The XPS were obtained by using Al Kα ($h\nu$ = 1486.6 eV) or Mg Kα (hν = 1253.6 eV) radiation at an average of 30 scans with step size of 0.05 eV. Before the measurement, the ceramic samples with polished surfaces were kept in a preparation chamber (residual pressure $1.6 \cdot 10^{-6}$ Pa) of the experimental setup for one day. The residual pressure in the analyzer chamber was $1.3 \cdot 10^{-8}$ Pa. In order to extract the core-level shifts and relative intensities of these components, a curve-fitting procedure was utilized. The fitting of the core-level data was performed using a nonlinear fitting procedure with software XPSPEAK 41.

To exclude any effects on the values of binding energies due to charging of the sample during the XPS analysis, all data were corrected by a linear shift such that the peak maximum of the C 1s binding energy of adventitious carbon corresponded to 284.6 eV.

3.3. Scanning Electron Microscopy and Energy Dispersive X-ray analysis

Scanning electron microscopy (SEM) and energy-dispersive X-ray spectroscopy (EDX) techniques were used for the analysis of chemical composition of the investigated compounds. Both techniques are integrated in TM3000 – Hitachi equipment, which was used for the investigation. Ceramics were prepared for SEM/EDX investigation. Pellets were broken and measurements were performed on the broken edge.

3.4. **Impedance Spectroscopy**

Electrical properties of the ceramics were investigated by **broadband impedance spectroscopy.** When a monochromatic alternating voltage $U(t) = U_m\sin(\omega t)$ is applied to a system then the resulting current is $I(t) = I_m\sin(\omega t-\phi)$, where ϕ is the phase difference between voltage and current, U_m is amplitude of sinusoidal voltage and I_m is amplitude of sinusoidal current. Electrical impedance obeys Ohm's law and it can be defined as $\tilde{Z} = U(t)/I(t) = |Z| \exp(j\phi) = Z' - jZ''$, where $j = (-1)^{1/2}$. The specific impedance can be defined by formula: $\tilde{z} = \tilde{Z}\frac{S}{l}$, where S is electrode area and l is sample length. Electrical impedance can be plotted in complex plain as planar vector (see Figure 3.4.1)[52].

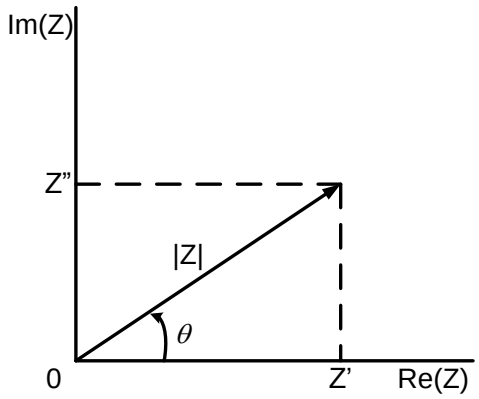

Figure 3.4.1 Electrical impedance Z plotted as planar vector. Adapted from [53]

When analyzing a system by broadband impedance spectroscopy, not only impedance, but all four immittances (specific impedance $\tilde{z}$, specific admittance $\tilde{\sigma}$, dielectric permittivity $\tilde{\varepsilon}$, and electric modulus $\tilde{m}$) can be used. The following equations show interrelationships between immittances:

$$\tilde{z} = z' - jz'', \tag{3.4.1}$$

$$\tilde{\sigma} = \sigma' + j\sigma'' = 1/\tilde{z}, \tag{3.4.2}$$

$$\tilde{\varepsilon} = \varepsilon' - j\varepsilon'' = \tilde{\sigma}/j\omega\varepsilon_0, \tag{3.4.3}$$

$$\tilde{m} = m' + jm'' = 1/\tilde{\varepsilon} = j\omega\varepsilon_0\tilde{z}, \tag{3.4.4}$$

where ε_0 is the dielectric permittivity of free space.

Broadband impedance spectroscopy can cover frequency regime from 10^{-6} Hz up to 10^{12} Hz [52]. Several polarization mechanisms can occur in the material in this frequency range. Electronic or atomic polarization arises from electron cloud shift from nucleus when electrical field is applied and it typically persists at frequencies between about 10^{13}-10^{15} Hz [52]. Usually in solids with ionic bonding positive and negative ions form natural dipoles, but the net polarization of a volume is equal to zero. In electrical field ions move slightly and create nonzero net dipole moment. This type of polarization is called ionic polarization. Ionic polarization typically persists at frequencies between 10^{9}-10^{13} Hz [52]. Orientation polarization can occur in the materials with built in dipoles. The dipoles in this kind of material orient themselves in the direction of external electrical field. This type of polarization typically happens below 10^{9} Hz [52]. Another important type of polarization is interface or space charge polarization. This polarization mechanism is also known as Maxwell-Wagner-Silars polarization. In this case polarization occurs at grain boundaries, electrode-material interface or any other interface. This type of polarization occurs at low frequencies. Electrode polarization is due to charge carriers blocking at the material-electrode interface. Electrical double layer charges and discharges with alternating electrical field. Electrode polarization affects impedance spectra of the material at low frequencies. The higher the conductivity of the sample the higher frequencies are influenced by this type of polarization [52].

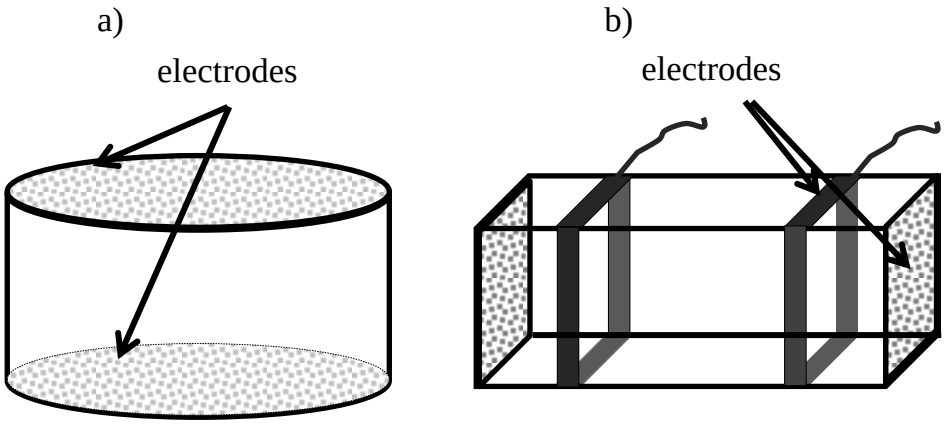

Figure 3.4.2 Sample geometry for (a) two- and (b) four- probe impedance spectroscopy measurements.

It is impossible to cover all broadband frequency range only with one technique. In this work two different spectrometers were used. High frequency range (0.3 – 3000 MHz) was covered with a spectrometer based on Agilent E5062A network analyzer. This impedance spectrometer is capable to work in the temperature range 300 to 1200 K. A cylindrically shaped sample with electrodes on both faces (as shown in Figure 3.4.2 (a)) is necessary for the measurements. A coaxial waveguide made of $3Al_2O_3$-$2SiO_2$ (mullite) ceramic covered with platinum serves as a sample holder. The separation of inner conductor into two parts enables to place a sample in the gap. Control of network analyzer Agilent E5062A, DC power supply and digital thermometer by the computer is realized with software developed on Matlab environment. Network analyzer Agilent E5062A is used to measure scattering S-parameters.

a)

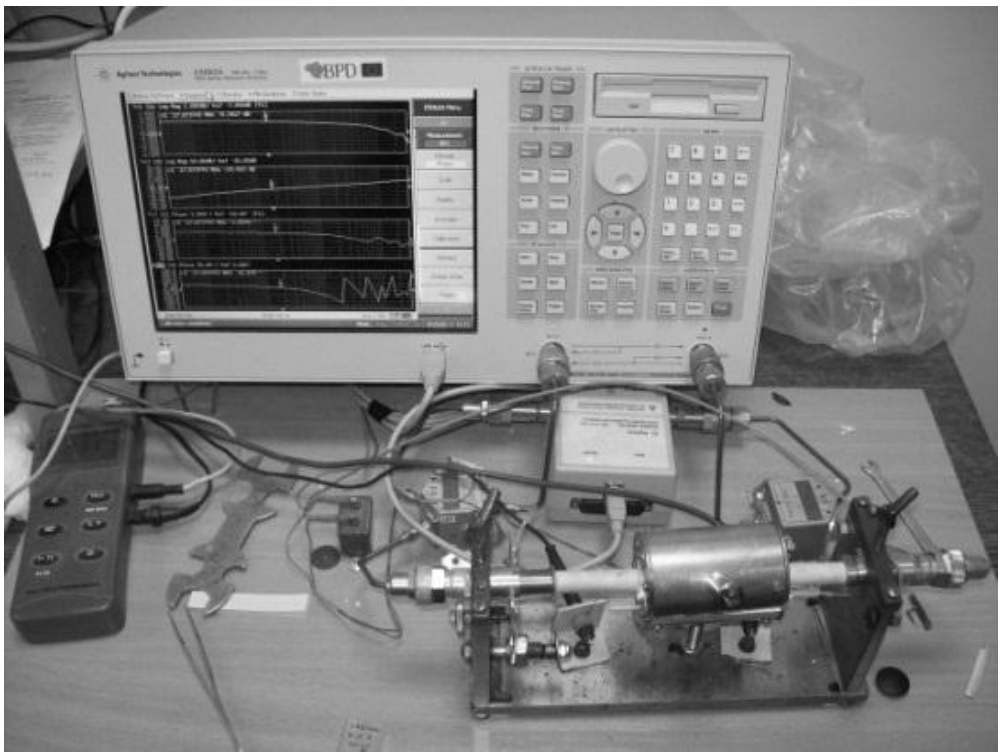

b)

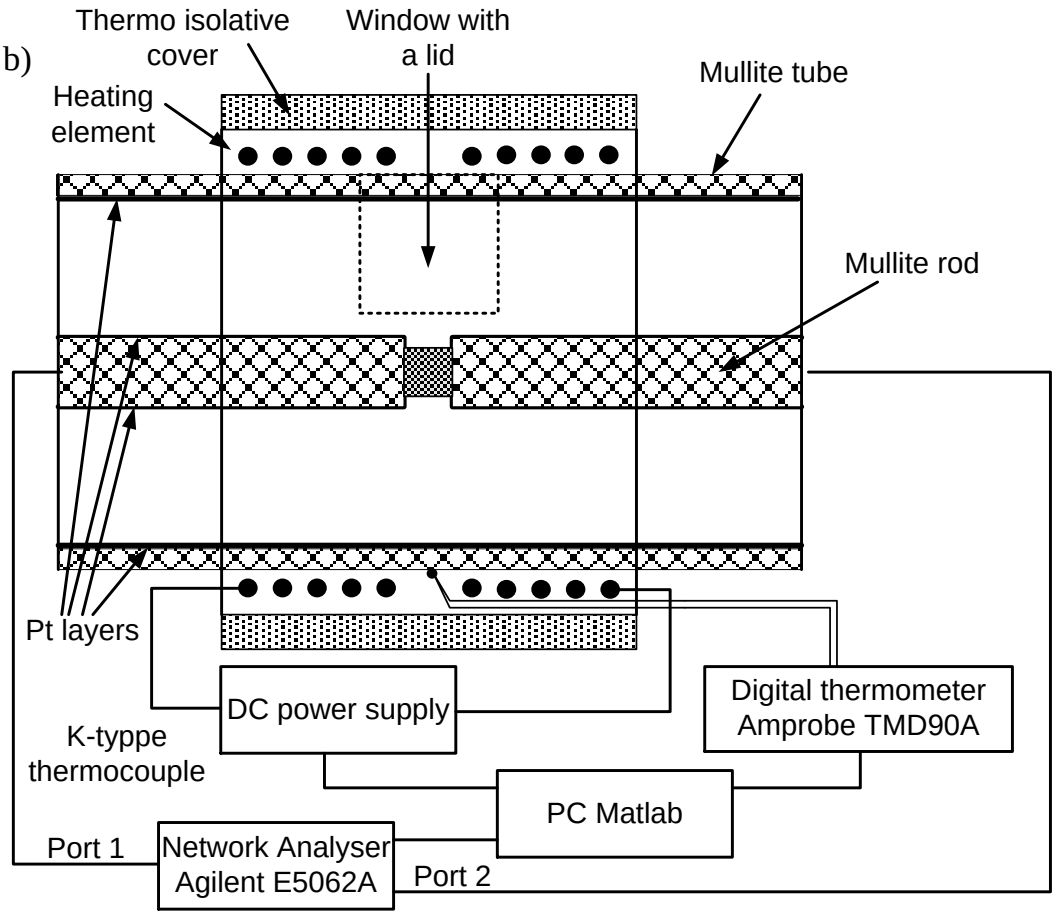

Figure 3.4.3 Photo (a) and the block-scheme (b) of the high frequency impedance spectrometer [54].

Impedance measurements in low frequency range (10 – $2 \cdot 10^6$ Hz) were performed with low frequency setup, which is capable to work in two- or four-electrode measurement mode. A sample with special geometry (see Figure 3.4.2 (b)) is necessary for 4-electrode method measurements. Operation of the spectrometer is based on voltmeter-ammeter method. This method is based on measurements of voltage applied to the sample, current in the sample and phase difference between voltage and current. Schematic overview of the spectrometer and its photograph are shown in Figure 3.4.4. Operation of the spectrometer is controlled by computer with software developed in Matlab environment. Instrument TiePie Handyscope HS3-50 is used for signal generation and voltage determination. The current in the sample is measured by current to voltage converter, which feeds the signal to the first channel (CH1) of the oscilloscope. The voltage applied to the sample is fed to second channel (CH2) of the oscilloscope. Differential amplifier is used for four-electrode method realization. Low frequency setup is capable to work in temperature range 300 to 800 K. The heater is powered with computer controlled power supply and digital thermometer Amprobe TMD90A is used for temperature control.

a)

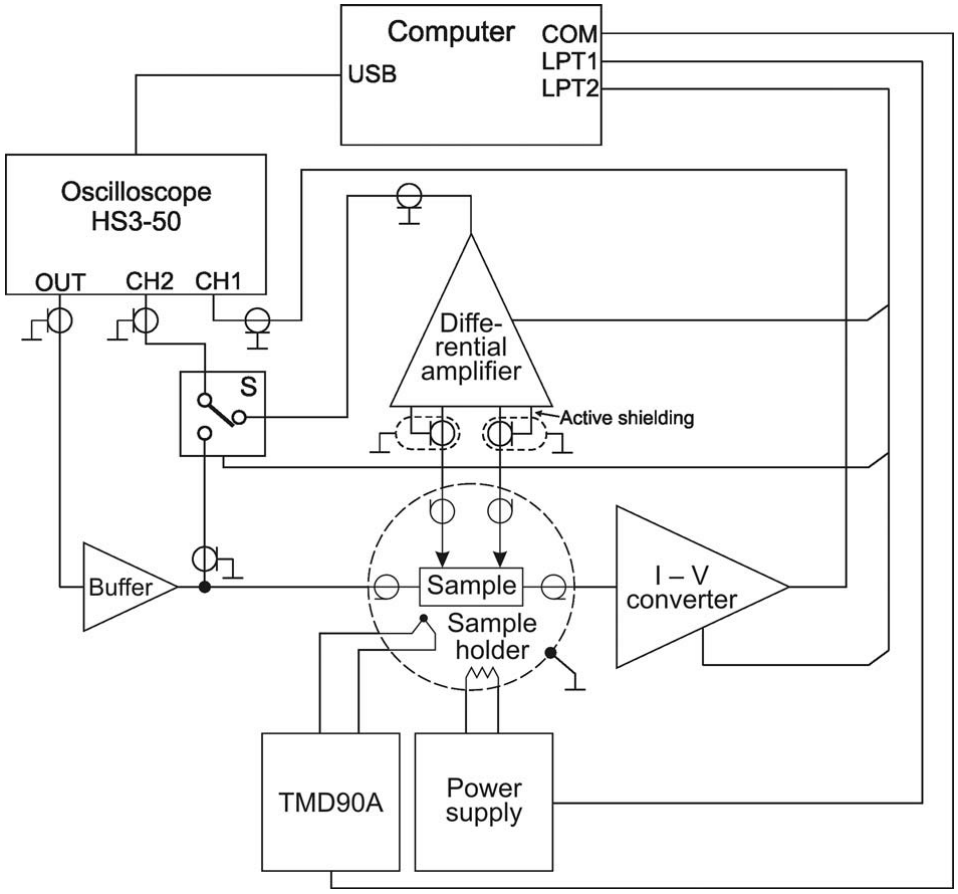

b)

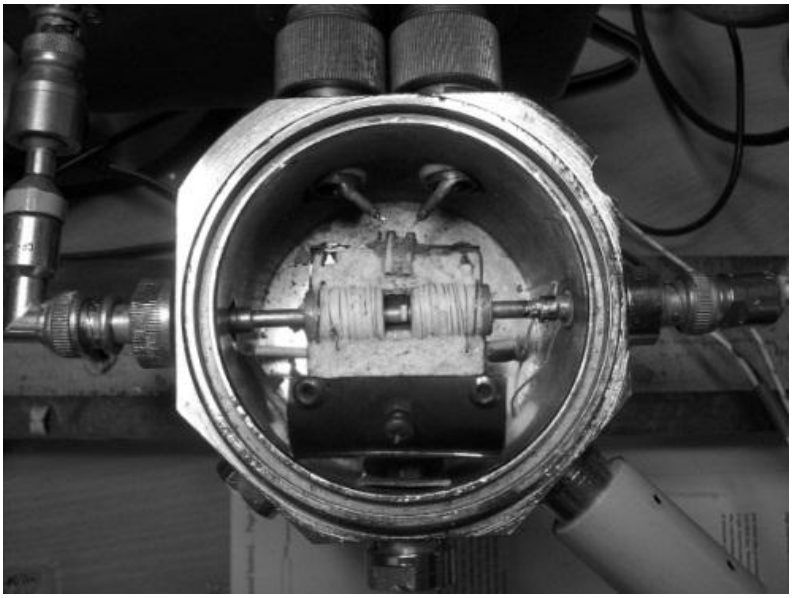

Figure 3.4.4 Schematic overview of low frequency set up a) and photograph of this spectrometers sample holder b) [55].

4. RESULTS AND DISCUSSION

4.1. Synthesis of Li^+ solid electrolytes

The powders of investigated compounds were synthesized by solid state reaction. Solid phase starting materials are used for this method of synthesis. Starting materials are mixed together and milled. In this work milling was performed in ethanol. Several milling and heating steps ensure that all starting materials will come into contact with each other for reaction. The sequences of synthesis of investigated compounds are shown below (see Fig. 4.1.1 – 4.1.6).

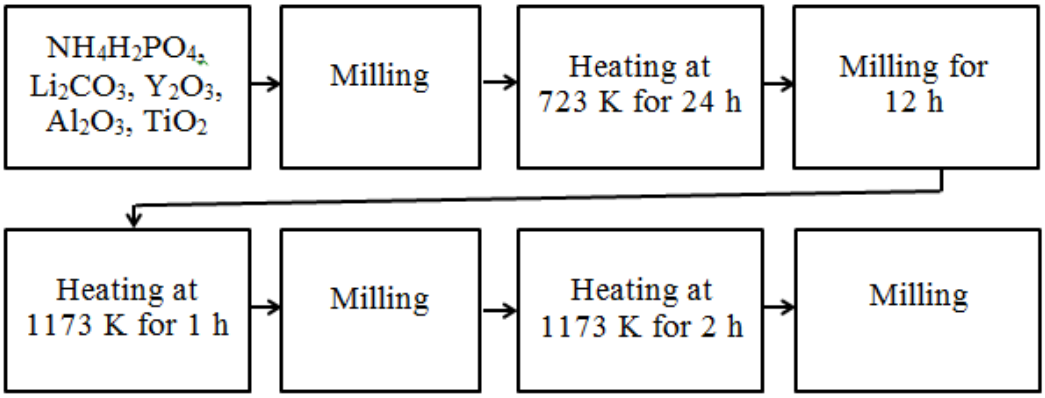

Figure 4.1.1 Synthesis of $Li_{1.3}Al_yY_{x-y}Ti_{1.7}(PO_4)_3$ by solid state reaction.

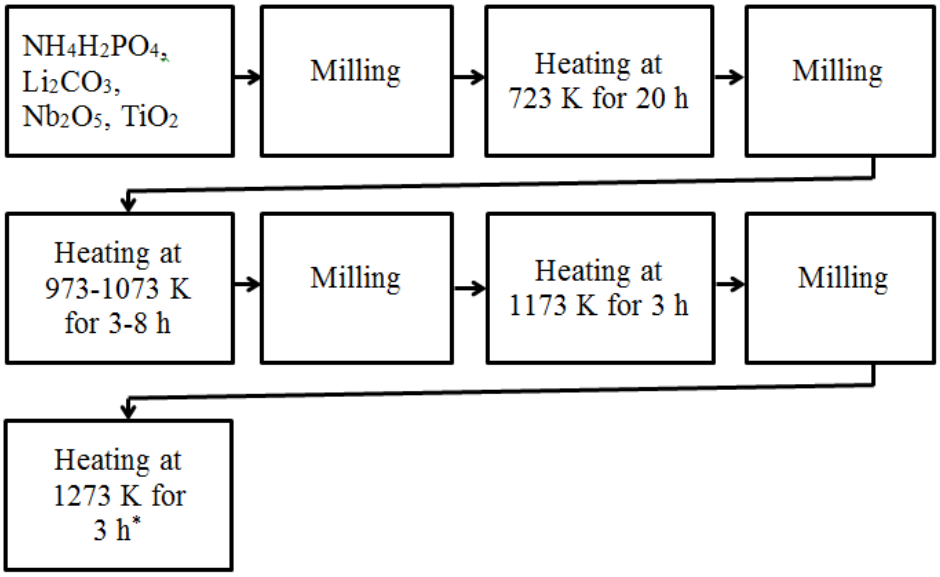

Figure 4.1.2 Synthesis of $Li_{1+4x}Ti_{2-x}Nb_yP_{3-y}O_{12}$ by solid state reaction (* - The heating step for the compound with y = 0.1 was 1473 K for 2 h.

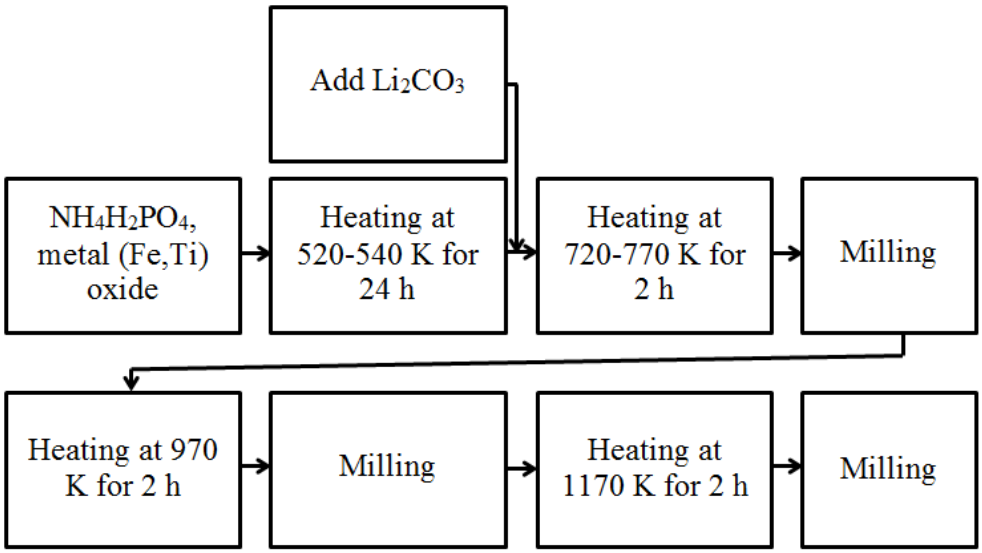

Figure 4.1.3 Synthesis of $LiFeP_2O_7$ and $Li_{0.9}Fe_{0.9}Ti_{0.1}P_2O_7$ by solid state reaction

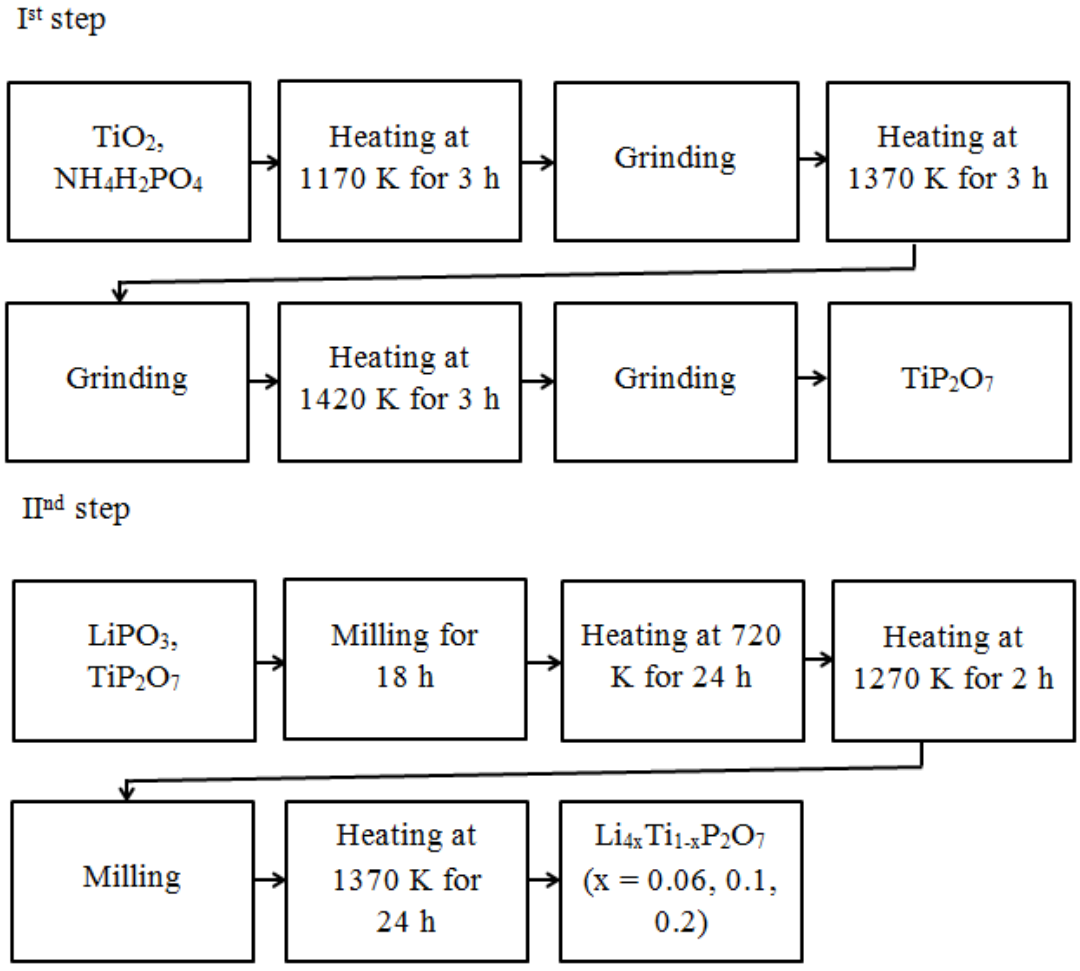

Figure 4.1.4 Synthesis of $Li_{4x}Ti_{1-x}P_2O_7$ (x = 0, 0.06, 0.1, 0.2) by solid state reaction.

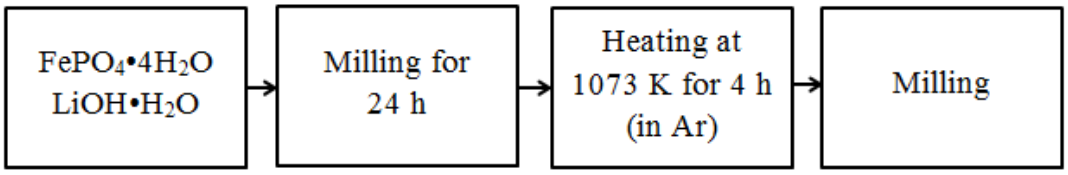

Figure 4.1.5 Synthesis of $LiFePO_4$ by solid state reaction.

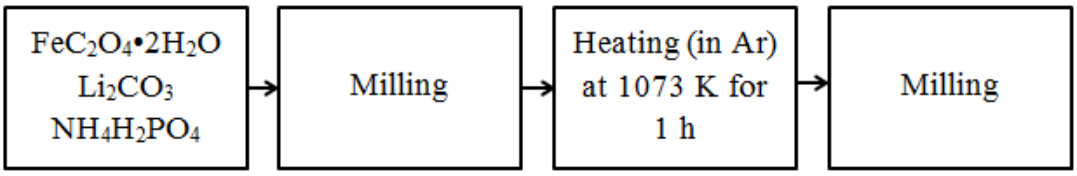

Figure 4.1.6 Synthesis of $LiFePO_4$/C by solid state reaction.

4.2. **Solid electrolyte ceramics fabrication technology**

In order to prepare ceramics, powders of solid electrolytes were uniaxially cold-pressed into pellets at pressures between 150-300 MPa. Most pellets were sintered in air. Sintering temperatures (T_s) and sintering times (t_s) are presented in Table 4.2.1. The heating and cooling ratio in the furnace was 5 K/min. Before sintering pellets are heated at 673 K for 1 h (see Figure 4.2.1). Densities of the pellets (d) were evaluated by measuring geometry and mass of the pellets. Relative densities of the ceramics were calculated according to formula $d_r = (d / d_{XRD}) \cdot 100\%$, where d_{XRD} is the theoretical density calculated from XRD patterns of the compounds. Relative densities of the investigated ceramics are presented in Table 4.2.1 too.

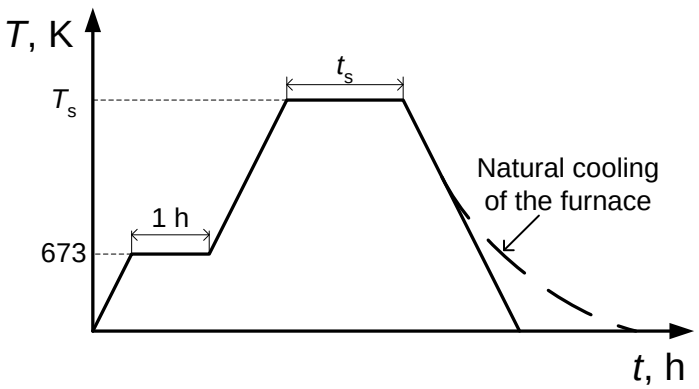

Figure 4.2.1 Schematic diagram of the sintering process of ceramics.

Table 4.2.1 Ceramics preparation conditions and relative densities of the ceramics

Compound	Pressure P, MPa	Sintering temperature T_s, K	Sintering time t_s, h	Relative density d_r, %
$Li_{1.8}Ti_{1.8}(PO_4)_3$	300	1363	1	95
$Li_3Ti_{1.5}(PO_4)_3$	300	923	1	81
$Li_{1.4}Ti_{1.9}P_3O_{12}$	300	1343	1	
$Li_{1.4}Ti_{1.9}Nb_{0.1}P_{2.9}O_{12}$	300	1223	1	
$Li_{1.8}Ti_{1.8}Nb_{0.2}P_{2.8}O_{12}$	300	1223	1	
$Li_{2.2}Ti_{1.7}Nb_{0.3}P_{2.7}O_{12}$	300	1223	1	
$Li_{1.3}Al_{0.2}Y_{0.1}Ti_{1.7}(PO_4)_3$	300	1373	1	
$Li_{1.3}Al_{0.1}Y_{0.2}Ti_{1.7}(PO_4)_3$	300	1373	1	
$LiFePO_4$	300	1073	10	85.8
$LiFePO_4$/C	300	1073 (in Ar)	1	73.7
$Li_4Ti_5O_{12}$	150	1173	10	79
$Li_4Ti_{4.95}Ta_{0.05}O_{12}$	150	1173	10	86
$Li_4Ti_{4.95}Nb_{0.05}O_{12}$	150	1173	10	83
$LiFeP_2O_7$	300	1173	2	73
$Li_{0.9}Fe_{0.9}Ti_{0.1}P_2O_7$	300	1173	2	71
TiP_2O_7	150	1460	3	92
$Li_{0.24}Ti_{0.94}P_2O_7$	150	1370	1	
$Li_{0.4}Ti_{0.9}P_2O_7$	150	1270	1	
$Li_{0.8}Ti_{0.8}P_2O_7$	150	1170	1	

4.3. **Structure of lithium solid electrolytes**

Structure of the investigated lithium solid electrolytes was investigated by X-Ray diffraction analysis. Refined lattice parameters and theoretical densities at room temperature are presented in Table 4.3.1.

Table 4.3.1 Lattice parameters and theoretical densities of the powders.

Compound	Space group	a, Å	b, Å	c, Å	V, Å^3	d_{XRD}, g/cm^3	Z
$Li_{1.8}Ti_{1.8}(PO_4)_3$	$R\bar{3}c$	8.5162(4)		20.8482(30)	1309.5	2.9	6
$Li_3Ti_{1.5}(PO_4)_3$	$R\bar{3}c$	8.5144(5)		20.8762(60)	1310.8	2.85	6
$Li_{1.4}Ti_{1.9}P_3O_{12}$	$R\bar{3}c$	8.5137(2)		20.8587(5)	1309.36	2.93	6
$Li_{1.4}Ti_{1.9}Nb_{0.1}P_{2.9}O_{12}$	$R\bar{3}c$	8.5267(23)		20.8608(53)	1313.49	2.97	6
$Li_{1.8}Ti_{1.8}Nb_{0.2}P_{2.8}O_{12}$	$R\bar{3}c$	8.5257(6)		20.8975(35)	1315.49	3	6
$Li_{2.2}Ti_{1.7}Nb_{0.3}P_{2.7}O_{12}$	$R\bar{3}c$	8.5242(7)		20.8976(27)	1315.04	3.03	6
$Li_{1.3}Al_{0.2}Y_{0.1}Ti_{1.7}(PO_4)_3$	$R\bar{3}c$	8.5054(4)		20.8247(12)	1304.68	2.974	6
$Li_{1.3}Al_{0.1}Y_{0.2}Ti_{1.7}(PO_4)_3$	$R\bar{3}c$	8.5109(4)		20.8372(16)	1307.1	3.016	6
$LiFePO_4$	Pnma					3.6	
$LiFePO_4$/C	Pnma					3.42	

Table 4.3.1 continued.

Compound	Space group	a, Å	b, Å	c, Å	V, Å^3	d_{XRD}, g/cm^3	Z
$Li_4Ti_5O_{12}$	$Fd\bar{3}m$	8.3586			584.004	3.48	
$Li_4Ti_{4.95}Ta_{0.05}O_{12}$	$Fd\bar{3}m$	8.3627			584.85	3.48	
$Li_4Ti_{4.95}Nb_{0.05}O_{12}$	$Fd\bar{3}m$	8.3633			584.98	3.48	
$LiFeP_2O_7$	$P2_1$	4.8240(2)	8.0828(3)	6.9390(2)	255.19	3.081	
$Li_{0.9}Fe_{0.9}Ti_{0.1}P_2O_7$	$P2_1$	4.8239(4)	8.0786(6)	6.9365(5)	255.09	3.063	
TiP_2O_7	$Pa\bar{3}$	23.6249(2)				3.015	108
$Li_{0.24}Ti_{0.94}P_2O_7$	$Pa\bar{3}$	23.6229(2)				3	108
$Li_{0.4}Ti_{0.9}P_2O_7$	$Pa\bar{3}$	23.6235(2)				2.99	108
$Li_{0.8}Ti_{0.8}P_2O_7$	$Pa\bar{3}$	23.6262(2)				2.96	108

NASICON-type structure compounds [A1, A2, A3]. Figure 4.3.1 shows powder X-ray diffraction patterns of $Li_{1.3}Al_yY_{x-y}Ti_{1.7}(PO_4)_3$ (x = 0.3; y = 0.1, 0.2) prepared by solid state reaction. Small amounts (up to 1.5 %) of $LiTiPO_5$ and YPO_4 were detected as impurities and marked with asterisks in Figure 4.3.1. At the room temperature, the $Li_{1.3}Al_yY_{x-y}Ti_{1.7}(PO_4)_3$ (x = 0.3; y = 0.1, 0.2) compounds belong to the rhombohedral symmetry (space group $R\bar{3}c$) with six formula units in the unit cell. The lattice parameters, unit cell volume (V) and theoretical density (d_t) of the investigated compounds are presented in Table 4.3.1.

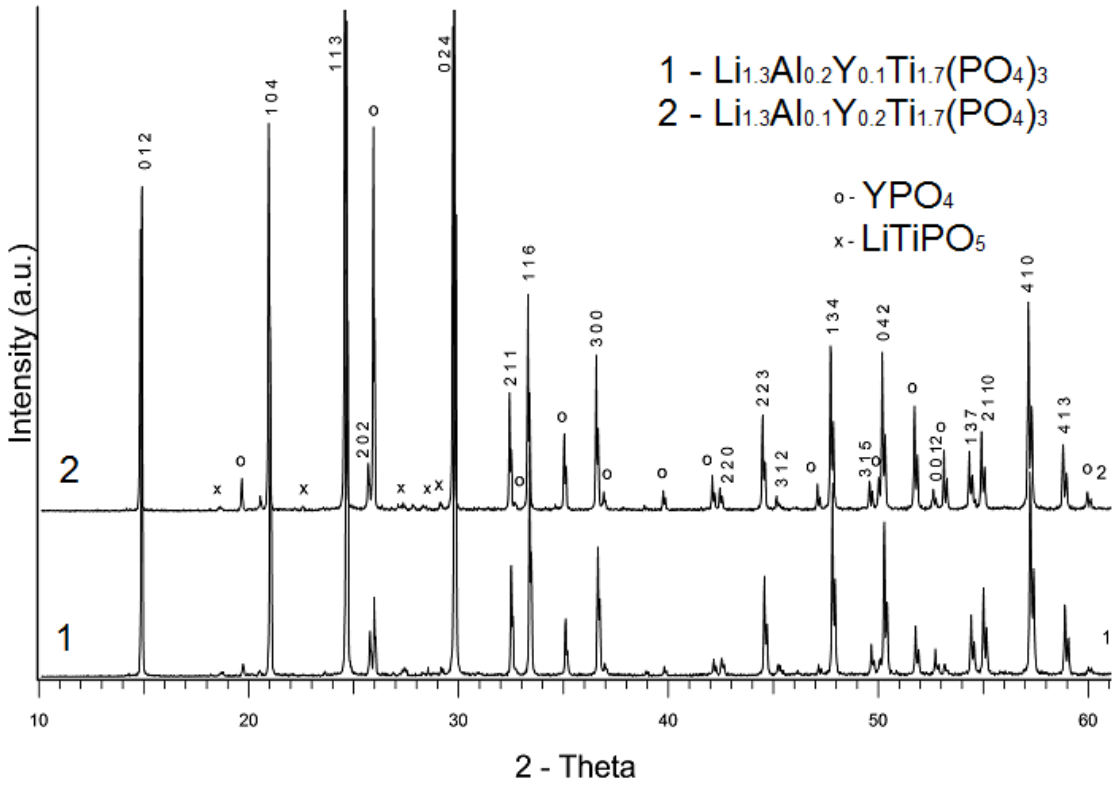

Figure 4.3.1 Powder X-ray diffraction patterns of $Li_{1.3}Al_yY_{x-y}Ti_{1.7}(PO_4)_3$ (x = 0.3; y = 0.1, 0.2) recorded at room temperature.

A partial substitution of Al^{3+} by Y^{3+} in $Li_{1.3}Al_yY_{x-y}Ti_{1.7}(PO_4)_3$ (x = 0.3; y = 0.1, 0.2) causes the increase in the lattice parameters and theoretical density of the compound (see Figure 4.3.2). This variation can be caused by different ionic radii of Y^{3+} and Al^{3+} ions. The ionic radii of Y^{3+} and Al^{3+} are 1.04 Å and 0.675 Å, respectively [56]. On the other hand, the analysis of XRD patterns

shows impurities of YPO_4 and $LiTiPO_5$, which can influence the above mentioned parameters.

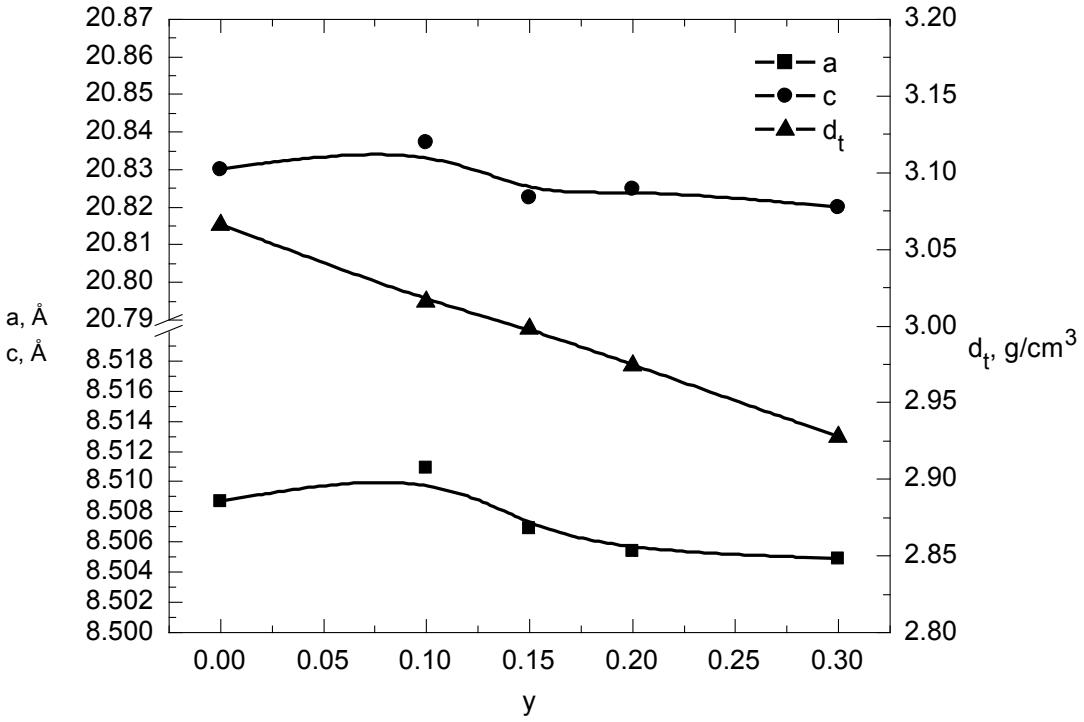

Figure 4.3.2 Lattice parameters (a, c) and theoretical density (d_t) of $Li_{1.3}Al_yY_{0.3-y}Ti_{1.7}(PO_4)_3$ dependences on parameter y. (The data for y = 0, 0.3 and y = 0.15 are from the references [57] and [58] respectively).

Figure 4.3.3 shows powder X-ray diffraction patterns of $Li_{1+4x}Ti_{2-x}Nb_yP_{3-y}O_{12}$ (x = 0.1, 0.2, 0.3; y = 0, 0.1, 0.2, 0.3) compounds. The results of XRD data analysis have shown that $LiTiPO_5$ impurities are present in compounds with y = 0, 0.1, 0.2, 0.3 and they are marked with asterisks in Figure 4.3.3. In compounds with y = 0, 0.1, 0.2 and 0.3 the amounts of impurities were found to be 2%, 3%, 8% and 17% respectively. The investigated compounds belong to hexagonal symmetry (space group $R\bar{3}c$). The lattice parameters, unit cell volume (V), theoretical density ($d_{X\text{-}ray}$) and formula units in the lattice (Z) of the investigated compounds are presented in Table 4.3.1. The relative density of the ceramics was found to be 94 % of the theoretical density.

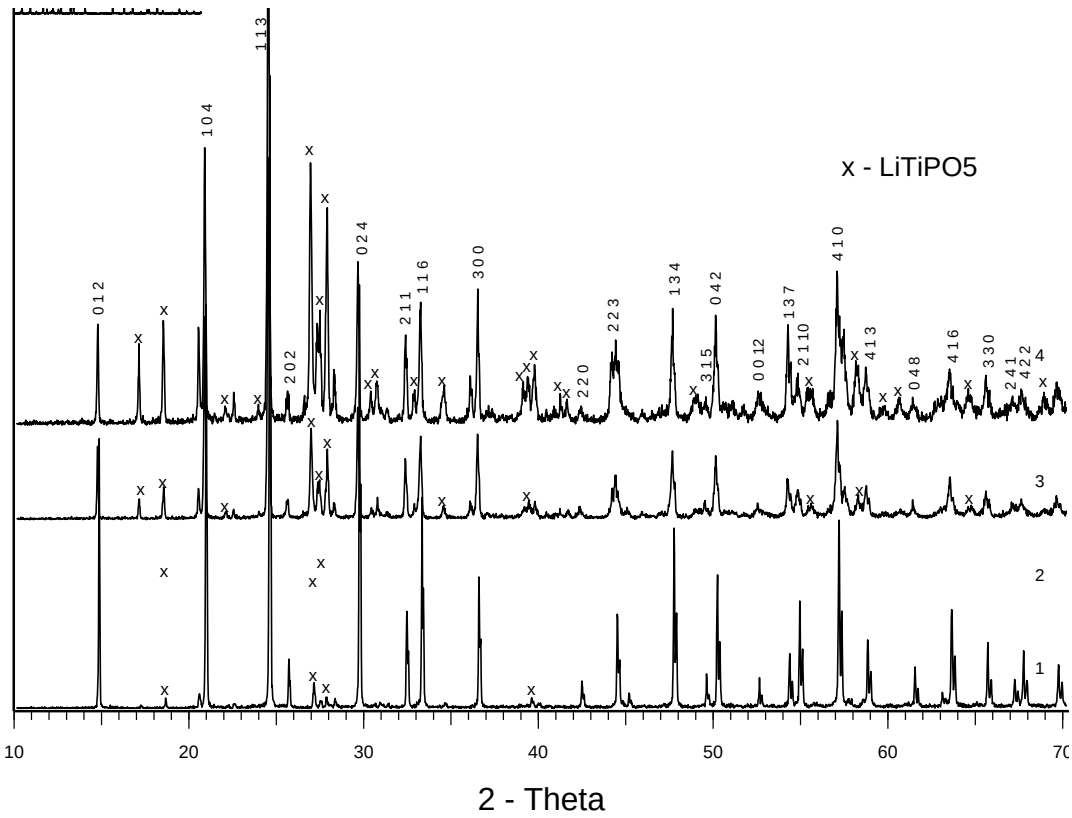

Figure 4.3.3 The powder X-ray diffraction patterns of $Li_{1+4x}Ti_{2-x}Nb_yP_{3-y}O_{12}$ compounds (1-(x = 0.1, y = 0); 2- (x = 0.1, y = 0.1); 3- (x = 0.2, y = 0.2); 4- (x = 0.3, y = 0.3)).

The amounts of up to 0.8 wt. % and 5 wt. % of $LiTiPO_5$ and $Li_4(P_2O_7)$ in compounds $Li_{1+4x}Ti_{2-x}(PO_4)_3$ with x = 0.2 and 0.5, respectively, were found. The amounts of impurities were estimated from the intensities and their square analysis of XRD patterns. $LiTiPO_5$ and $Li_4(P_2O_7)$ belong to orthorhombic and triclinic symmetry group and are marked with asterisks on the XRD patterns in Figure 4.3.4. At room temperature the $Li_{1+4x}Ti_{2-x}(PO_4)_3$ (where x = 0.2, 0.5) compounds belong to the rhombohedral symmetry (space group $R\bar{3}c$) with six formula units in the unit cell. The lattice *a*, *c* parameters, volume (*V*), theoretical density (d_t) of the ceramics are presented in Table 4.3.1.

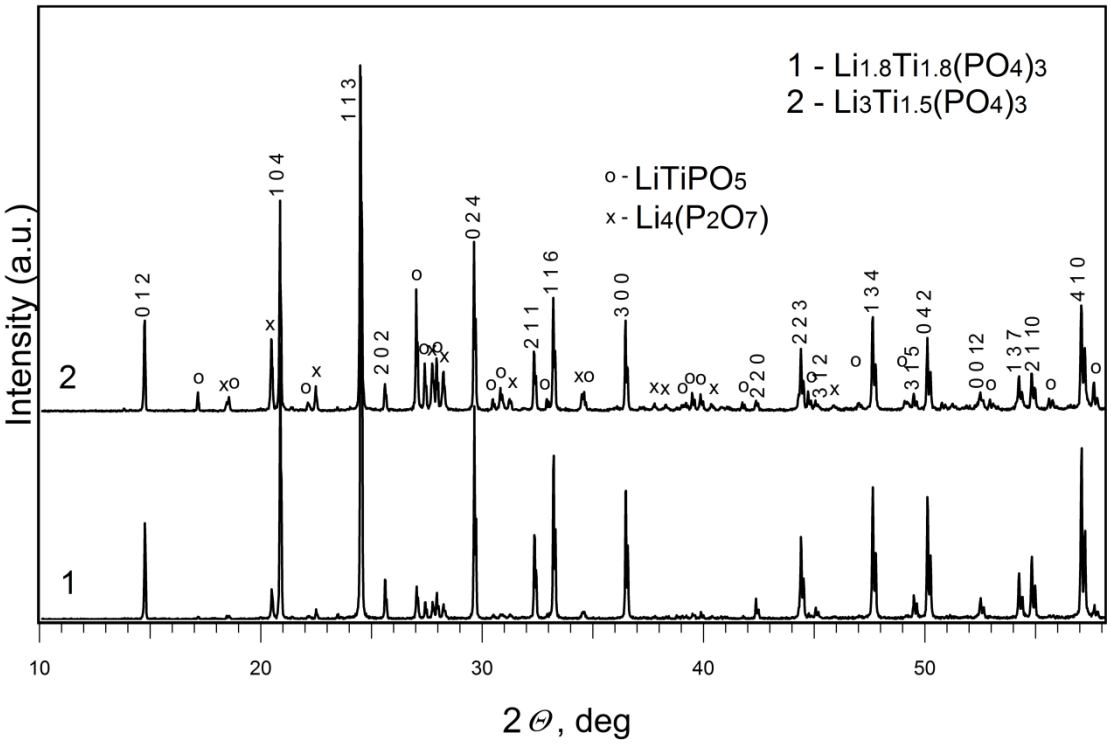

Figure 4.3.4 XRD patterns of $Li_{1+4x}Ti_{2-x}(PO_4)_3$ (where x = 0.2, 0.5) at room temperature.

The increase of Li content leads the increase of volume of the lattice and decrease of the theoretical density of the compounds. This variation can be caused by the different values of the ionic radii of Li^+ and Ti^{4+} ions. The ionic radii of Li^+ and Ti^{4+} are 0.92 Å and 0.74 Å respectively [56]. On the other hand, the analysis of XRD patterns shows the impurities of $LiTiPO_5$ and $Li_4(P_2O_7)$, which can influence the above mentioned parameters too.

XRD spectra of $LiFeP_2O_7$ and $Li_{0.9}Fe_{0.9}Ti_{0.1}P_2O_7$ pyrophosphates at various temperatures [A5]. X-ray powder diffraction analysis was performed at temperatures T = 300, 440, 540 and 680 K. The X-ray diffraction patterns of $LiFeP_2O_7$ and $Li_{0.9}Fe_{0.9}Ti_{0.1}P_2O_7$ powders at 300 K and 680 K are presented in Figure 4.3.5. Crystal structure of $LiFeP_2O_7$ powders has been indexed as monoclinic system (s.g. $P2_1$) in all the investigated temperatures. The structure was further refined based on the initial atomic positions reported in [59].

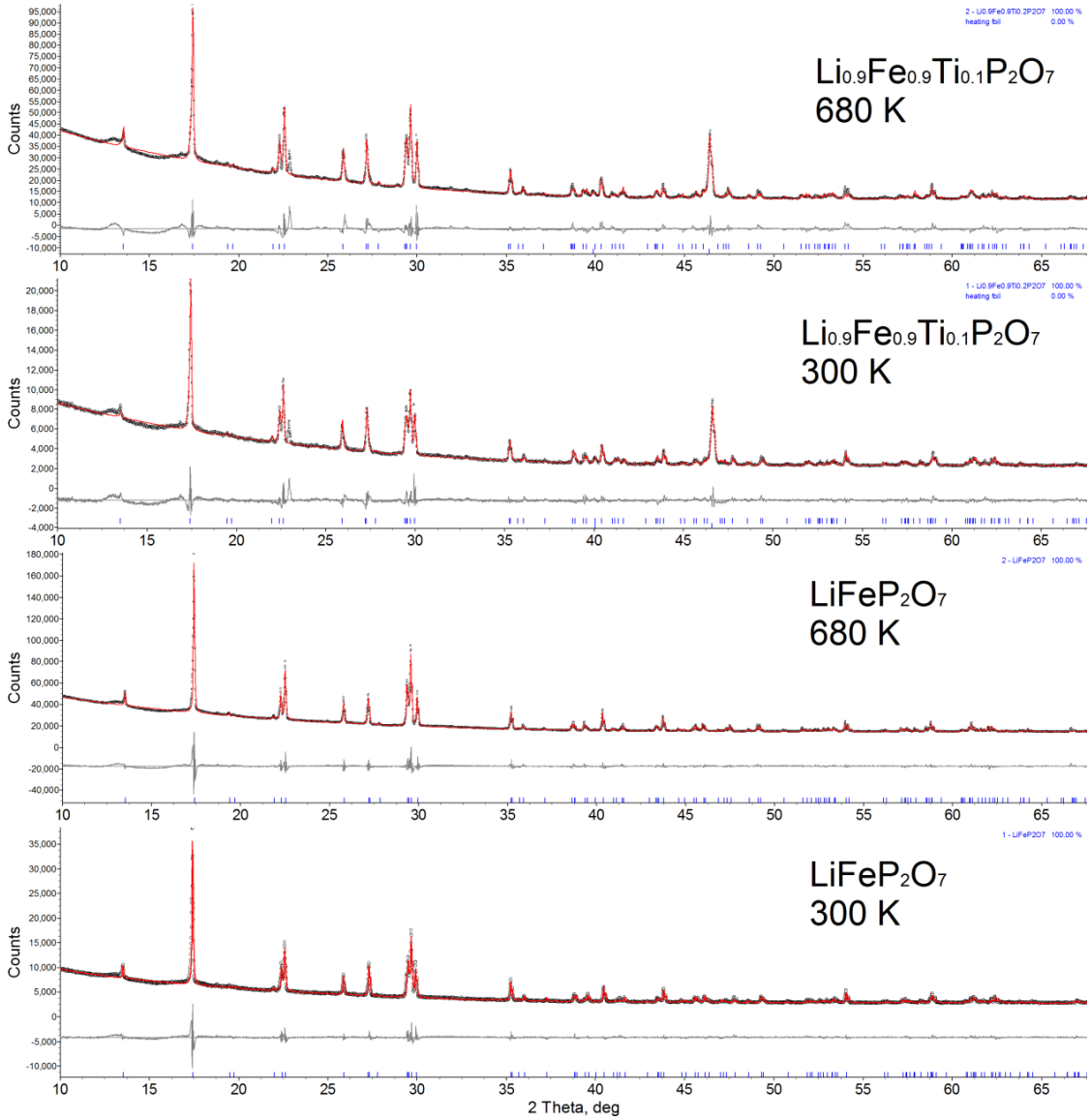

Figure 4.3.5 X-ray diffraction patterns for $Li_{0.9}Fe_{0.9}Ti_{0.1}P_2O_7$ and $LiFeP_2O_7$ compounds at 300 K and 680 K temperature.

The structure of $Li_{0.9}Fe_{0.9}Ti_{0.1}P_2O_7$ powders was also indexed as monoclinic system with $P2_1$ space group. Based on the observation of the same space group and other examples of partial Fe substitution in $LiFeP_2O_7$ it is expected that Ti partially replaces Fe atoms at its original sites but calculated and difference curves (Figure 4.3.5) indicates several additional peaks and intensity discrepancies. The peaks at roughly 40.0 and 46.6 degrees are known to be caused by heating element (Pt-Rh foil) and were included in the structure refinement as a Pawley phase (cubic, s. g. Fm-3m, a ≈ 4.8242). The exact cause of the strong peak at roughly 23.00 degrees and some minor peaks (for

example at 16.89, 24.49 and 26.09) is not clear, therefore it is not presented in the refinement (Figure 4.3.5.). However, it is probable that later peaks belong to the monoclinic $Fe(PO_3)_3$ phase (it could consist up to 6 wt. %) which was reported in [60]. The attempts to refine $Li_{0.9}Fe_{0.9}Ti_{0.1}P_2O_7$ XRD data using another Ti sites or by using other space group were not successful, therefore despite the observed inadequacies we assume that the structure is generally correct.

The additional modest improvement of XRD data refinement was observed then occupation coefficients (occ) were varied freely: for all atomic positions of $LiFeP_2O_7$ refined occ was close to 0.9, meanwhile for $Li_{0.9}Fe_{0.9}Ti_{0.1}P_2O_7$ refined occ values had tendency to be smaller by a value of 0.2-0.3 and for some sites were even lower than 0.5. Variation of occ are accompanied by inadequate changes of isotropic temperature factors (beq), therefore in the presented XRD data refinement variation of beq was limited (the chosen variation range limits were from 0 to 1). Under such restrictions beq relaxed to values close to 0 and 1: for $LiFeP_2O_7$ at 300 K beq relaxed to value of 0 only for Lithium and two oxygen atomic sites (four oxygen sites at 680 K); for $Li_{0.9}Fe_{0.9}Ti_{0.1}P_2O_7$ at 300 K beq relaxed to value of 0 for iron, lithium and two oxygen sites; for $Li_{0.9}Fe_{0.9}Ti_{0.1}P_2O_7$ at 680 K beq relaxed to value of 0 for lithium and six oxygen sites. Both of these effects (occ and beq variations) could be caused by the insufficient data quality which is reduced due to possible changes of heating foil curvature, X-ray beam cropping and scattering by heating chamber windows, relatively small acquisition times. On the other hand the anomalies of lattice parameters and tendency of occ changes of the atoms in the both compounds can be related to disordering in the unit cells of the compounds. This assumption is also supported by the observed differences in P/Fe atomic concentration ratios and variations of Fe^{2+} and Fe^{3+} states which are discussed below.

The refined lattice (a,b,c) parameters, volume of the unit cell (V), theoretical (d_{XRD}) density of the ceramics at room temperature are summarized in Table 4.3.1. The temperature dependences of the lattice parameters, V, β of the investigated compounds are shown in Figure 4.3.6. The volumes of the cells increase, β and densities decrease with increase of the temperature. The anomalies of lattice parameters of $LiFeP_2O_7$ and $Li_{0.9}Fe_{0.9}Ti_{0.1}P_2O_7$ in the temperature range 543 to 680 K were found. The anomalies of lattice parameters in the both compounds can be related to disordering in the unit cells of the compounds. It is worth to note, that the space group of both compounds at 300 K and 683 K temperature remains the same.

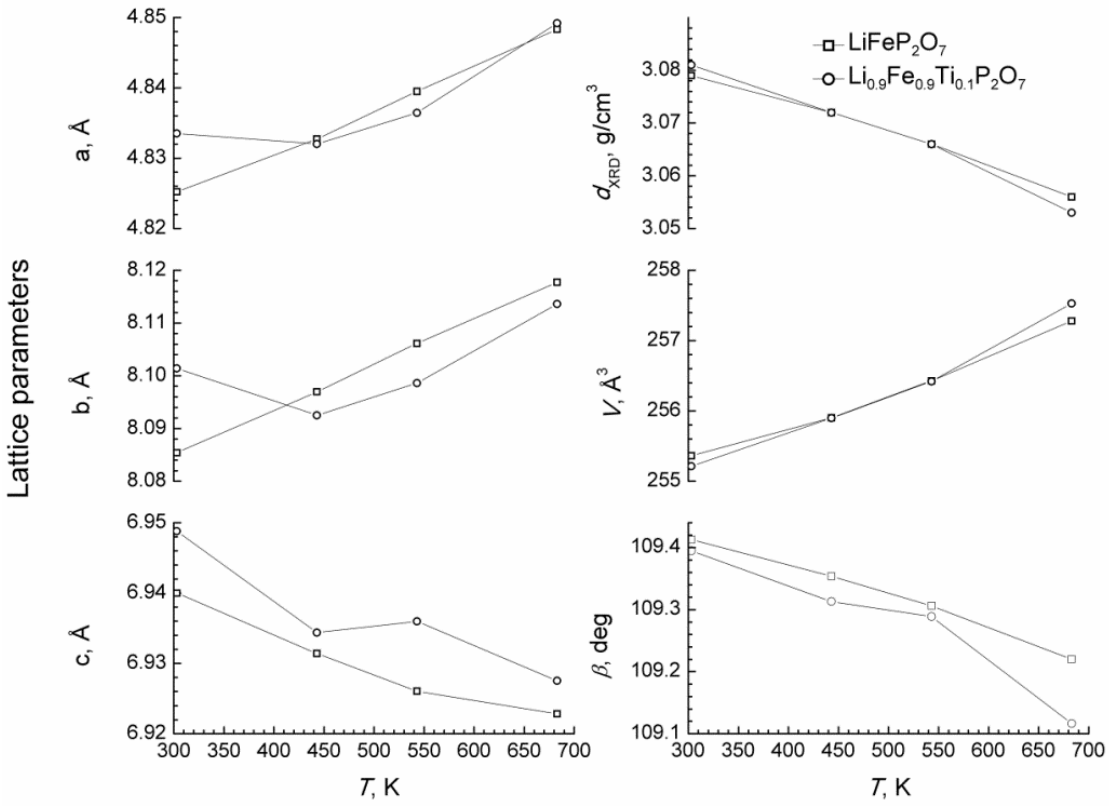

Figure 4.3.6 Lattice parameters (a, b, c), angle (β), volume (V), theoretical density (d_{XRD}) of $Li_{0.9}Fe_{0.9}Ti_{0.1}P_2O_7$ and $LiFeP_2O_7$ compounds determined from XRD analysis at different temperatures.

Crystal structure of $Li_{4x}Ti_{1-x}P_2O_7$ (x = 0, 0.06, 0.1, 0.2) pyrophosphates [A6]. XRD analysis at room temperature confirmed that obtained TiP_2O_7 powder belongs to cubic symmetry with space group $Pa\bar{3}$ as reported before [31]. Results of X-ray diffraction analysis also show that $Li_{4x}Ti_{1-x}P_2O_7$ (x = 0.06, 0.1, 0.2) compounds have cubic superstructure and the same space group as TiP_2O_7. The obtained XRD patterns are shown in Figure 4.3.7. Comparison of the results with the results reported in [61] shows some similarities between the $Li_{4x}Ti_{1-x}P_2O_7$ compounds synthesized in the present work and the $Li_xTiP_2O_7$ system during lithium insertion and extraction processes. The increase of lithium amount in the system $Li_{4x}Ti_{1-x}P_2O_7$ slightly decreased the theoretical density of the compounds (see Table 4.3.1).

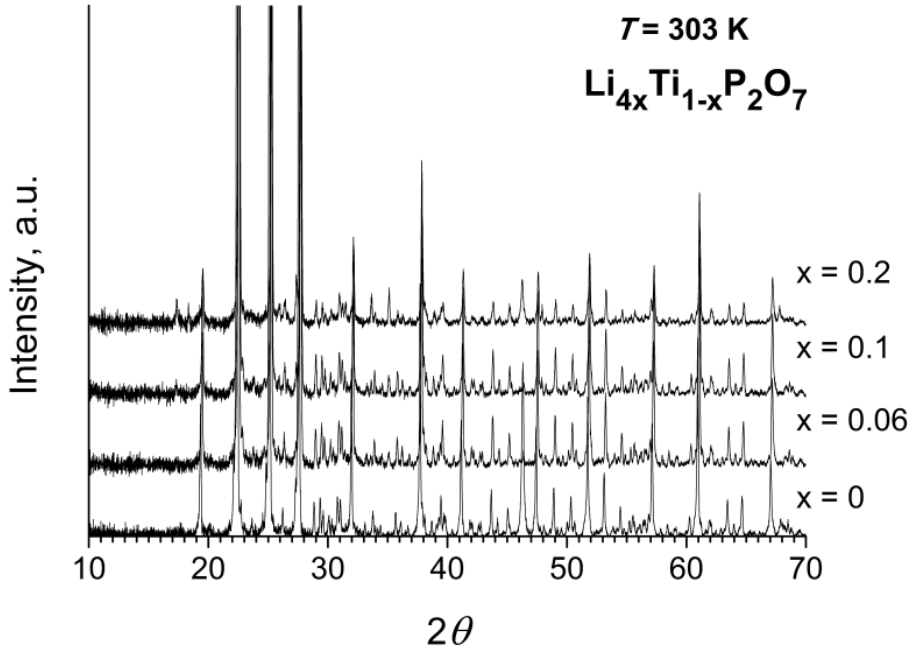

Figure 4.3.7 X-ray diffraction patterns of $Li_{4x}Ti_{1-x}P_2O_7$ (where x = 0, 0.06, 0.1, 0.2) powders.

Structure of $Li_4Ti_5O_{12}$, $Li_4Ti_{4.95}Nb_{0.05}O_{12}$ and $Li_4Ti_{4.95}Ta_{0.05}O_{12}$ [A7]. XRD patterns of LTO, LTO+Nb, LTO+Ta ceramics at heating and cooling in the temperature range (300-1270) K are displayed in Figure 4.3.8 a), b), c). Some changes of XRD patterns are found only in LTO ceramic.

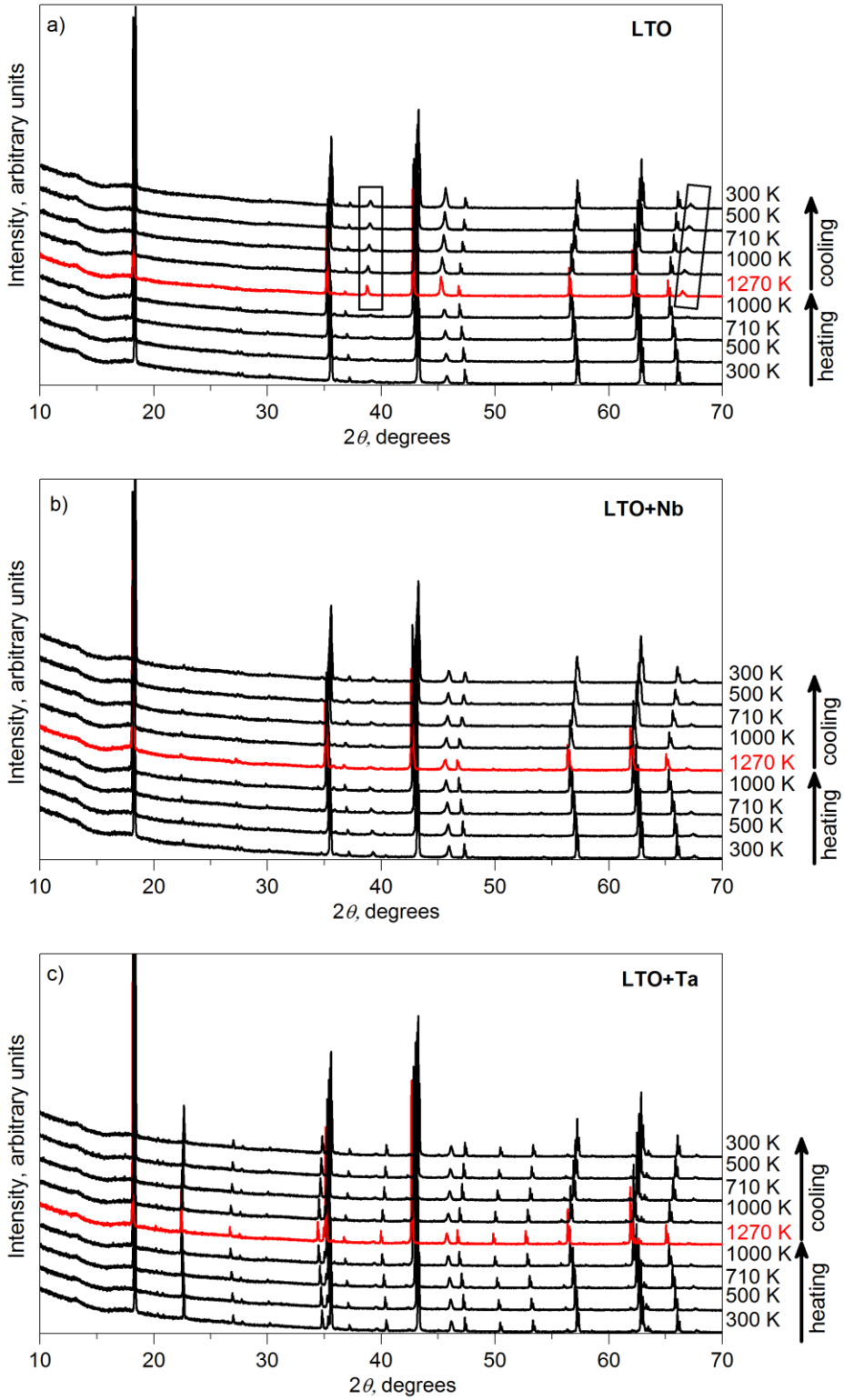

Figure 4.3.8 High-temperature XRD patterns for a) $Li_4Ti_5O_{12}$ (LTO), b) $Li_4Ti_{4.95}Nb_{0.05}O_{12}$ (LTO+Nb) and c) $Li_4Ti_{4.95}Ta_{0.05}O_{12}$ (LTO+Ta) ceramics.

These changes appear in the patterns in the temperature region (1000 – 1270) K and they remain after cooling LTO to room temperature. At room

temperature LTO, LTO+Nb, LTO+Ta powders belong to cubic symmetry with space group $Fd\bar{3}m$ as in [39]. At temperature T = 300 K lattice parameter a of LTO was found to be 8.358 Å. The lattice parameter a for LTO, where Ti^{4+} ions are substituted with Nb or Ta, is larger and was found to be 8.362Å. This can be caused by larger ionic radii of Nb^{5+} (0.64Å) and Ta^{5+} (0.64Å) compared with Ti^{4+} (0.605Å) [56].

Figure 4.3.9 shows temperature dependences of the lattice parameter of LTO, LTO+Nb and LTO+Ta. The lattice parameters increase linearly with temperature in the temperature range (300 – 1270) K, but lattice parameter of LTO shows some anomaly in the temperature range (1000 - 1270) K. During cooling to room temperature, lattice parameter of the sample decreases linearly, but the changes in XRD patterns remain after cooling to room temperature. The changes in XRD patterns and anomaly of lattice parameter in the temperature range (1000-1270) K, can be caused by the loss of the lattice oxygen from LTO compound.

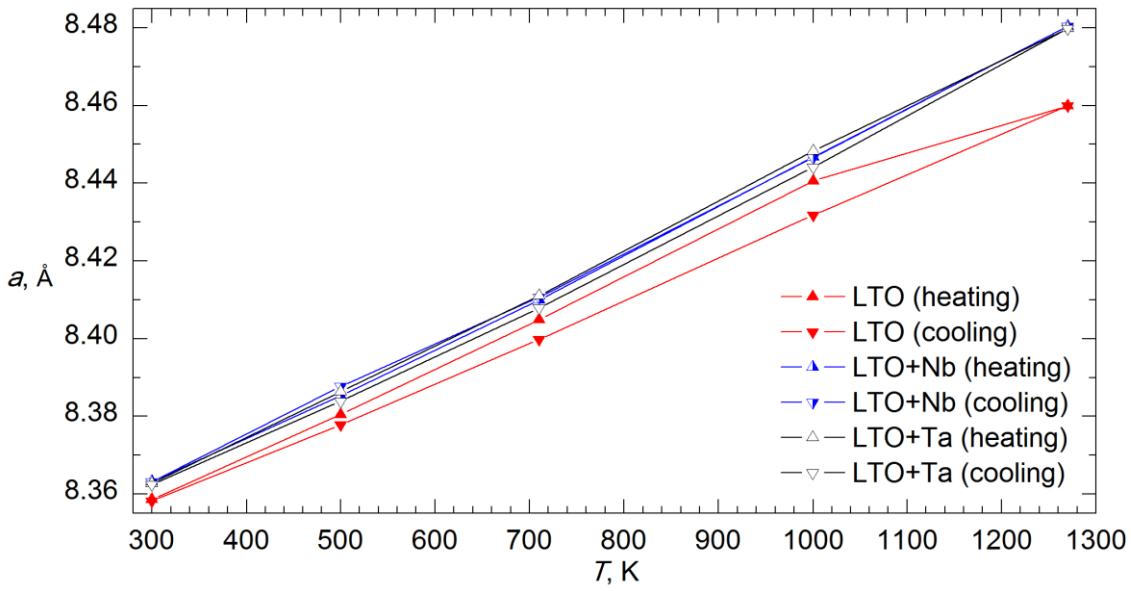

Figure 4.3.9 Temperature dependences of lattice parameter a for LTO, LTO+Nb, LTO+Ta ceramics.

4.4. Microstructure of lithium solid electrolytes investigated by SEM/EDX

Microstructure of sintered ceramics was investigated by SEM/EDX technique.

Microstructure and elemental composition of NASICON-type structure ceramics [A3]. SEM images of the surfaces of $Li_{1.8}Ti_{1.8}(PO_4)_3$ and $Li_3Ti_{1.5}(PO_4)_3$ ceramics are presented in Figure 4.4.1. The microstructure of both investigated ceramics is similar and their grain sizes varies in the range from 4μm to 10μm. Figure 4.4.2 shows EDX spectra for the grains of ceramics. The results of the investigation of elemental compositions has shown small amount of Al (0.585-0.457 wt. %-the error of this amount is found to be η ±0.035-0.033 wt.%) and Si (0.220-0.201 wt.% - η±0.32-0.031 wt.%) impurities in the grains of the investigated ceramics (see Figure 4.4.2). These impurities could be from substrates, which were used for sintering of the ceramics.

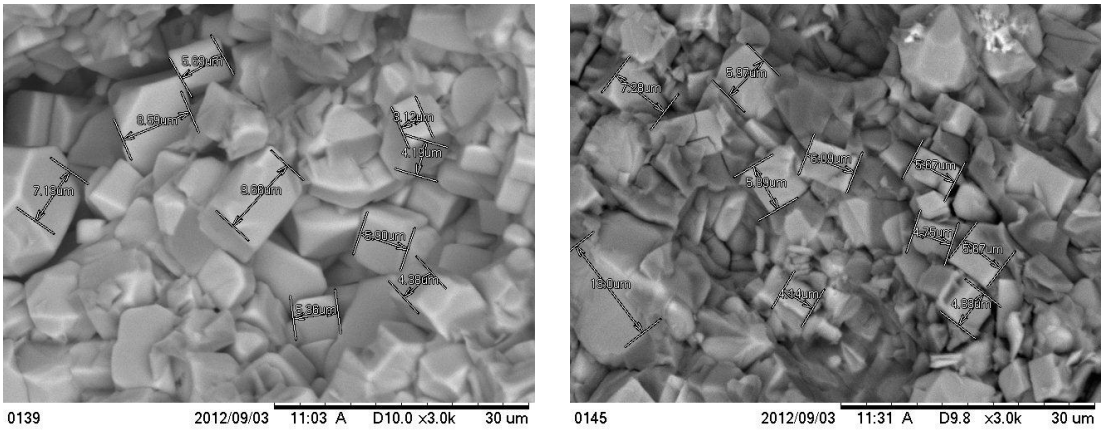

Figure 4.4.1 SEM images of a) $Li_{1.8}Ti_{1.8}(PO_4)_3$ and b) $Li_3Ti_{1.5}(PO_4)_3$ ceramics surfaces.

a)

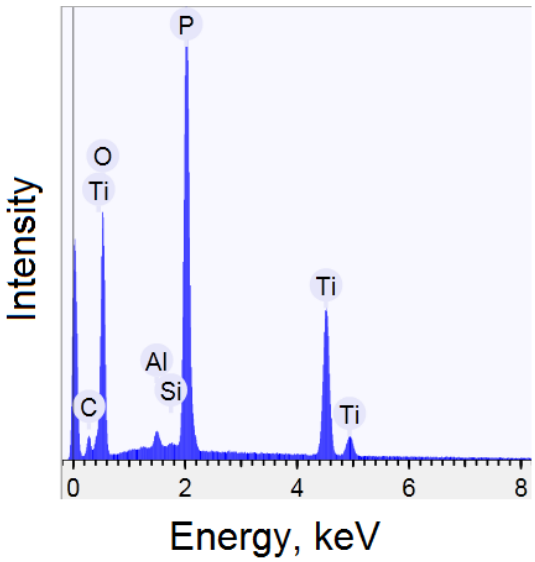

$Li_{1.8}Ti_{1.8}(PO_4)_3$	
El.	Weight %
C	10.246±0.365
O	52.208±0.344
Al	0.585±0.035
Si	0.220±0.032
P	19.882±0.167
Ti	16.860±0.165

b)

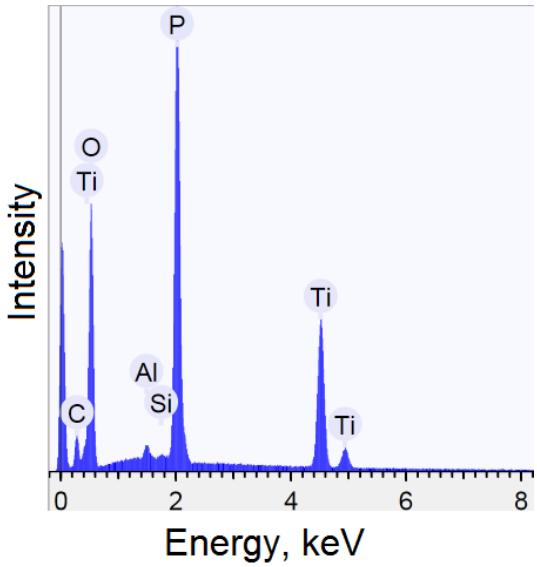

$Li_3Ti_{1.5}(PO_4)_3$	
El.	Weight %
C	12.908±0.370
O	52.186±0.347
Al	0.457±0.033
Si	0.201±0.031
P	18.587±0.160
Ti	15.660±0.157

Figure 4.4.2 EDX spectra of the grains of a) $Li_{1.8}Ti_{1.8}(PO_4)_3$ and b) $Li_3Ti_{1.5}(PO_4)_3$ ceramics surfaces.

Microstructure of $LiFeP_2O_7$ and $Li_{0.9}Fe_{0.9}Ti_{0.1}P_2O_7$ ceramics [A5]. SEM images of the surfaces of $LiFeP_2O_7$ and $Li_{0.9}Fe_{0.9}Ti_{0.1}P_2O_7$ ceramics are presented in Figure 4.4.3. The microstructure of both investigated ceramics is similar and their grain sizes varies in the range from approximately 5 μm to 30 μm.

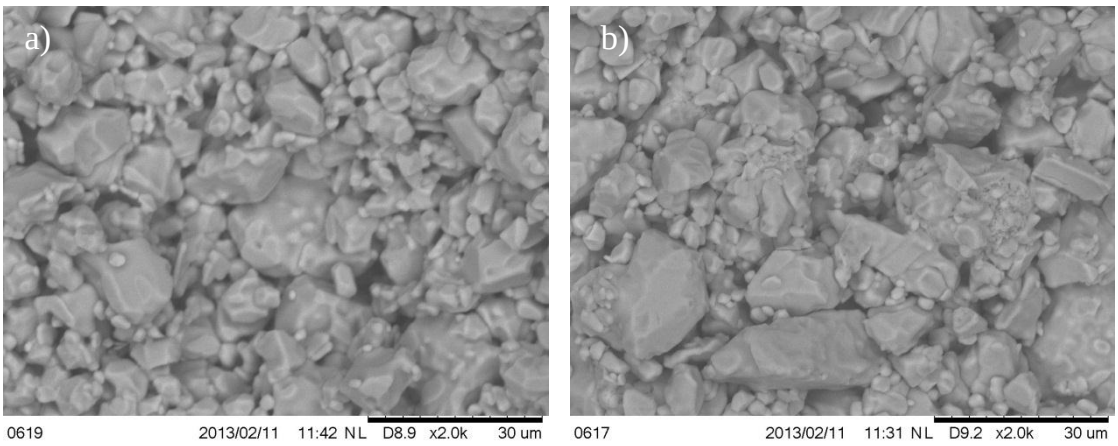

Figure 4.4.3 SEM images of $LiFeP_2O_7$ a) and $Li_{0.9}Fe_{0.9}Ti_{0.1}P_2O_7$ b) ceramics.

Figure 4.4.4 a) and b) shows EDX spectra of the investigated ceramics. The results of the investigation of elemental compositions from the square including grains and grain boundaries of the ceramics have shown small amount of Al ((3.11 – 4.50) ±0.12 wt. %) and Mg ((0.24 – 0.25) ± 0.07 wt. %) as impurities in the ceramics (see the insertions of . Figure 4.4.4 a), b)). For sintering of the investigated ceramics the Al_2O_3 substrates were used. So it is possible that Al from substrates can get into ceramic samples. The amount of Mg impurities doesn't exceed the allowed measurement error of the equipment. The ratio of P/Fe elements in the grains of $LiFeP_2O_7$ and $Li_{0.9}Fe_{0.9}Ti_{0.1}P_2O_7$ ceramics was found to be 2.32 and 1.86 respectively.

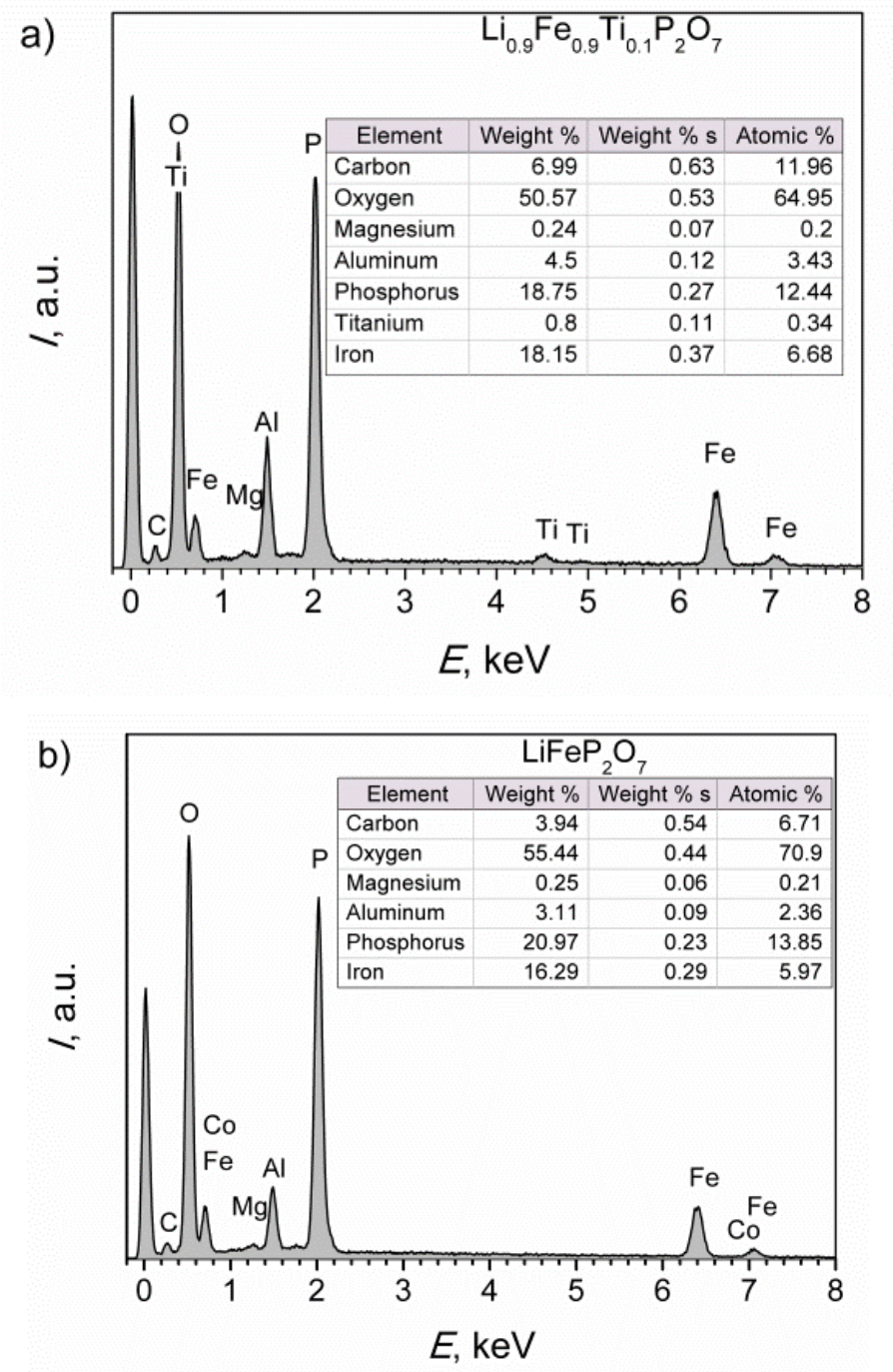

Figure 4.4.4 EDX spectra and elemental composition in weight and atomic percent of $Li_{0.9}Fe_{0.9}Ti_{0.1}P_2O_7$ (a)) and $LiFeP_2O_7$ (b)) ceramics.

SEM/EDX investigation of $LiFePO_4$ and $LiFePO_4$/C ceramics [A4]. SEM images of $LiFePO_4$ ceramic and $LiFePO_4$/C composite surfaces are presented in Figure 4.4.5 a) and b). The grain sizes in the investigated area of

$LiFePO_4$ ceramic surface vary in the range from approximately 3.1 μm to 8.5 μm. $LiFePO_4$/C composite has numerous microcracks.

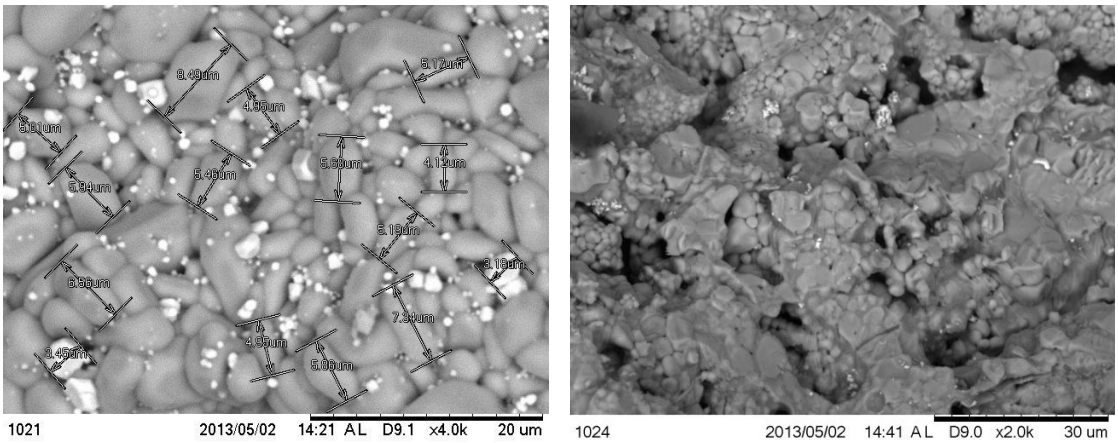

Figure 4.4.5 SEM images of $LiFePO_4$ (a) and $LiFePO_4$/C (b) ceramic surfaces.

Figure 4.4.6 a) and b) show EDX spectra. The results of the investigation of elemental composition of $LiFePO_4$ ceramics have shown small amount of Al, Na, Ti and Co impurities (see the insertions of Figure 4.4.6 a)). There is a small amount of Al impurities in $LiFePO_4$/C (Figure 4.4.6 b)). Al_2O_3 substrates used for sintering can be Al impurity source. If the amount of registered element is up to 1 at.% (Na, Ti and Co impurities), the most probable explanation is errors of the equipment.

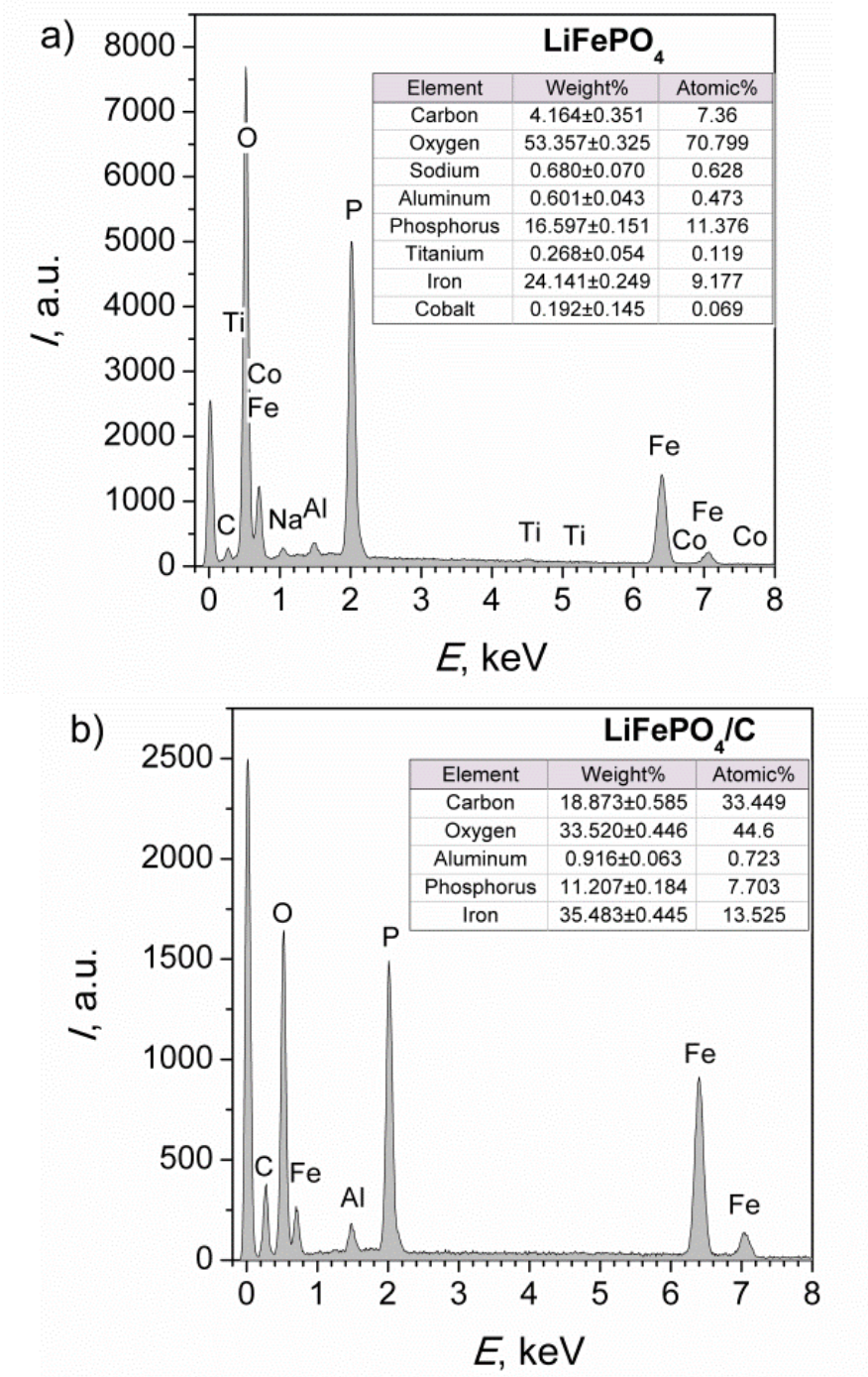

Figure 4.4.6 EDX spectra of $LiFePO_4$ (a) and $LiFePO_4$/C (b) ceramics.

4.5. Investigation of ceramics' surfaces by X-ray Photoelectron Spectroscopy

XPS analysis of Ti 2p core level [A1, A2, A3, A7]. The Ti 2p XP spectra of NASICON-type structure and LTO ceramics are shown in Figure 4.5.1. The Ti 2p XP spectra show the spin-orbit doublet of Ti $2p_{3/2}$ and Ti $2p_{1/2}$

as in [58, 62]. The $2p_{3/2}$ peaks at lower binding energies are associated with a lower oxidation state (Ti^{3+}). The peaks at higher $2p_{3/2}$ binding energies are associated with the Ti^{4+} state as in [63]. The Ti^{4+} valence state is typical for titanium. The Ti^{3+} valence state can be associated with oxygen deficiency in the investigated compounds as in $LiTi_2(PO_4)_3$ samples [64]. The amounts of Ti^{4+} and Ti^{3+} were determined by fitting the spectra and estimating areas under curves of each doublet. The summary of XPS investigation of Ti 2p core level is presented in Table 4.5.1.

It has been reported [62], that the binding energy splitting between $2p_{3/2}$ and $2p_{1/2}$ in $LiM_{0.05}Mn_{1.95}O_4$ (M = Ni, Fe and Ti) solid electrolytes is 5.4 eV. The splitting energy in $Li_{1.3}Al_yY_{x-y}Ti_{1.7}(PO_4)_3$ (x = 0.3; y = 0.1, 0.2) ceramics is 5.8 eV and does not depend on parameter y. While the splitting energy in $Li_{1+4x}Ti_{2-x}Nb_yP_{3-y}O_{12}$ (where x = 0.1, 0.2, 0.3; y =0, 0.1, 0.2, 0.3) depends on stoichiometric parameters x and y and is in the range between 5.8 eV and 6.1 eV. The splitting energies between lower and higher binding energy peaks in $Li_{1+4x}Ti_{2-x}(PO_4)_3$ (where x = 0.2, 0.5) are 5.6 eV and 5.7 eV respectively. Also the increase of parameter x in $Li_{1+4x}Ti_{2-x}(PO_4)_3$ is associated with the increase of Ti^{4+} amount. So a ratio Ti^{4+}/Ti^{3+} changes from 1.5 for a compound with x = 0.2 to 1.9 for a compound with x = 0.5. The splitting energy of Ti 2p core level XPS of investigated spinels are in the range from 5.5 eV to 5.9 eV. The substitution of LTO by Nb^{5+} and Ta^{5+} leads the increase of amount of titanium ions in Ti^{3+}valence state and decrease the amount of ions in Ti^{4+}valence state in the ceramics.

Table 4.5.1 Summary of X-ray photoelectron spectroscopy results of some NASICON and spinel ceramics for Ti 2p core level.

Compound	Binding energy, eV	Splitting energy, eV	Amount, at.%	Chi square χ^2
$Li_{1.3}Al_{0.1}Y_{0.2}Ti_{1.7}(PO_4)_3$	458.9	5.9	48.3	0.84
	459.8	5.9	51.7	
$Li_{1.3}Al_{0.2}Y_{0.1}Ti_{1.7}(PO_4)_3$	459.1	5.8	46.4	0.86
	459.9	5.9	53.6	
$Li_{1.4}Ti_{1.9}P_3O_{12}$	458.5	5.8	67.2	1.1
	459.7	5.8	32.8	
$Li_{1.4}Ti_{1.9}Nb_{0.1}P_{2.9}O_{12}$	458.8	5.8	49.9	1.1
	459.9	5.8	50.1	
$Li_{1.8}Ti_{1.8}Nb_{0.2}P_{2.8}O_{12}$	459.3	5.7	77.0	0.89
	460.2	5.8	23.0	
$Li_{2.2}Ti_{1.7}Nb_{0.3}P_{2.7}O_{12}$	459.1	6.1	29.3	0.69
	460.1	6.1	70.7	
$Li_{1.8}Ti_{1.8}(PO_4)_3$	459.5	5.6	39.1	0.6
	460.4	5.7	60.9	
$Li_3Ti_{1.5}(PO_4)_3$	459.4	5.6	34.7	0.5
	460.4	5.7	65.3	
$Li_4Ti_5O_{12}$	457.7	5.5	23.5	1.2
	458.5	5.9	76.5	
$Li_4Ti_{4.95}Nb_{0.05}O_{12}$	457.4	5.8	33.9	1.2
	458.5	5.9	66.1	
$Li_4Ti_{4.95}Ta_{0.05}O_{12}$	457.5	5.6	24.6	1.3
	458.4	5.8	75.4	

a)

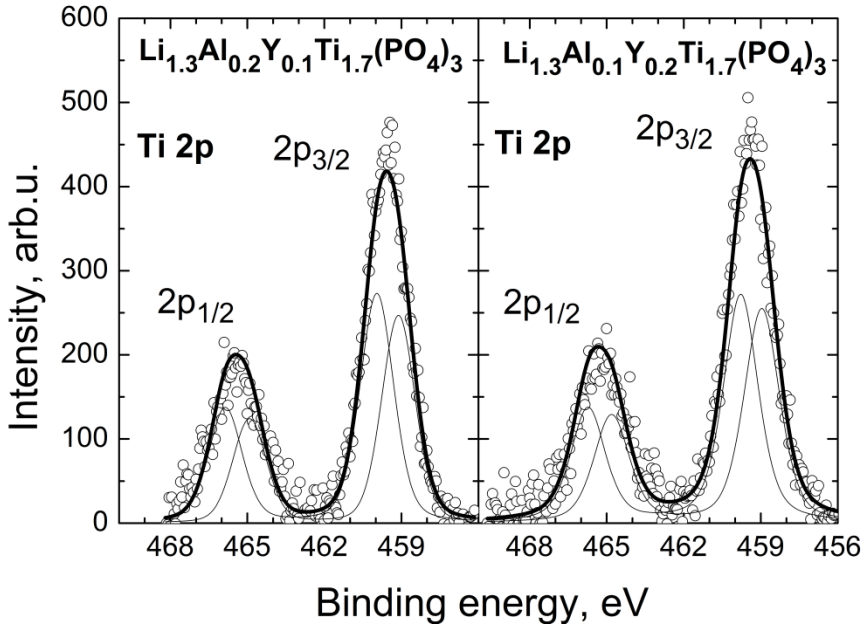

b)

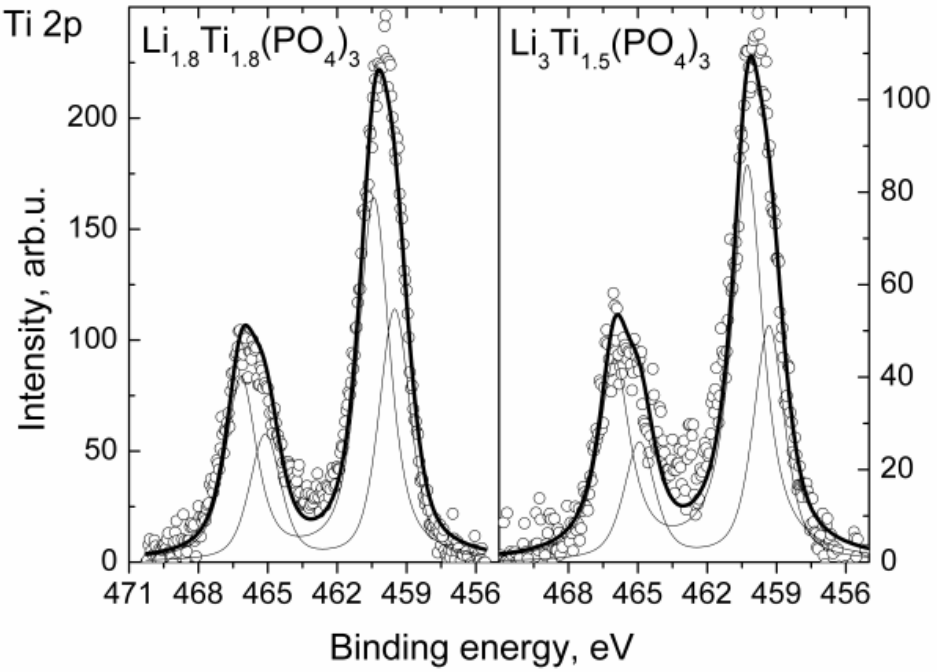

Figure 4.5.1 Ti 2p core level XPS for $Li_{1.3}Al_yY_{x-y}Ti_{1.7}(PO_4)_3$ (x = 0.3; y = 0.1, 0.2) (a), $Li_{1+4x}Ti_{2-x}(PO_4)_3$ (where x = 0.2, 0.5) (b) $Li_{1+4x}Ti_{2-x}Nb_yP_{3-y}O_{12}$ (where x = 0.1, 0.2, 0.3; y =0, 0.1, 0.2, 0.3) (c) and LTO (d) ceramics at room temperature.

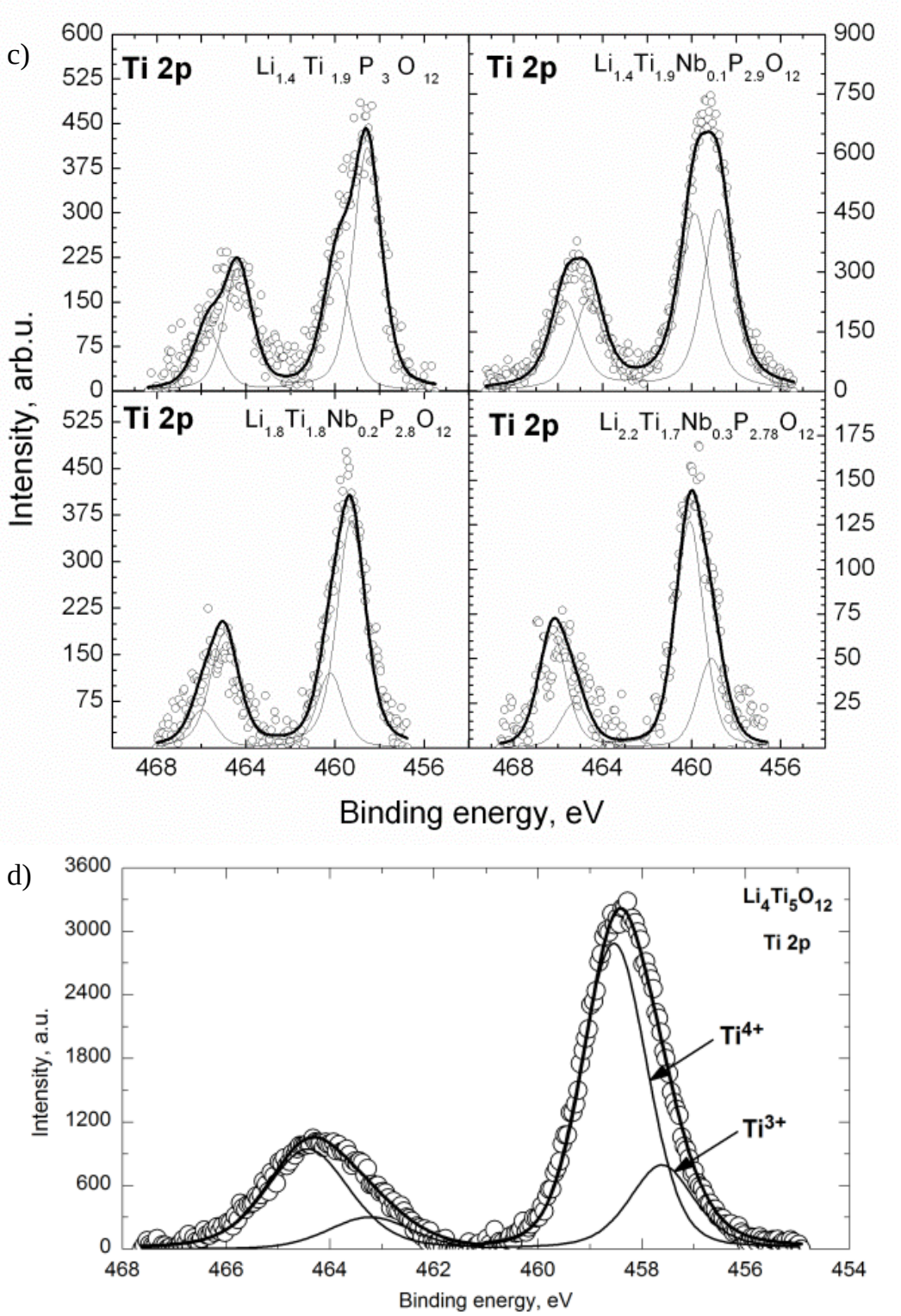

Figure 4.5.2 (continued).

The P 2p core level XPS of the investigated ceramics [A1, A2, A3, A4, A5]. The fitting patterns of the P 2p core level XP spectra are shown in Figure 4.5.3. The best fit of P 2p core level XPS for all investigated ceramics containing phosphorus was obtained when P $2p_{3/2}$ XP spectra was

deconvoluted into two peaks. These peaks can be associated with P^{5+} and P^{3+} states in the investigated ceramics. The P^{5+} and P^{3+} states in the ceramics can be associated with group PO_4^{3-} and group PO_3^{-} respectively. The binding energy in $Li_{1.3}Al_yY_{x-y}Ti_{1.7}(PO_4)_3$ (x = 0.3; y = 0.1, 0.2) ceramics depends on stoichiometric parameter y of the compounds. The increase of y parameter shifts the peaks to lower binding energy. The peaks at binding energies 132.7 eV (y = 0.2), 134.6eV (y = 0.1) are attributed to group PO_4^{3-} as in [64] and the peaks at binding energy 133.4 eV can be attributed to PO_3^{-} group as in [58] (binding energy 133.9 eV). The splitting energy of P 2p spectra in $Li_{1.3}Al_yY_{x-y}Ti_{1.7}(PO_4)_3$ (x = 0.3; y = 0.1, 0.2) is 1.0 eV and does not depend on parameter y. The summary of the investigation of P 2p core level XPS of the ceramics are presented in the Table 4.5.2.

a)

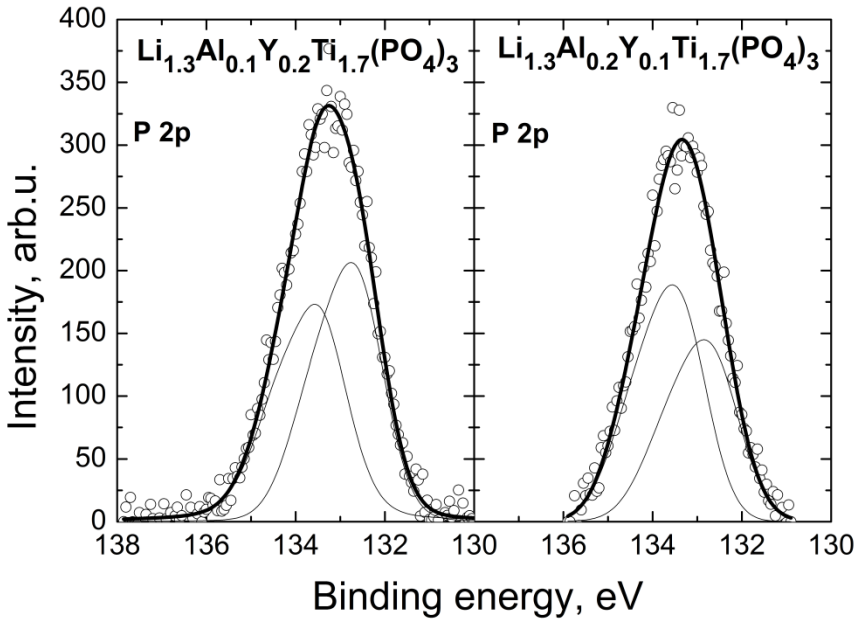

Figure 4.5.3 P 2p core level XPS for $Li_{1.3}Al_yY_{x-y}Ti_{1.7}(PO_4)_3$ (x = 0.3; y = 0.1, 0.2) (a), $Li_{1+4x}Ti_{2-x}(PO_4)_3$ (where x = 0.2, 0.5) (b) $Li_{1+4x}Ti_{2-x}Nb_yP_{3-y}O_{12}$ (where x = 0.1, 0.2, 0.3; y =0, 0.1, 0.2, 0.3) (c) $LiFePO_4$ (d) and $Li_{1-x}Fe_{1-x}Ti_xP_2O_7$ (x= 0, 0.1) (e) ceramics at room temperature.

b)

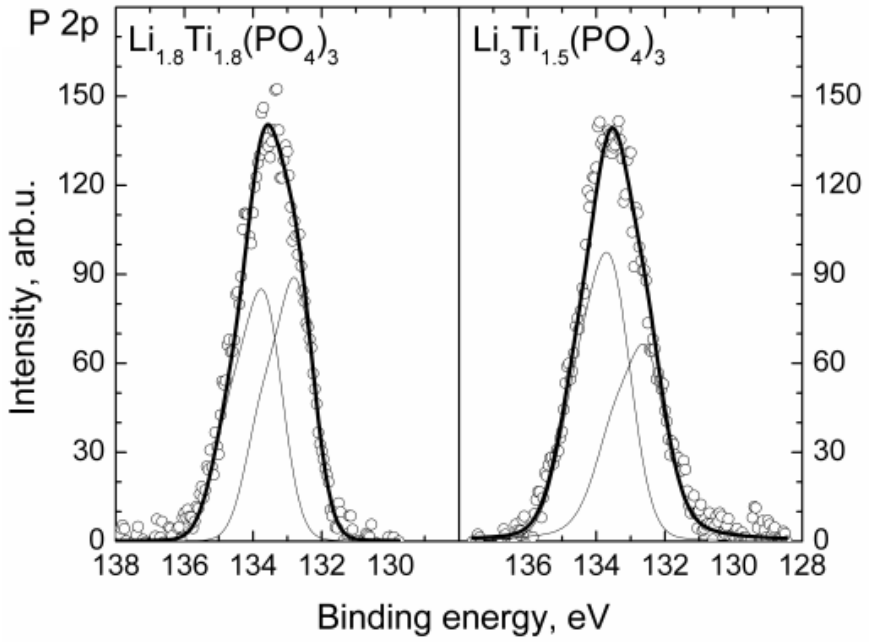

c)

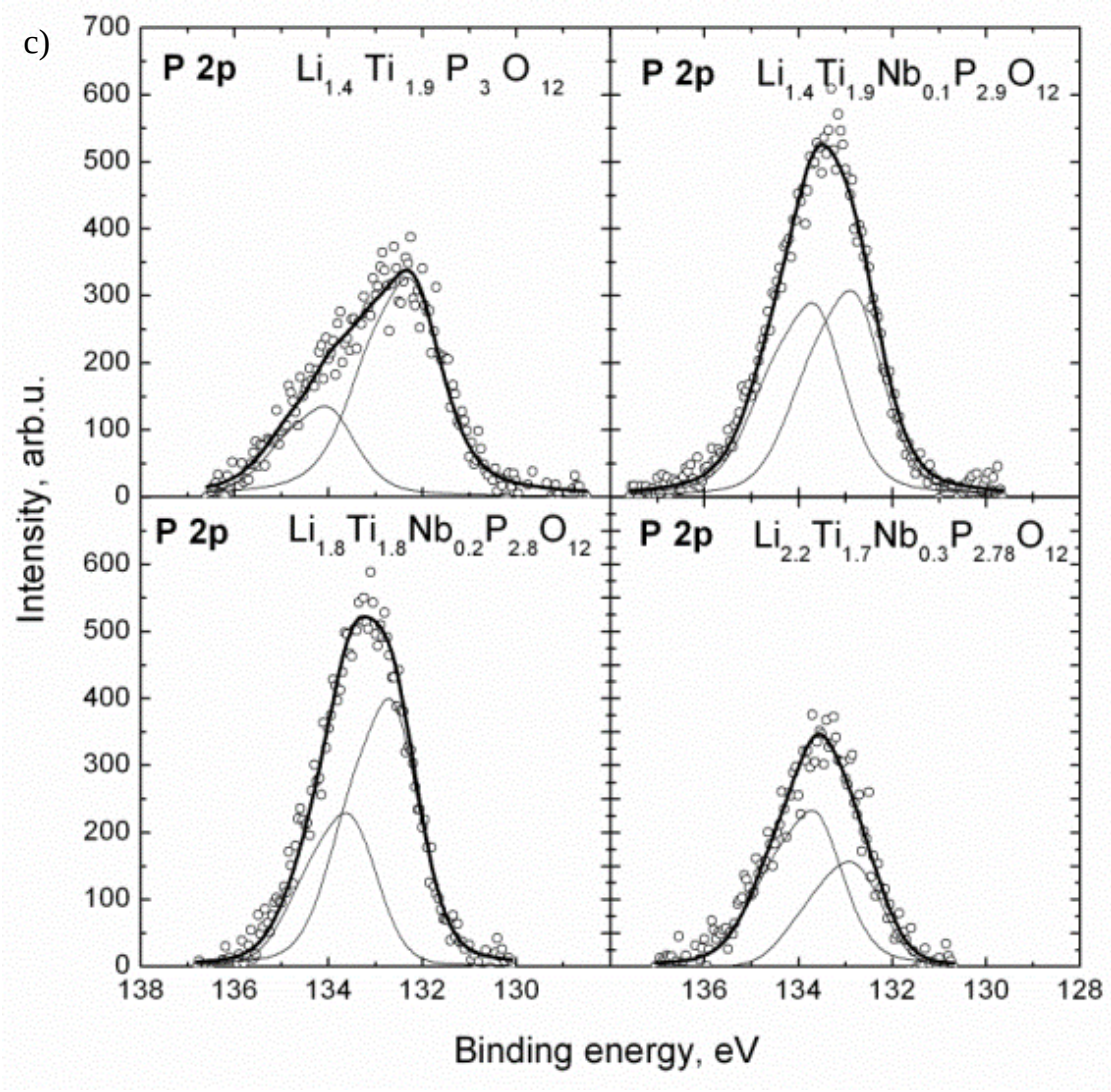

Figure 4.5.4 (continued).

d)

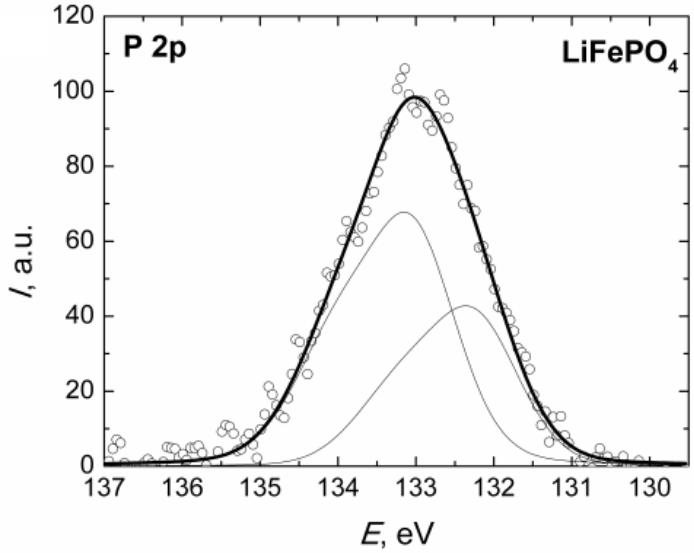

e)

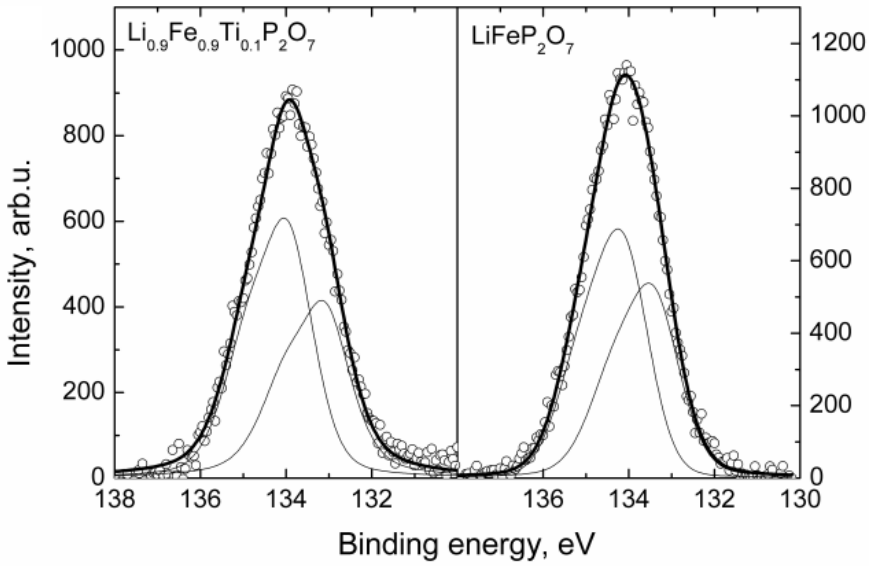

Figure 4.5.5 (continued).

Table 4.5.2 Summary of X-ray photoelectron spectroscopy analysis results of some lithium ion conducting ceramics for P 2p core level.

Compound	Binding energy, eV	Splitting energy, eV	Amount, at.%	Chi square χ^2
$Li_{1.3}Al_{0.1}Y_{0.2}Ti_{1.7}(PO_4)_3$	132.6	1.0	52.0	0.58
	133.4	1.0	48.0	
$Li_{1.3}Al_{0.2}Y_{0.1}Ti_{1.7}(PO_4)_3$	132.7	1.0	44.2	0.65
	133.4	1.0	55.8	
$Li_{1.4}Ti_{1.9}P_3O_{12}$	132.2	0.95	72.1	1.46
	133.9	0.95	27.9	
$Li_{1.4}Ti_{1.9}Nb_{0.1}P_{2.9}O_{12}$	132.8	1.0	50.4	1.04
	133.6	1.0	49.6	
$Li_{1.8}Ti_{1.8}Nb_{0.2}P_{2.8}O_{12}$	132.6	0.95	64.9	1.17
	133.5	0.95	35.1	
$Li_{2.2}Ti_{1.7}Nb_{0.3}P_{2.7}O_{12}$	132.8	1.0	36.6	1.4
	133.6	1.0	63.4	
$Li_{1.8}Ti_{1.8}(PO_4)_3$	132.7	1.0	50.4	0.8
	133.6	1.0	49.6	
$Li_3Ti_{1.5}(PO_4)_3$	132.5	1.0	43.4	0.7
	133.6	1.0	56.6	
$LiFePO_4$	132.2	1.0	37.8	0.6
	133.1	1.0	62.2	
$LiFePO_4$/C	135.0	1.0	45.3	0.8
	133.2	1.0	54.7	
$Li_{0.9}Fe_{0.9}Ti_{0.1}P_2O_7$	133.1	1.0	42.6	0.9
	134.0	1.0	57.4	
$LiFeP_2O_7$	133.4	1.0	45.6	0.8
	134.1	1.0	54.4	

XPS analysis of O 1s core level [A1, A2, A3, A4, A5, A7]. The O 1s core level XPS spectra for investigated ceramics surfaces are shown in Figure 4.5.6 and the results of the O 1s core level XPS investigation are summarized in Table 4.5.3. The highest intensity peaks can be attributed to lattice oxygen. For example, in $Li_{1.3}Al_yY_{x-y}Ti_{1.7}(PO_4)_3$ (x = 0.3; y = 0.1, 0.2) the binding energy for this peak does not depend on parameter y and it is located at 531.0 eV. The O 1s spectra for all LTO based ceramics display asymmetric shapes, which could be fitted with an intense component and two lower intensity peaks. The highest intensity peaks for LTO, LTO+Nb and LTO+Ta are centered at binding energies 529.2 eV (amount 49.1 at. %), 529.0 eV (55.4 at. %) and 528.9 eV (73.0 at. %) respectively. The results show that insertion of Nb and Ta into LTO stimulates the increase of high intensity components and decrease of lower intensity components. The other O 1s core level peaks in all the investigated ceramics can be assigned to metallic oxides, hydroxyl groups, chemisorbed oxygen or oxygen in H_2O as in [60, 65, 66].

a)

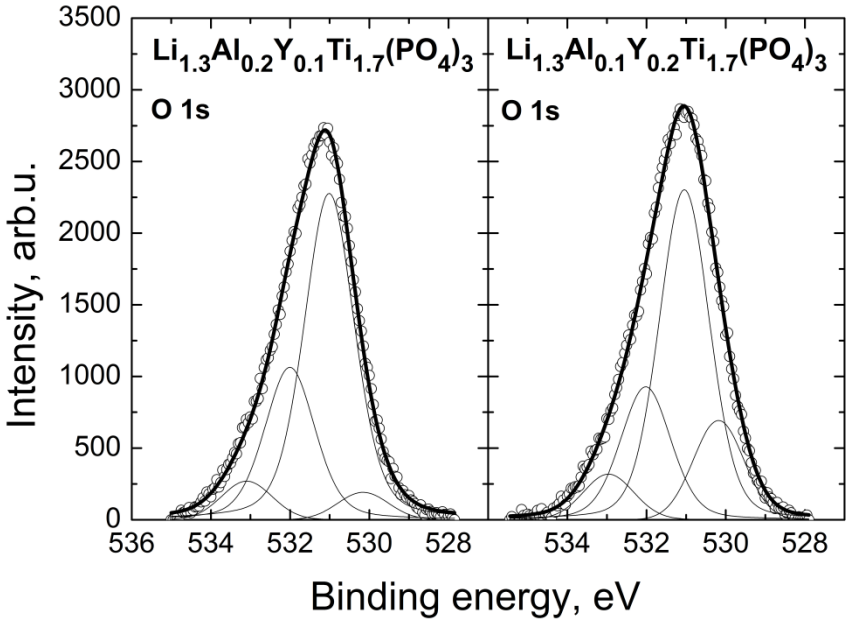

Figure 4.5.6 O 1s core level XPS for $Li_{1.3}Al_yY_{x-y}Ti_{1.7}(PO_4)_3$ (x = 0.3; y = 0.1, 0.2) (a), $Li_{1+4x}Ti_{2-x}(PO_4)_3$ (where x = 0.2, 0.5) (b) $Li_{1+4x}Ti_{2-x}Nb_yP_{3-y}O_{12}$ (where x = 0.1, 0.2, 0.3; y =0, 0.1, 0.2, 0.3) (c) $LiFePO_4$ (d), $LiFePO_4$/C (e), $Li_{1-x}Fe_{1-x}Ti_xP_2O_7$ (x= 0, 0.1) (f) and $Li_4Ti_5O_{12}$ (g) ceramics at room temperature.

b)

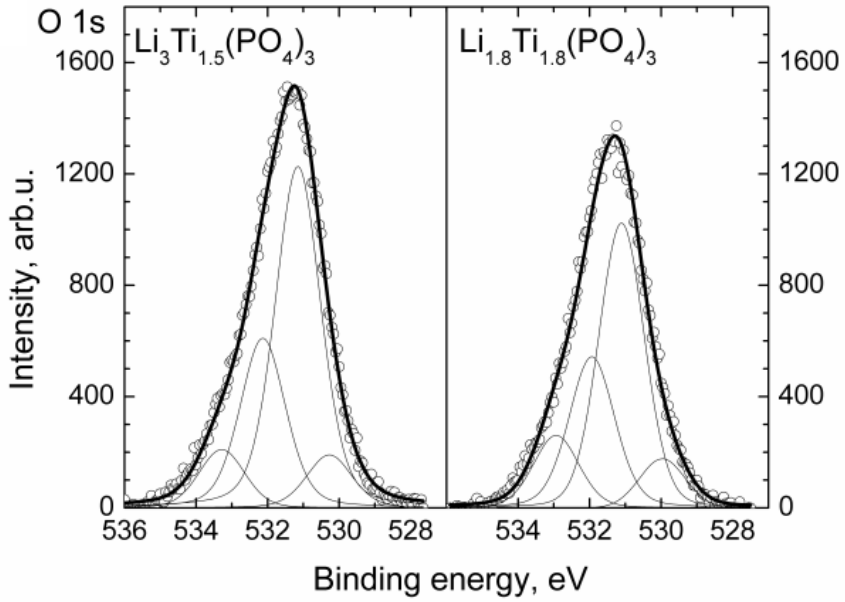

c)

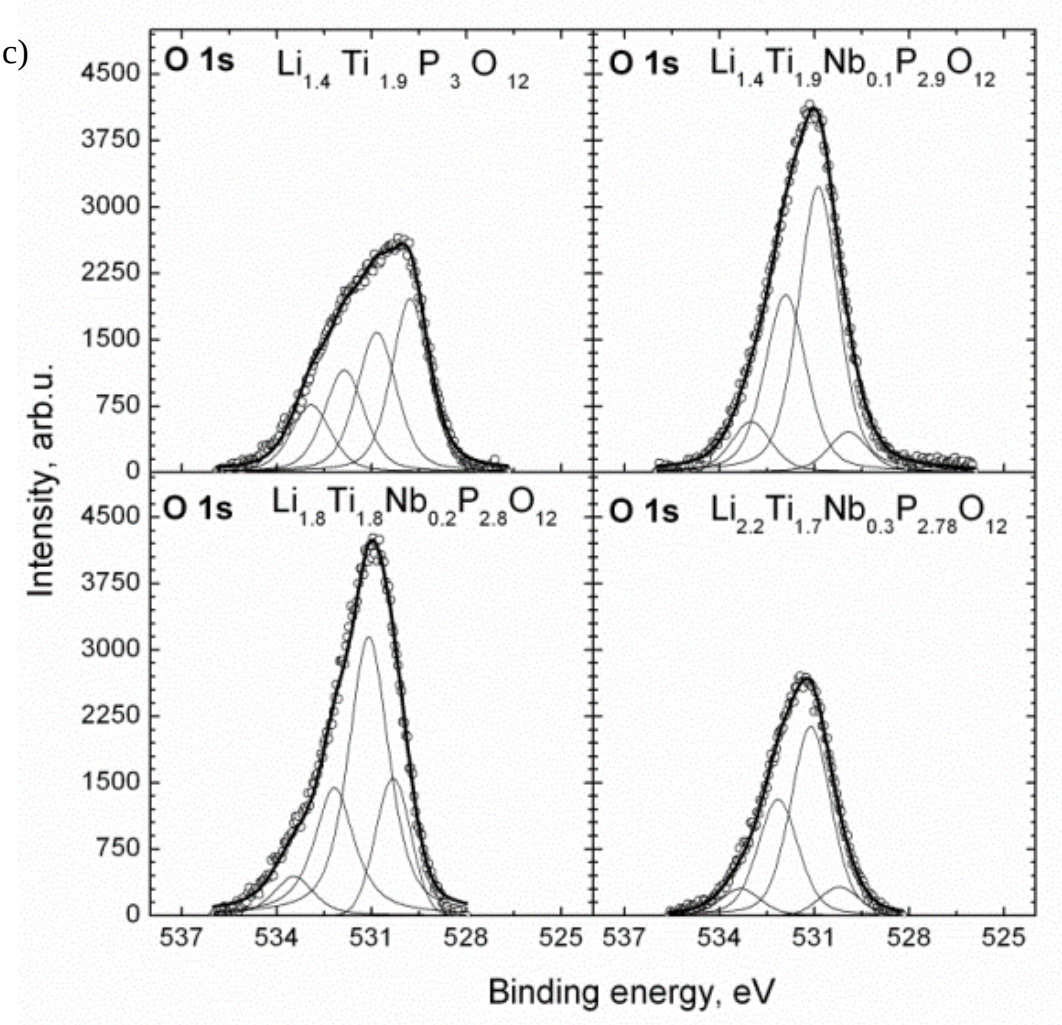

Figure 4.5.7 (continued).

d)

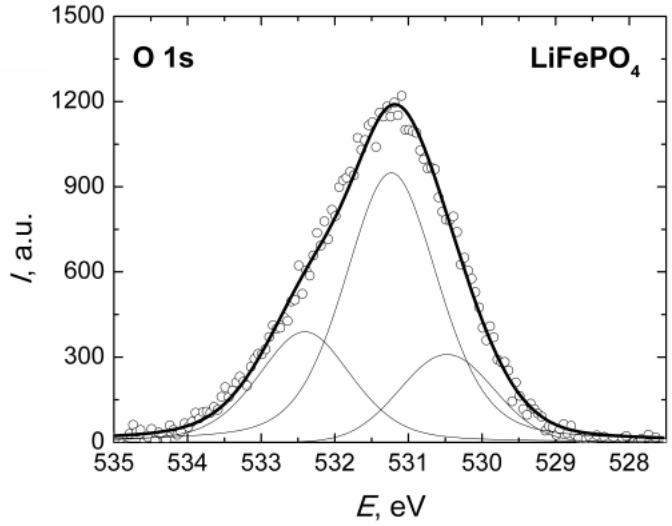

e)

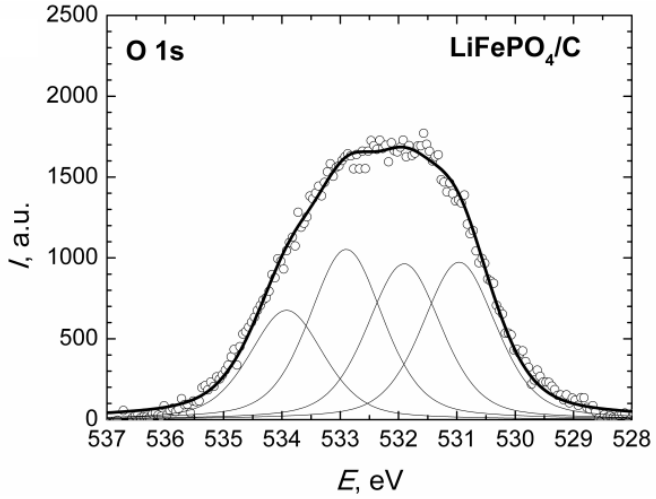

f)

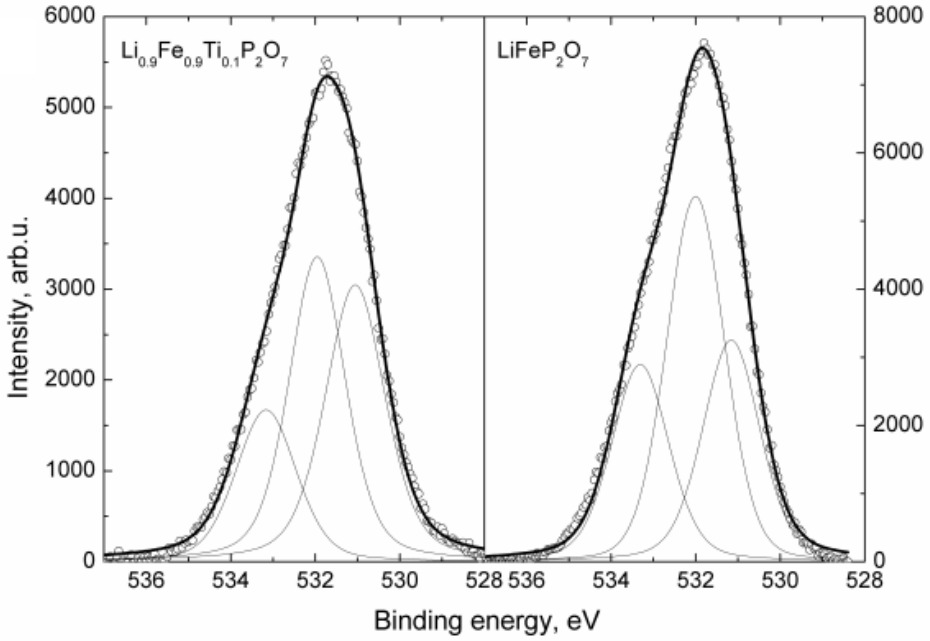

Figure 4.5.8 (continued).

g)

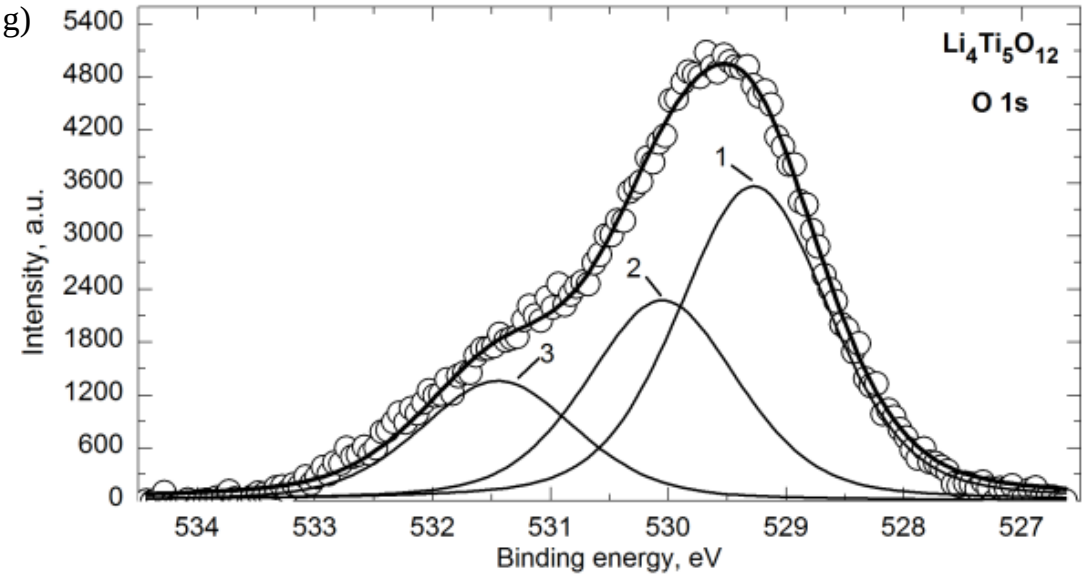

Figure 4.5.9 (continued).

Table 4.5.3 Summary of X-ray photoelectron spectroscopy results of some lithium ion conducting ceramics for O 1s core level.

Compound	Binding energy, eV	Amount, at.%	Chi square χ^2
$Li_{1.3}Al_{0.1}Y_{0.2}Ti_{1.7}(PO_4)_3$	530.1	15.1	0.93
	531.0	55.1	
	532.0	22.6	
	533.0	7.2	
$Li_{1.3}Al_{0.2}Y_{0.1}Ti_{1.7}(PO_4)_3$	530.1	4.5	0.89
	531.0	60.8	
	532.0	28.4	
	533.1	6.4	

Table 4.5.4 (continued).

Compound	Binding energy, eV	Amount, at.%	Chi square χ^2
$Li_{1.4}Ti_{1.9}P_3O_{12}$	529.8	34.3	2.19
	530.8	29.7	
	531.9	21.7	
	532.9	14.3	
$Li_{1.4}Ti_{1.9}Nb_{0.1}P_{2.9}O_{12}$	529.9	7.2	1.7
	530.9	50.9	
	532.0	32.7	
	533.0	9.2	
$Li_{1.8}Ti_{1.8}Nb_{0.2}P_{2.8}O_{12}$	530.3	17.2	3.7
	531.1	50.6	
	532.2	25.3	
	533.5	6.9	
$Li_{2.2}Ti_{1.7}Nb_{0.3}P_{2.7}O_{12}$	530.2	7.0	1.6
	531.1	52.8	
	532.2	32.6	
	533.3	7.6	
$Li_{1.8}Ti_{1.8}(PO_4)_3$	530.3	8.5	0.9
	531.2	55.1	
	532.1	27.4	
	533.3	8.0	
$Li_3Ti_{1.5}(PO_4)_3$	530.0	8.2	1.2
	531.1	50.6	
	532.0	28.1	
	533.2	13.1	

Table 4.5.5 (continued).

Compound	Binding energy, eV	Amount, at.%	Chi square χ^2
$LiFePO_4$	530.4	16.6	1.74
	531.2	59.2	
	532.4	24.2	
$LiFePO_4/C$	530.9	26.6	2.1
	531.9	26.2	
	532.9	28.7	
	533.9	18.5	
$Li_{0.9}Fe_{0.9}Ti_{0.1}P_2O_7$	531.0	39.2	1.9
	532.0	40.2	
	533.2	20.6	
$LiFeP_2O_7$	531.2	28.9	3.4
	532.1	45.4	
	533.2	25.6	
$Li_4Ti_5O_{12}$	529.2	49.1	3.6
	530.0	31.6	
	531.4	19.3	
$Li_4Ti_{4.95}Nb_{0.05}O_{12}$	529.0	55.4	3.6
	530.0	35.8	
	531.4	8.8	
$Li_4Ti_{4.95}Ta_{0.05}O_{12}$	528.9	73.0	3.3
	529.5	22.4	
	531.2	4.6	

The Li 1s core level XPS of the investigated ceramics [A1, A2, A3]. The Li 1s core level XPS spectra for investigated ceramics surfaces are shown in Figure 4.5.4. It was impossible to obtain high intensity Li 1s core level XP spectra of investigated ceramics. So the fitting of the patterns was very complicated. Li 1s core level XP spectra of all $Li_{1+4x}Ti_{2-x}Nb_yP_{3-y}O_{12}$ (where x =

0.1, 0.2, 0.3; y = 0, 0.1, 0.2, 0.3) ceramics have been deconvoluted into two peaks. The binding energies of Li 1s spectra depend on stoichiometric parameters x and y of the investigated compounds (see Table 4.5.6). It is reported that the Li 1s core level XPS peak is at binding energy around 55.8 eV [67]. For the $Li_{0.8}CoO_4$ composition single Li 1s peak has been observed at 55.4 eV but for Li rich compositions such as $LiCoO_4$ and $Li_{1.2}CoO_4$ an intense peak is at 55.4 eV, and a shoulder peak around 55.05 eV has also been observed [68]. The authors concluded that Li ions occupy two different positions. The results of the NMR study of $LiTi_{2-x}Zr_x(PO_4)_3$ composition have shown that Li ions occupy two different positions in the lattice too [69].

Table 4.5.6 Summary of X-ray photoelectron spectroscopy results of some lithium ion conducting ceramics for Li 1s core level.

Compound	Binding energy, eV	Amount, at.%	Chi square χ^2
$Li_{1.3}Al_{0.1}Y_{0.2}Ti_{1.7}(PO_4)_3$	54.7	100	0.3
$Li_{1.3}Al_{0.2}Y_{0.1}Ti_{1.7}(PO_4)_3$	54.7	39.2	0.38
	55.2	60.8	
$Li_{1.4}Ti_{1.9}P_3O_{12}$	54.6	71.7	0.34
	55.7	28.3	
$Li_{1.4}Ti_{1.9}Nb_{0.1}P_{2.9}O_{12}$	54.5	36.1	0.35
	55.5	63.9	
$Li_{1.8}Ti_{1.8}Nb_{0.2}P_{2.8}O_{12}$	54.4	85	0.39
	55.4	15	
$Li_{2.2}Ti_{1.7}Nb_{0.3}P_{2.7}O_{12}$	54.4	81.7	0.1
	55.4	18.3	
$Li_{1.8}Ti_{1.8}(PO_4)_3$	55.3	100	0.1
$Li_3Ti_{1.5}(PO_4)_3$	55.0	100	0.2

Only a single peak of Li 1s core level XPS was found for the surfaces of $Li_{1+4x}Ti_{2-x}(PO_4)_3$ (where x = 0.2, 0.5) ceramics. These results can be assigned to the fact that in the lattice of the compounds one energy position for Li ions

dominates. The binding energy of Li 1s core level XPS changed in the range from 55.3 to 55.0 eV and these results accord with [70]. The low intensity of the Li 1s XP spectra of $Li_{1.3}Al_yY_{x-y}Ti_{1.7}(PO_4)_3$ (x = 0.3; y = 0.1, 0.2) ceramics does not lead to the conclusions about the number of Li-ion positions in these ceramics. It was impossible to analyze Li 1s core level XP spectra of $Li_{1-x}Fe_{1-x}Ti_xP_2O_7$ (x= 0, 0.1) ceramics, as these spectra overlap with Fe 3p spectra.

a)

b)

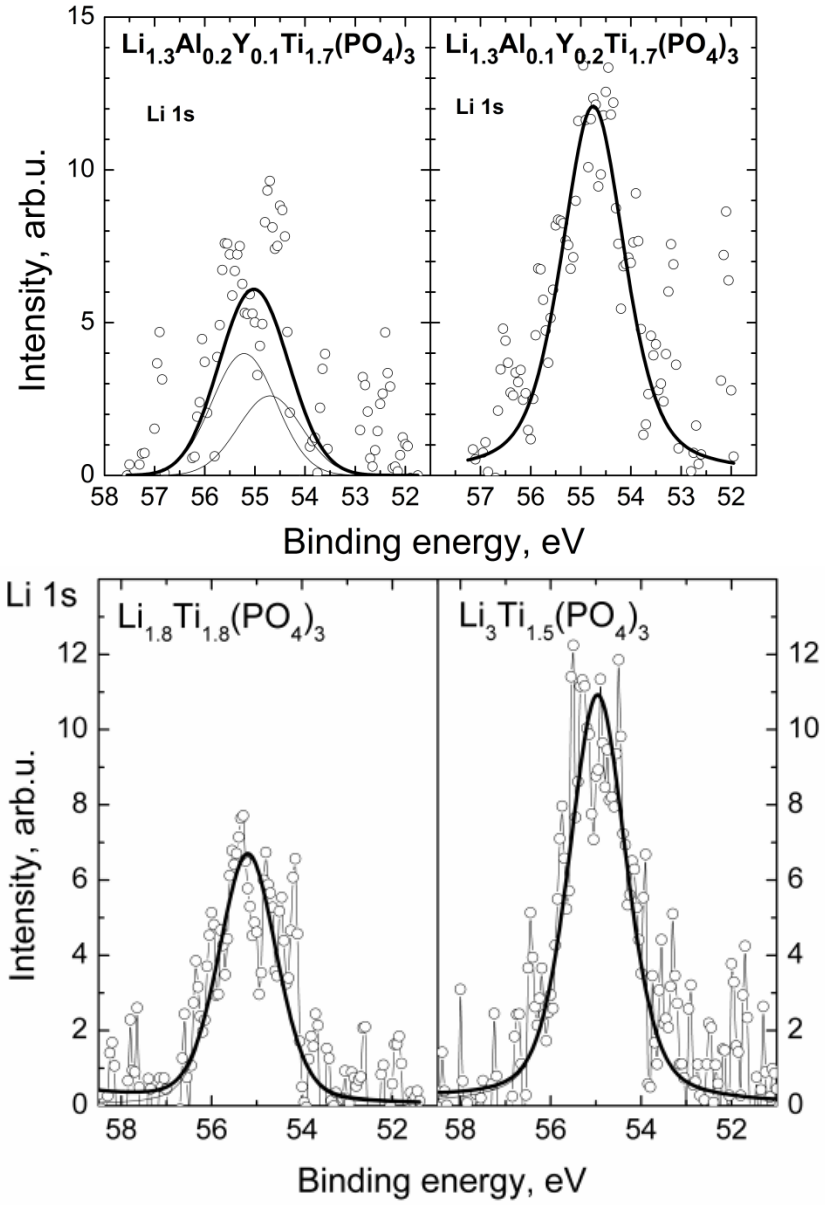

Figure 4.5.10 Li 1s core level XPS for $Li_{1.3}Al_yY_{x-y}Ti_{1.7}(PO_4)_3$ (x = 0.3; y = 0.1, 0.2) (a), $Li_{1+4x}Ti_{2-x}(PO_4)_3$ (where x = 0.2, 0.5) (b) and $Li_{1+4x}Ti_{2-x}Nb_yP_{3-y}O_{12}$ (where x = 0.1, 0.2, 0.3; y =0, 0.1, 0.2, 0.3) (c) ceramics at room temperature.

c)

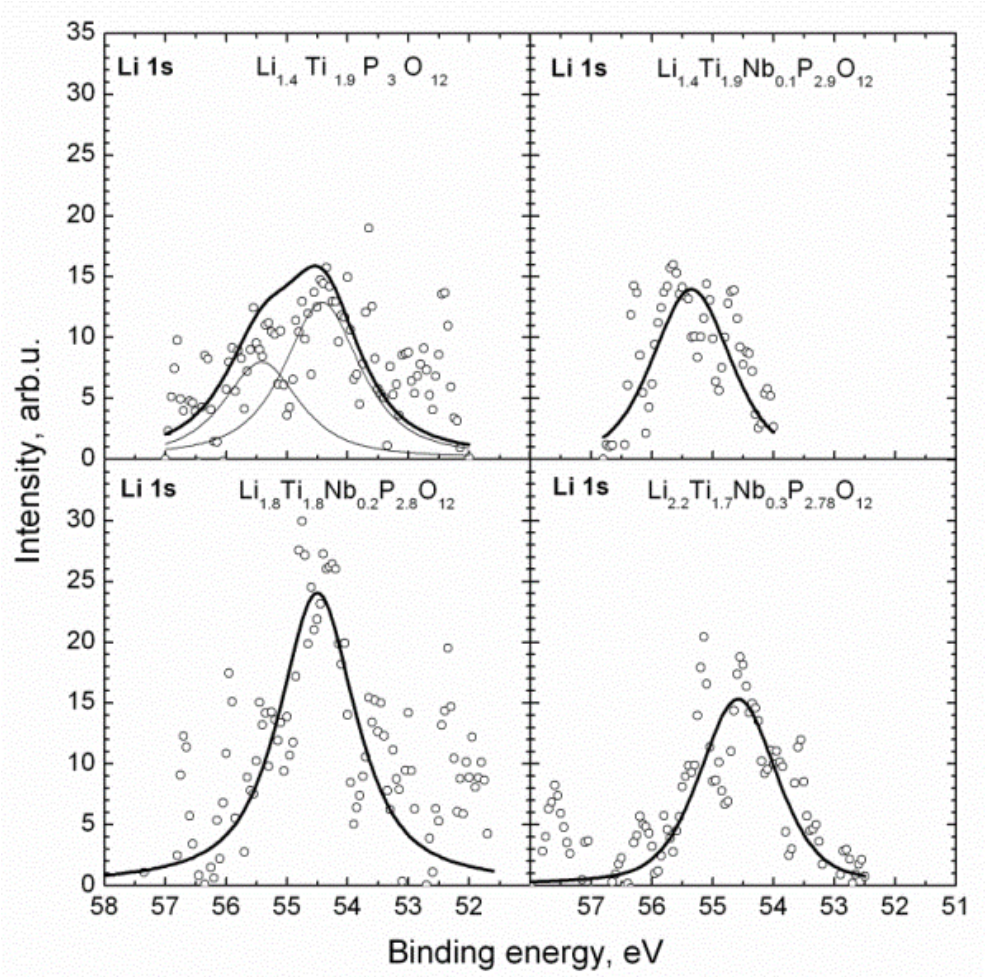

Figure 4.5.11 (continued).

XPS analysis of Y 3d core level [A2]. The XPS spectra of $Li_{1.3}Al_yY_{x-y}Ti_{1.7}(PO_4)_3$ (x = 0.3; y = 0.1, 0.2) ceramics show spin-orbit doublets of Y $3d_{5/2}$ and Y $3d_{3/2}$ (see Figure 4.5.12). The binding energies of Y $3d_{5/2}$ were found to be 158.5 eV (y = 0.2), 158.7 eV (y = 0.1). The splitting energy between Y $3d_{5/2}$ and Y $3d_{3/2}$ core level peaks is 1.85eV. According to [65], this splitting is 1.73 eV in the Y_2O_3-Al_2O_3-SiO_2 system. Each of the spin-orbit doublet lines have been deconvoluted into two peaks. This deconvolution is associated with different positions of Y atoms. The peaks at the binding energies of 158.7 eV (y = 0.1) and 158.5 eV (y = 0.2) can be attributed to Y^{3+} when Y atoms are in the form of Y–O–P. The other peak is shifted to lower energy at binding energies of 157.7 eV (y = 0.1) and 157.8 eV (y = 0.2).

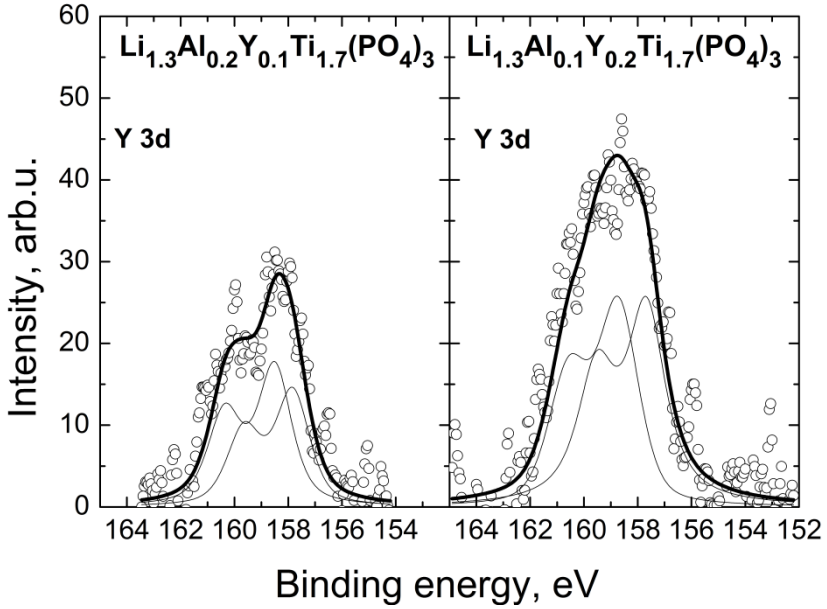

Figure 4.5.12 Y 3d core level XPS for $Li_{1.3}Al_yY_{x-y}Ti_{1.7}(PO_4)_3$ (x = 0.3; y = 0.1, 0.2) ceramics at room temperature.

This shift implies that the Y atoms are either in the other valence state [71] or Y may be bonded to less electronegative elements and form bonds such as in oxides materials. The Y^{2+} valence state is not typical for yttrium. If yttrium is not in a fully oxidized state the binding energies shift to lower values [72]. The peaks with lower binding energies can indicate that in investigated compounds some concentration of oxygen vacancies exists as in $Y_2O_{3-\delta}$ [72]. The other possibility is the formation of oxide in the surface region. Yttrium 3d spectra show bigger amount of Y with lower binding energy peak for compound with y = 0.1. The increase of the component at 157.7 eV together with the simultaneous increase in the O 1s component at 530.1 eV is an indication that low binding energy peak of Y 3d can be related to yttrium oxide. The X-ray diffraction patterns did not show any amount of Y_2O_3 phase but XPS is very sensitive to all changes in the surface region. It has been reported that surface and grain boundary analysis of yttrium doped zirconia ceramics showed yttrium enrichment after heat treatment at (1000–1300)°C temperature [73, 74]. These treatment conditions are suitable for yttrium segregation. The Al 2p spectrum peak of $Li_{1.3}Al_yY_{x-y}Ti_{1.7}(PO_4)_3$ (x = 0.3; y = 0.1, 0.2) ceramics is centred at 74.2 eV and this energy corresponds to Al^{+3} as in [58, 75].

XPS analysis of Nb 3d core level in NASICON-type structure ceramics [A1]. Figure 4.5.13 shows Nb 3d spectra of the investigated ceramics. The spectrum shows spin-orbit doublet of Nb $3d_{5/2}$ and Nb $3d_{3/2}$ as in $LiNbO_3$ [76] or potassium lithium niobate [77] crystals. The deconvolution of the Nb 3d core level XPS can be associated with different amounts of Nb^{5+} and Nb^{4+} [76] or lower Nb^{3+} valence states in the investigated ceramics. The amount of different Nb valence states, binding and splitting energies of Nb $3d_{5/2}$ and Nb $3d_{3/2}$ core level XPS are presented in Table 4.5.7.

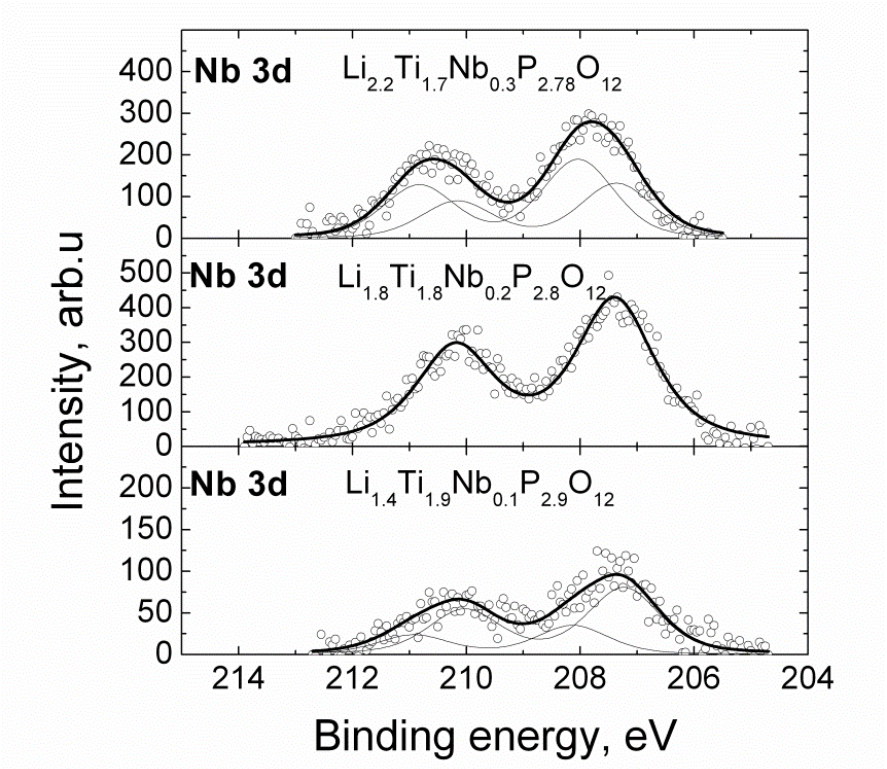

Figure 4.5.13 Nb 3d core level XP spectra of $Li_{1+4x}Ti_{2-x}Nb_yP_{3-y}O_{12}$ (x = 0.1, 0.2, 0.3; y =0, 0.1, 0.2, 0.3).

Table 4.5.7 Summary of X-ray photoelectron spectroscopy results of $Li_{1+4x}Ti_{2-x}Nb_yP_{3-y}O_{12}$ (x = 0.1, 0.2, 0.3; y = 0.1, 0.2, 0.3) ceramics for Nb 3d core level.

Compound	Binding energy, eV	Splitting energy, eV	Amount, at.%	Chi square χ^2
$Li_{1.4}Ti_{1.9}Nb_{0.1}P_{2.9}O_{12}$	207.2	2.8	69.9	0.47
	208.1	2.8	30.1	
$Li_{1.8}Ti_{1.8}Nb_{0.2}P_{2.8}O_{12}$	207.4	2.8	100	1.3
$Li_{2.2}Ti_{1.7}Nb_{0.3}P_{2.7}O_{12}$	207.4	2.8	41.3	1.03
	208.0	2.8	58.7	

Nb 3d and Ta 4f core level XPS were investigated for LTO+Nb and LTO+Ta compounds respectively. The spin-orbit doublet Nb $3d_{3/2}$ core level XPS peak is centered at binding energy 206.0 eV (the spin-orbit splitting energy between $3d_{3/2}$ and $3d_{5/2}$ peaks is 2.8 eV, amount Nb^{5+} valence state is 100 at.%) and these results are well correlated with [78]. The Ta $4f_{7/2}$ core level XPS peak is located at binding energy 24.1 eV. The spin-orbit splitting between $4f_{7/2}$ and $4f_{5/2}$ peaks is 1.8 eV. So the amount of Ta^{5+} is 100 at.%. According to [79], the binding energy of Ta $4f_{7/2}$ core level XPS in Ta_2O_5 was found to be 26.4 eV.

XPS analysis of Fe 2p core level [A4, A5]. The XP spectra of Li 1s of $LiFePO_4$ and $LiFePO_4$/C cannot be separated from the intensive overlapping Fe 3p peak. The Fe $2p_{3/2}$ XPS of both samples are composed of nine peaks with different binding energies (Figure 4.5.14) as in [80]. Binding energies of Fe 2p peaks were in the range from 709.6 to 718.0 eV and in the range from 709.4 to 717.9 eV in $LiFePO_4$ and $LiFePO_4$/C respectively. Grosvenor et. al. assigned Fe $2p_{3/2}$ core level XPS peaks at binding energies 710.2, 711.3, 712.4 and 713.6 eV to Fe^{3+} valence state and peaks at binding energies 708.3, 709.3 and 710.4 eV to Fe^{2+} valence state in Fe_3O_4 [80]. For $LiFePO_4$ ceramics the Fe 2p peaks at binding energies 709.6, 710.4 and 711.3 eV were related to Fe^{2+} oxidation state and for $LiFePO_4$/C composite the Fe 2p peaks at binding

energies 709.4, 710.2 and 711.2 eV were related to Fe^{2+} valence state too. These values are larger than in oxide Fe_3O_4 [80] because the shifting of peaks to higher binding energy is due to formation of bonds Fe-O-P instead of Fe-O-Fe and electronegativity of phosphorus is higher than iron.

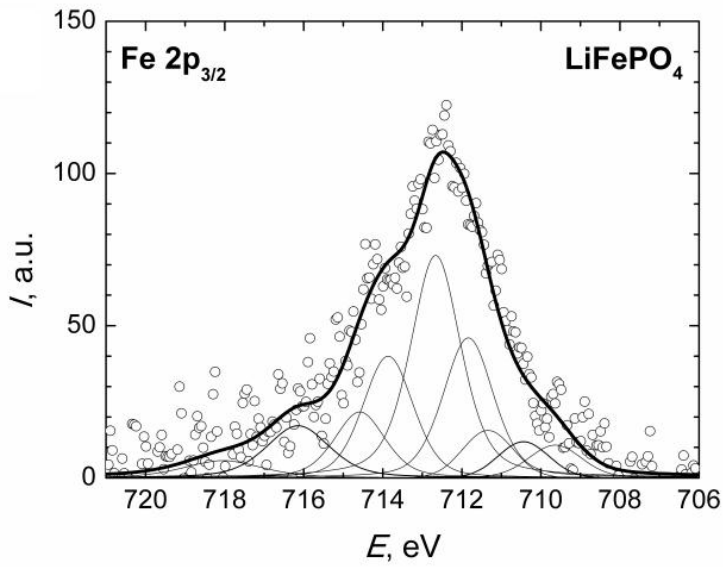

Figure 4.5.14 Fe 2p core level XPS for $LiFePO_4$ ceramic at room temperature.

The amounts of Fe^{2+} valence state in $LiFePO_4$ and $LiFePO_4$/C were found to be 15.8 at.% and 36.0 at.% respectively. The peaks caused by Fe^{2+} valence state are located in binding energy ranges from 709.6 eV to 711.3 eV for $LiFePO_4$ and from 709.4 eV to 711.2 eV for $LiFePO_4$ /C compounds. The results summarized in

Table 4.5.8 show that oxidation Fe^{2+} to Fe^{3+} shift the binding energy region towards to higher energy and correlate with results published in [81]. The Fe 2p peaks related to Fe^{3+} oxidation state for $LiFePO_4$ were found in binding energy range from 711.8 to 714.5 eV and in $LiFePO_4$/C this region was between 711.6 and 714.6 eV. The amounts of Fe^{3+} valence state in $LiFePO_4$ and $LiFePO_4$/C were 84.2 at.% and 64.0 at.% respectively. In the investigated compounds iron should be bivalent. The results of XPS investigations showed that ratio of Fe^{3+} / Fe^{2+} in $LiFePO_4$ and $LiFePO_4$/C were 5.33 and 1.78 respectively. The increase of this ratio in $LiFePO_4$ showed that sintering of the ceramics in air stimulates the reduction Fe^{2+} into Fe^{3+} valence state. Two Fe 2p

satellite peaks are located at binding energies 716.1, 718.0 eV and 716.0, 717.9 eV for $LiFePO_4$ and $LiFePO_4$/C respectively. A broad Fe^{2+} satellite peak was found in the compounds with variable compositions such as $Fe^{II}_{6(1-x)}Fe^{III}_{6x}O_{12}H_{2(7-3x)}CO_3 \cdot 3H_2O$ at binding energy around 715 eV [82].

Table 4.5.8 Summary of Fe 2p core level XPS investigation of $LiFePO_4$ and $LiFePO_4$/C ceramics at room temperature.

Compound	Binding energy, eV	Amount, at.%	Chi square χ^2
$LiFePO_4$	709.6	4.8 (2+)	0.7
	710.4	4.8 (2+)	
	711.3	6.2 (2+)	
	711.8	21.1 (3+)	
	712.6	35.2 (3+)	
	713.8	17.8 (3+)	
	714.5	10.1 (3+)	
	716.1	Satellite	
	718.0	Satellite	
$LiFePO_4$/C	709.4	10.1 (2+)	0.6
	710.2	11.0 (2+)	
	711.2	14.9 (2+)	
	711.6	17.4 (3+)	
	712.7	25.0 (3+)	
	713.8	12.9 (3+)	
	714.6	8.7 (3+)	
	716.0	Satellite	
	717.9	Satellite	

Fe $2p_{3/2}$ XP spectra of $Li_{1-x}Fe_{1-x}Ti_xP_2O_7$ (x= 0, 0.1) ceramics surfaces are shown in Figure 4.5.15. The relative amounts of peaks with different binding

energies of Fe $2p_{3/2}$ core level XP spectra for investigated ceramics are presented in Table 4.5.9 too. As has been mention above, Grosvenor et al. [80] have shown that the Fe $2p_{3/2}$ peak from a range of Fe(II) and Fe(III) high spin compounds can be well fitted using multiplets and $2p_{3/2}$ satellite peaks. For the surfaces of $Li_{1-x}Fe_{1-x}Ti_xP_2O_7$ (x= 0, 0.1) ceramics the Fe $2p_{3/2}$ XP spectrum is composed of nine peaks with different binding energies.

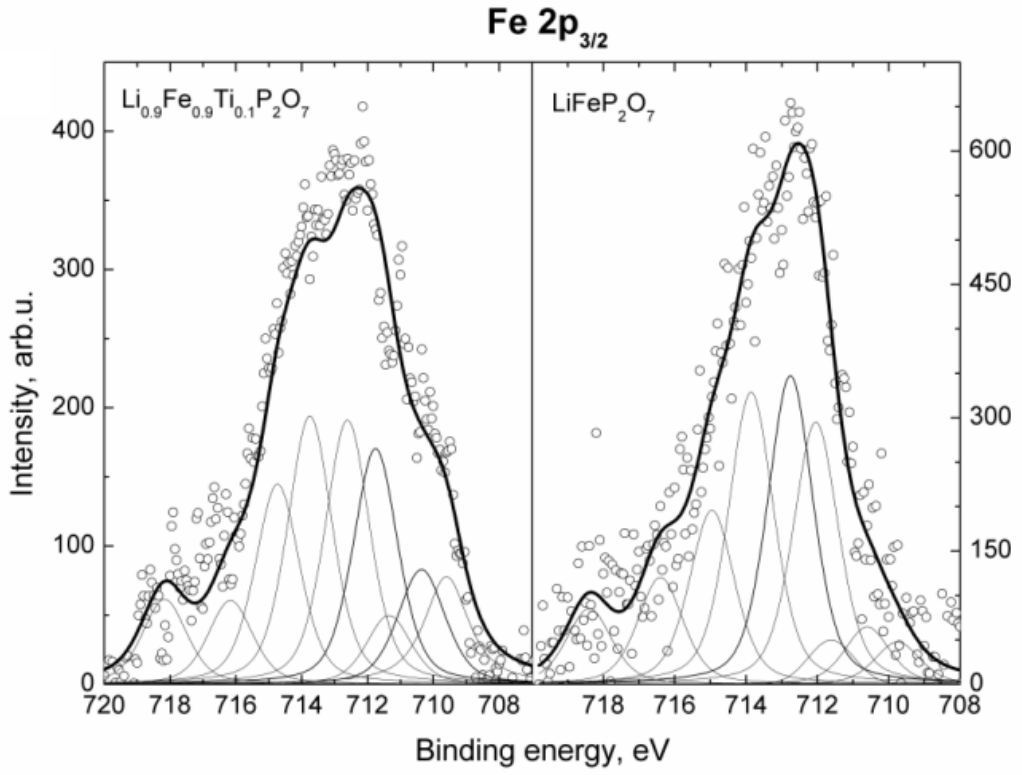

Figure 4.5.15 Fe $2p_{3/2}$ core level XPS for $Li_{1-x}Fe_{1-x}Ti_xP_2O_7$ (x= 0, 0.1) ceramics at room temperature.

For the $LiFeP_2O_7$ compound the multiplet peak with lowest binding energy is located at 710.5 eV and the peak with highest binding energy is at 714.6 eV. For $Li_{0.9}Fe_{0.9}Ti_{0.1}P_2O_7$ the binding energy peaks of Fe $2p_{3/2}$ XP spectrum are in the range from 709.7 eV to 718.0 eV. Considering that in phosphates Fe 2p binding energy will be shifted (1.3-1.5) eV to higher binding energies, the fitting results are in good agreement with Fe $2p_{3/2}$ core level XPS study of Fe_3O_4 compound where both Fe^{2+} and Fe^{3+} species are present [80]. The authors [80] have shown that Fe $2p_{3/2}$ core level XP peaks at binding energies 710.2, 711.3, 712.4 and 713.6 eV are specific with Fe^{3+} valence state and the

peaks at binding energies 708.3, 709.3 and 710.4 eV denote Fe^{2+} locations.

Table 4.5.9 Summary of Fe 2p core level XPS investigation for $Li_{1-x}Fe_{1-x}Ti_xP_2O_7$ (x= 0, 0.1) ceramics at room temperature.

Compound	Binding energy, eV	Amount, at.%	Chi square χ^2
$Li_{0.9}Fe_{0.9}Ti_{0.1}P_2O_7$	709.6	9.7(2+)	0.42
	710.4	9.5(2+)	
	711.3	5.4(2+)	
	711.7	18.4(3+)	
	712.6	20.6(3+)	
	713.8	20.9(3+)	
	714.7	15.6(3+)	
	716.0	Satellite	
	718.0	Satellite	
$LiFeP_2O_7$	709.7	3.6(2+)	0.60
	710.6	4.9(2+)	
	711.4	3.2(2+)	
	712.0	22.3(3+)	
	712.7	26.3(3+)	
	713.8	24.9(3+)	
	715.0	14.8(3+)	
	716.4	Satellite	
	718.4	Satellite	

The broad Fe^{2+} satellite peak was found in the compounds with variable compositions such as $Fe^{II}_{6(1-x)}Fe^{III}_{6x}O_{12}H_{2(7-3x)}CO_3 \cdot 3H_2O$ at the binding energy about 715 eV [82]. The two satellite peaks at binding energies in the range from 716.0 eV to 718.4 eV were found for each of the $LiFeP_2O_7$ and $Li_{0.9}Fe_{0.9}Ti_{0.1}P_2O_7$ compounds. The results of XPS investigations of the $LiFeP_2O_7$ and $Li_{0.9}Fe_{0.9}Ti_{0.1}P_2O_7$ compounds have shown both Fe^{2+} and Fe^{3+}

valence state location in the grains of the ceramics but higher amount of Fe^{2+} have been found in $Li_{0.9}Fe_{0.9}Ti_{0.1}P_2O_7$ compound.

4.6. Peculiarities of electrical properties of NASICON-type compounds [A1, A2, A3]

The impedance spectroscopy investigation of the ionic conductivity in the wide frequency and in the broad temperature ranges allows one to separate charge carrier transport processes in bulk and in grain boundaries of the ceramics. Three dispersion regions are generally observed in σ' spectra of solid electrolyte ceramics when using two-probe method [83, 84].

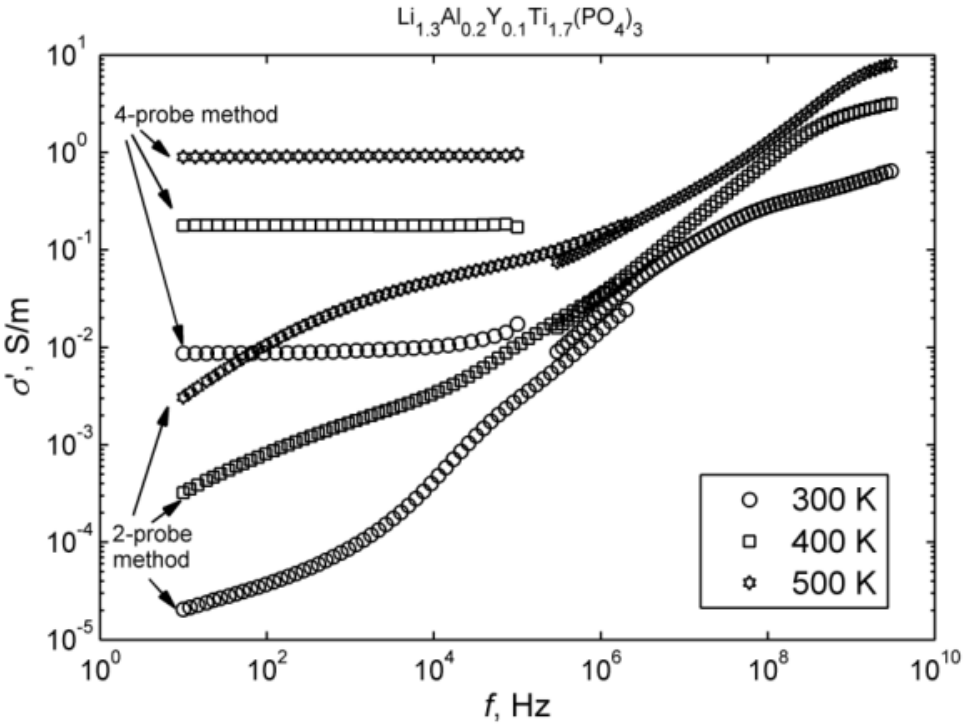

Figure 4.6.1 Characteristic frequency dependences of the real part of complex conductivity of $Li_{1.3}Al_{0.2}Y_{0.1}Ti_{1.7}(PO_4)_3$ ceramics measured by four and two probe methods at different temperatures: 300, 400, 500 K.

The higher frequency part of the recorded spectra may be attributed to the relaxation processes in bulk, the lower frequency part corresponds to relaxation processes in grain boundaries, and the ionic blocking character of the electrode

is observed at even lower frequencies. In Figure 4.6.1 the characteristic frequency dependences of the real part of complex conductivity (σ') of $Li_{1.3}Al_{0.2}Y_{0.1}Ti_{1.7}(PO_4)_3$ ceramics measured by four and two probe method at different temperatures are shown. A clear plateau in microwave frequency region (over 10^8 Hz at 300 K) can be observed, which corresponds to bulk ionic conductivity (σ_b) of the ceramics. Bulk ionic conductivities have been found from complex plain plots of specific resistivity or conductivity. In $\rho''(\rho')$ plot σ_b value corresponds to the diameter of the semicircle as shown in Figure 4.6.2 (a) and in $\sigma''(\sigma')$ plot σ_b value can be found from the interception of a straight line with the real axis (Figure 4.6.2(b)).

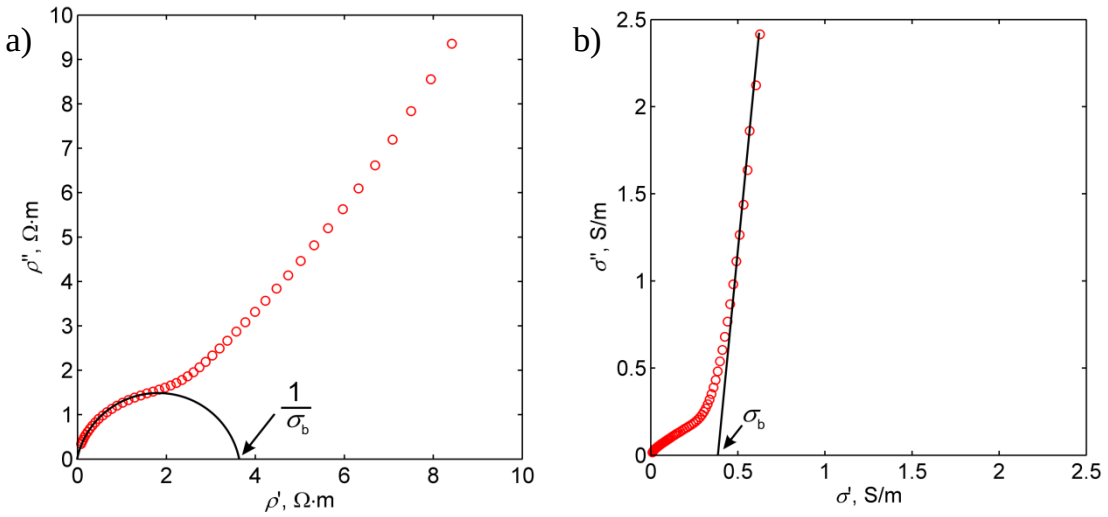

Figure 4.6.2 Complex specific electrical resistivity (a) and conductivity (b) plots of the $Li_{1.3}Al_{0.2}Y_{0.1}Ti_{1.7}(PO_4)_3$ ceramic measured in the microwave electrical fields at temperature 300 K.

Two dispersion regions were found in σ' spectra for both investigated compounds if four-probe method is used. The low frequency dispersion range of σ' is caused by ion transport in grain boundary because microwave frequency range can be attributed to ion transport in bulk of the ceramics. In the impedance spectra obtained by two probe method grain boundary contribution is not visible because of the big influence of the interfaces between Pt electrodes and solid electrolyte. Hence total conductivities ($\sigma_{tot} = 1/(\rho_b + \rho_{gb})$ where ρ_b is bulk resistivity and ρ_{gb} is grain boundary

resistivity of the ceramics) were derived from measurements by four-probe method. In $\rho''(\rho')$ plot the grain boundary semicircle intercepts with the real axis giving σ_{tot} value as shown in Figure 4.6.3.

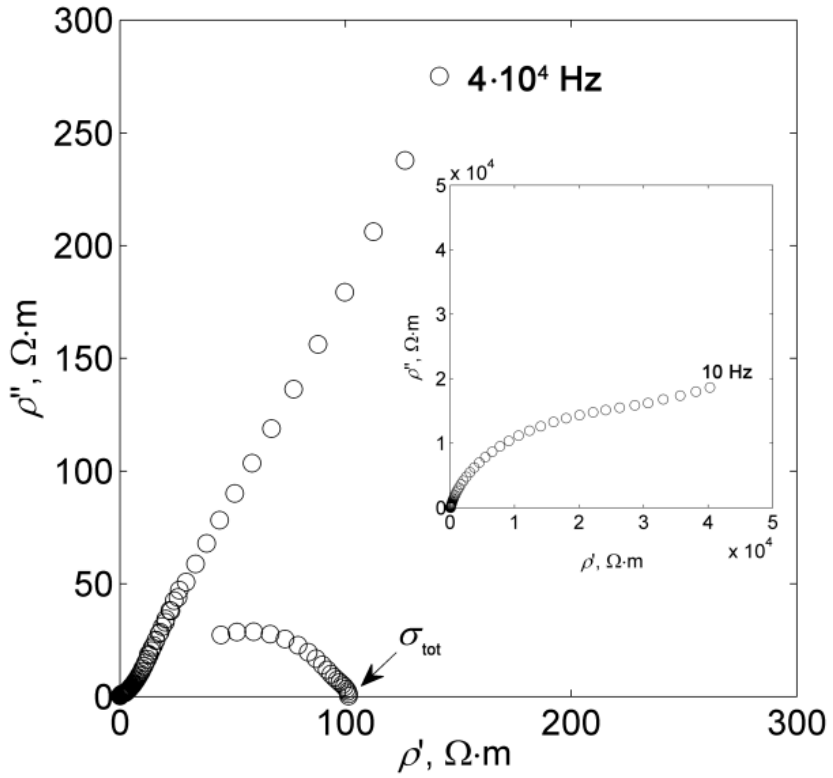

Figure 4.6.3 Determination of total ionic conductivity of $Li_{1.3}Al_{0.2}Y_{0.1}Ti_{1.7}(PO_4)_3$ ceramics from complex specific electrical resistivity plot. Both two-probe and four-probe impedance measurement results are shown. Full scale of the plot is presented in the insert.

The temperature dependences of σ_{tot} and σ_b of $Li_{1.3}Al_yY_{x-y}Ti_{1.7}(PO_4)_3$ (x = 0.3; y = 0.1, 0.2) ceramic samples are shown in Figure 4.6.4 (a), (b). The activation energies of σ_{tot} and σ_b were found from the slopes of the Arrhenius plots. From the maxima of $\rho''(f)$ at different temperatures, the characteristic relaxation frequency (f_b) of the ionic migration process in the grain was determined as described previously in [85, 86]. In Figure 4.6.5 the characteristic frequency dependences of ρ'' at temperature 300 K of $Li_{1.3}Al_{0.2}Y_{0.1}Ti_{1.7}(PO_4)_3$ compound are shown. Figure 4.6.6 shows the temperature dependences of f_b. Table 4.6.1 summarizes the experimental

results of the investigation of σ_{tot}, σ_b, their activation energies $\Delta E_{\sigma tot}$, $\Delta E_{\sigma b}$ and activation energy of characteristic relaxation frequency ΔE_f at 300 K. The results of the investigation of electrical conductivities have shown that increase of stoichiometric parameter y in $Li_{1.3}Al_yY_{x-y}Ti_{1.7}(PO_4)_3$ (x = 0.3; y = 0, 0.1, 0.15, 0.2, 0.3) system leads to the increase of σ_b values.

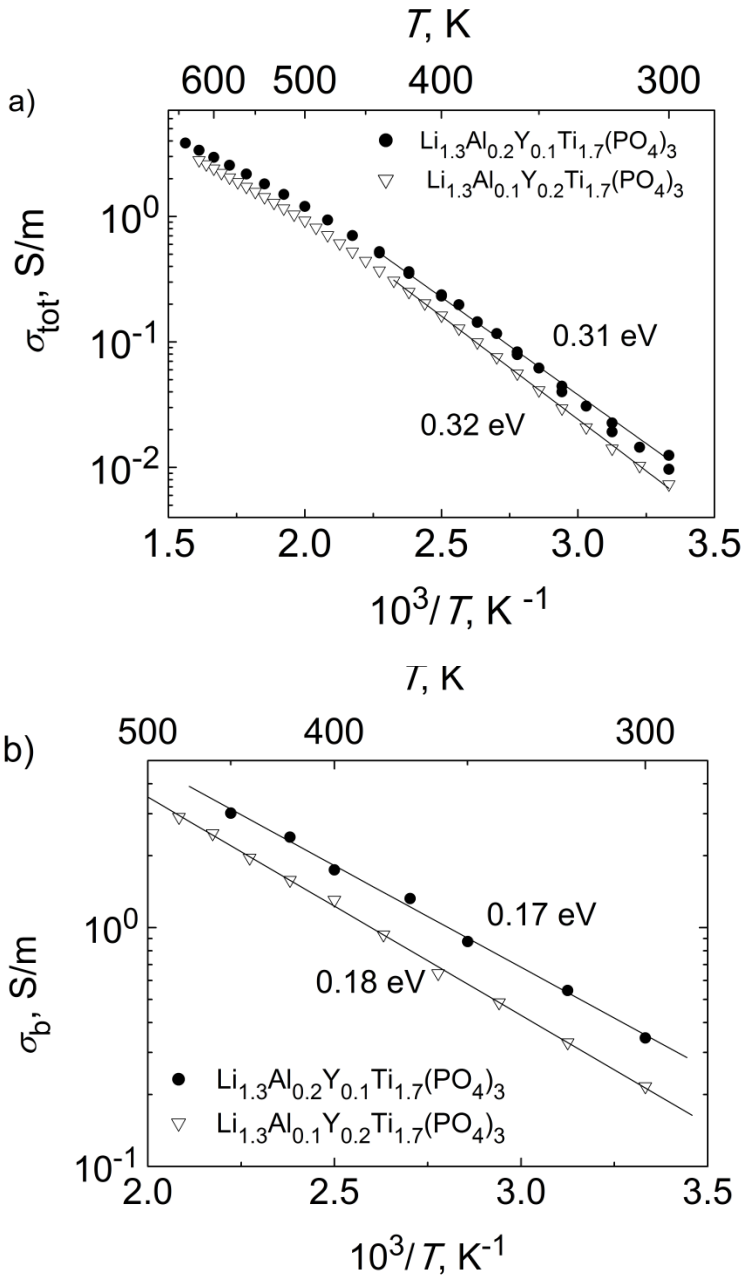

Figure 4.6.4 Temperature dependences of total (a) and bulk (b) conductivities of $Li_{1.3}Al_yY_{x-y}Ti_{1.7}(PO_4)_3$ (x = 0.3; y = 0.1, 0.2) ceramics.

Table 4.6.1 σ_b, σ_{tot}, their activation energies and activation energy of the relaxation frequency in bulk of $Li_{1.3}Al_yY_{x-y}Ti_{1.7}(PO_4)_3$ (x = 0.3; y = = 0, 0.1, 0.15, 0.2, 0.3) ceramic samples at 300 K.

Compound	σ_b, S/m	$\Delta E_{\sigma b}$, eV	ΔE_f, eV	σ_{tot}, S/m	$\Delta E_{\sigma tot}$, eV	Ref.
$Li_{1.3}Al_{0.3}Ti_{1.7}(PO_4)_3$	0.35	0.30	0.30			[57]
$Li_{1.3}Al_{0.2}Y_{0.1}Ti_{1.7}(PO_4)_3$	0.35	0.17	0.18	0.012	0.32	
$Li_{1.3}Al_{0.15}Y_{0.15}Ti_{1.7}(PO_4)_3$	0.22	0.26	0.26	0.0019	0.45	[58]
$Li_{1.3}Al_{0.1}Y_{0.2}Ti_{1.7}(PO_4)_3$	0.22	0.18	0.17	0.0073	0.31	
$Li_{1.3}Y_{0.3}Ti_{1.7}(PO_4)_3$	0.094	0.19	0.19			[57]

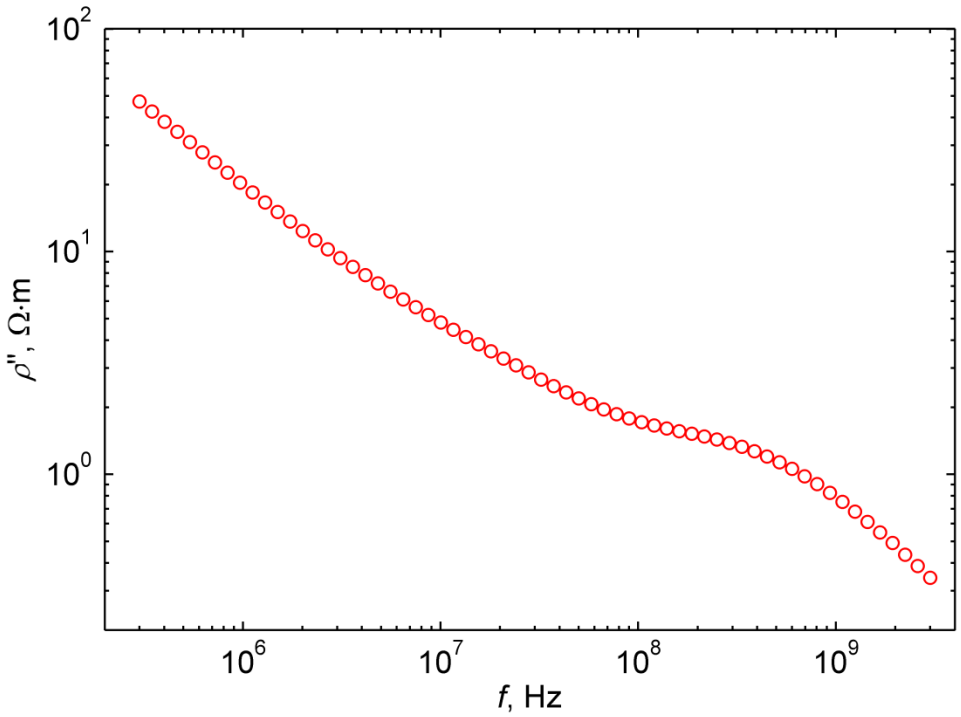

Figure 4.6.5 Characteristic frequency dependences of imaginary part of complex resistivity of $Li_{1.3}Al_{0.2}Y_{0.1}Ti_{1.7}(PO_4)_3$ ceramic at 300 K.

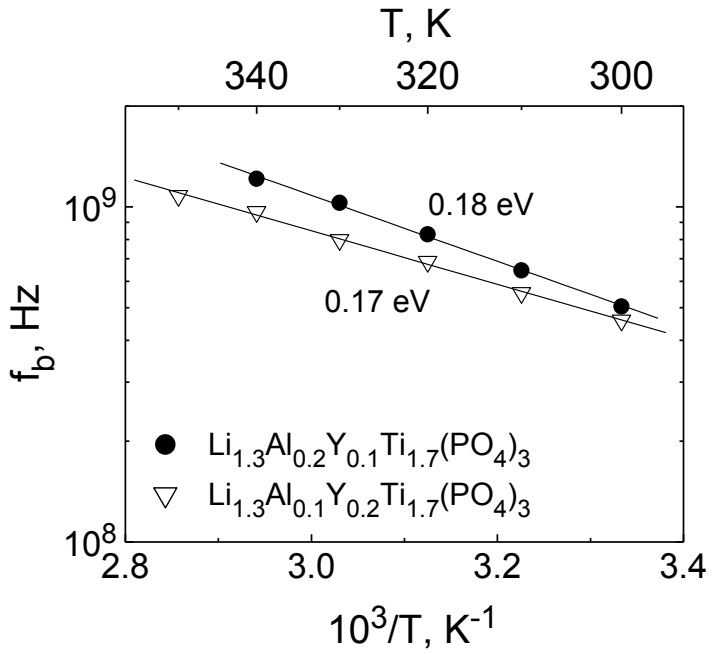

Figure 4.6.6 Temperature dependences of relaxation frequency in the bulk of $Li_{1.3}Al_yY_{x-y}Ti_{1.7}(PO_4)_3$ (x = 0.3; y = 0.1, 0.2) ceramics.

A good agreement between the activation energy of ionic migration process in grains, $\Delta E_{\sigma b}$, and the activation energy of characteristic relaxation frequency, ΔE_f, is found. The activation energy ΔE_f correlates with the activation energy of mobility of charge carriers in grains. As we found that the values of activation energies of the bulk ionic conductivities of investigated ceramics are similar to the activation energies of relaxation frequency, which can be attributed to migration of Li^+ ions, the concentration of charge carriers remains constant with changing temperature. It is shown that the major role in the temperature dependence of bulk conductivity is played by the Li^+ ion mobility which increases as temperature increases.

Electrical properties of $Li_{1+4x}Ti_{2-x}Nb_yP_{3-y}O_{12}$ ceramics were investigated by two probe methods. Two relaxation dispersions have been found in complex conductivity and impedance spectra of the studied $Li_{1+4x}Ti_{2-x}Nb_yP_{3-y}O_{12}$ ceramics. The one in the high frequency region was attributed to Li^+ ion relaxation in the bulk and the intermediate frequency range dispersion was caused by ion blocking effect at grain boundaries of the ceramics. Frequency

dependences of the real part of complex conductivity of $Li_{1+4x}Ti_{2-x}Nb_yP_{3-y}O_{12}$ (x = 0.1, 0.2, 0.3; y =0, 0.1, 0.2, 0.3) ceramics measured at temperature T = 530 K are shown in Figure 4.6.7. The dispersion regions shift to higher frequencies while temperature is increased.

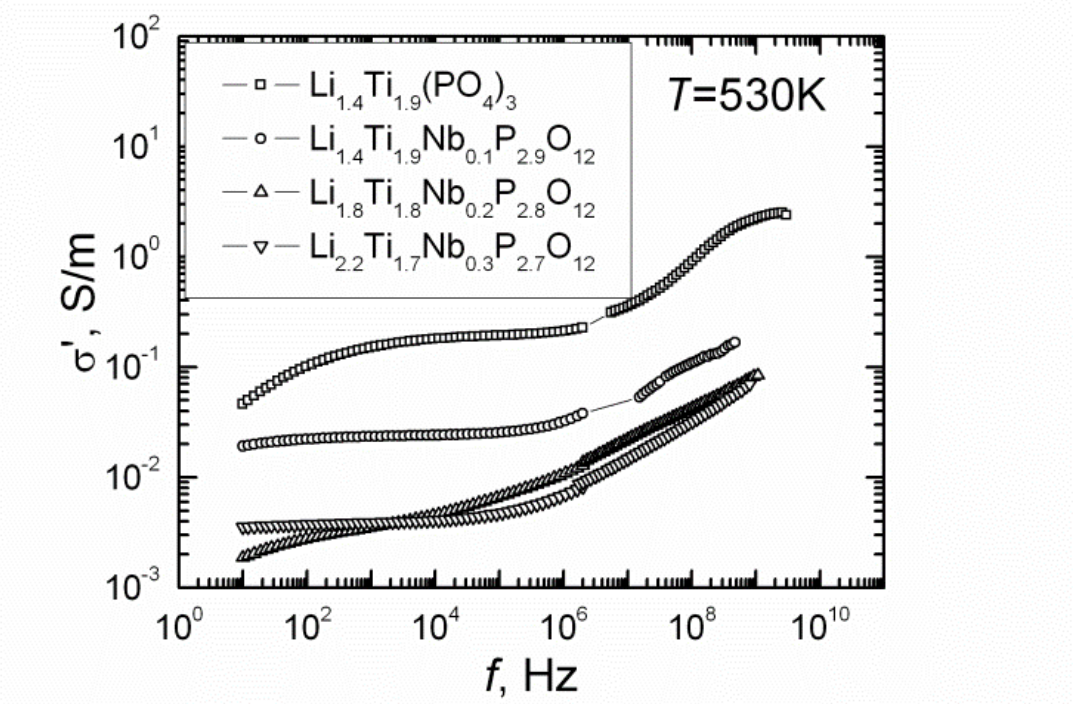

Figure 4.6.7 Frequency dependences of the real part of conductivity of $Li_{1+4x}Ti_{2-x}Nb_yP_{3-y}O_{12}$ (x = 0.1 0.2, 0.3; y =0.1, 0.2, 0.3) ceramics.

Bulk (σ_b) and total (σ_{tot}) conductivities were derived from impedance complex plain $Z''(Z')$ and conductivity complex plain $\sigma''(\sigma')$ plots. The characteristic $Z''(Z')$ and $\sigma''(\sigma')$ plots of $Li_{1.4}Ti_{1.9}P_3O_{12}$ ceramics at temperature T = 530 K are shown in Figure 4.6.8 and Figure 4.6.9 respectively.

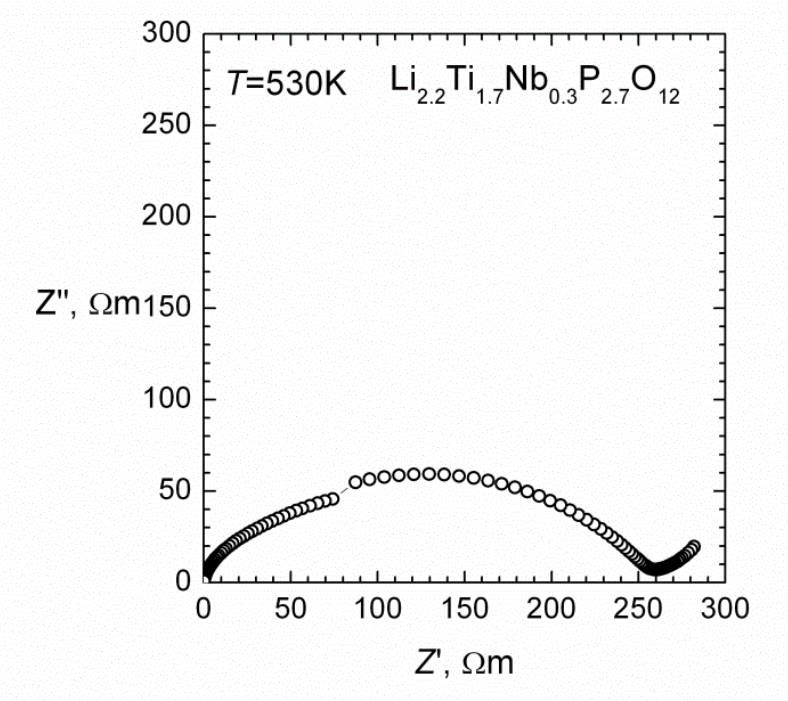

Figure 4.6.8 Characteristic impedance complex plain plot of $Li_{2.2}Ti_{1.7}Nb_{0.3}Ti_{1.7}P_{2.7}O_{12}$ ceramic.

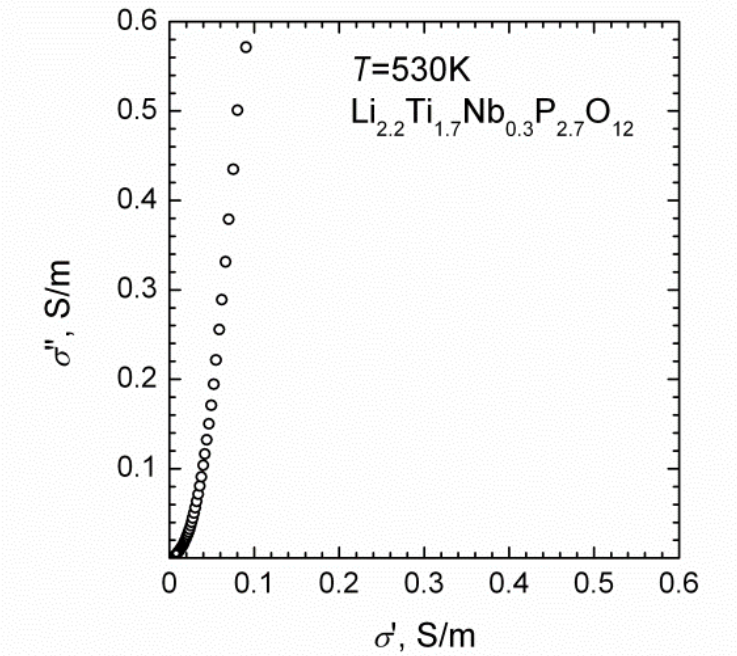

Figure 4.6.9 Characteristic conductivity complex plain plot of $Li_{2.2}Ti_{1.7}Nb_{0.3}Ti_{1.7}P_{2.7}O_{12}$ ceramic.

Temperature dependences of σ_{tot} and σ_b of $Li_{1+4x}Ti_{2-x}Nb_yP_{3-y}O_{12}$ (x = 0.1, 0.2, 0.3; y =0, 0.1, 0.2, 0.3) ceramics are shown in Figure 4.6.10 and Figure 4.6.11 respectively. σ_b and σ_{tot} of investigated ceramics change

according to Arrhenius law in the studied temperature range. The values of σ_b and σ_{tot}, their activation energies (ΔE_b) and (ΔE_{tot}) are summarized in Table 4.6.2. The comparison of the results of the XRD and conductivity investigations has shown that increase of the impurities of $LiTiPO_5$ leads to the decrease of total and bulk conductivities and increase their activation energies. According to [69] the compound of $LiTiPO_5$ exhibit very low electrical conductivity ((5-10)·10^{-4} S/m at 673 K, its activation energy $\Delta E \approx 1$ eV).

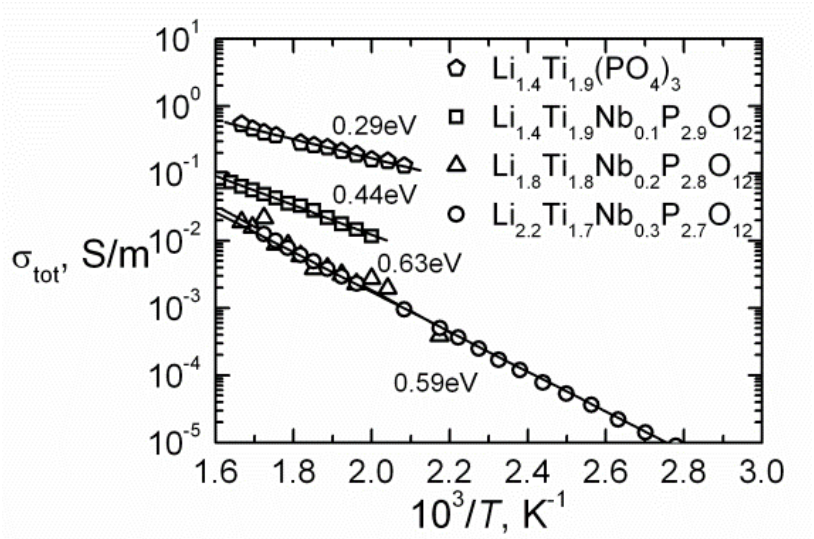

Figure 4.6.10 Temperature dependences of total conductivities of $Li_{1+4x}Ti_{2-x}Nb_yP_{3-y}O_{12}$ ceramics.

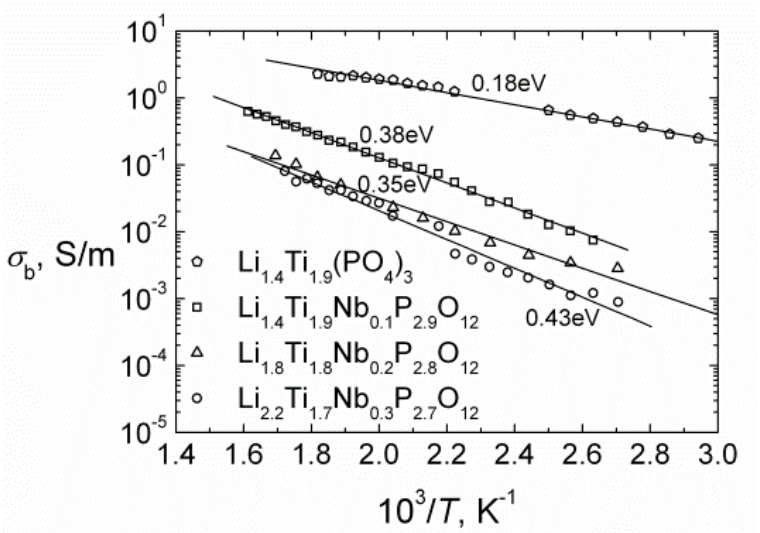

Figure 4.6.11 Temperature dependences of bulk conductivities of $Li_{1+4x}Ti_{2-x}Nb_y P_{3-y}O_{12}$ ceramics.

Table 4.6.2 σ_b, σ_t and their activation energies of $Li_{1+4x}Ti_{2-x}Nb_yP_{3-y}O_{12}$ ceramics at temperature T = 530 K.

Compounds	σ_b, S·m^{-1}	ΔE_b, eV	σ_t, S·m^{-1}	ΔE_t, eV
$Li_{1.4}Ti_{1.9}P_3O_{12}$	2.07	0.18	0.244	0.29
$Li_{1.4}Ti_{1.9}Nb_{0.1}P_{2..9}O_{12}$	0.22	0.38	0.022	0.44
$Li_{1.8}Ti_{1.8}Nb_{0.2}P_{2.8}O_{12}$	0.05	0.4	0.004	0.59
$Li_{2.2}Ti_{1.7}Nb_{0.3}P_{2.7}O_{12}$	0.04	0.43	0.0038	0.59

The temperature dependences of real part of dielectric permittivity (ε') and losses (tanδ) measured at frequency 1 GHz are presented in Figure 4.6.12 and Figure 4.6.13 respectively. At room temperature, the value of ε' of $Li_{1.4}Ti_{1.9}P_3O_{12}$ ceramic was found to be 12 and the values of ε' decrease with increase of stoichiometric parameters x, y and the amount of impurities in the ceramics. The increase of the values of ε' with temperature of the investigated compounds can be caused by contribution of the migration polarization of lithium ions, vibration of the lattice and electronic polarization.

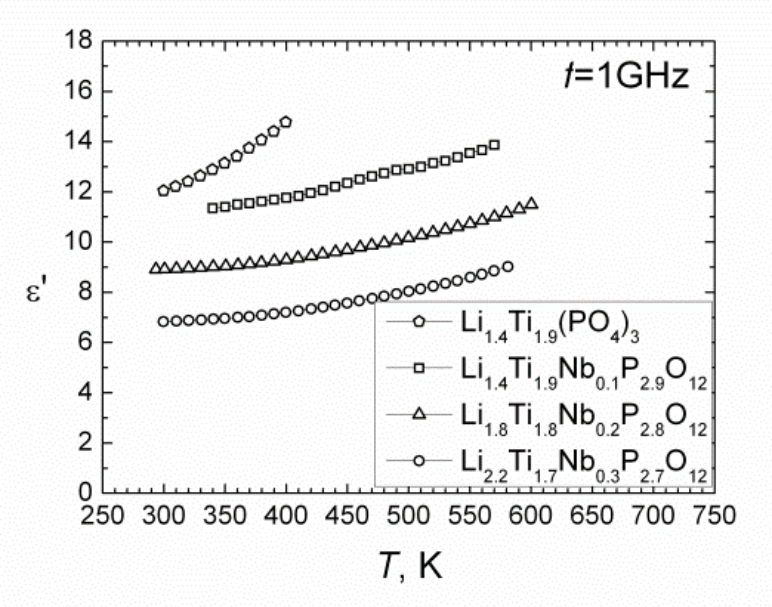

Figure 4.6.12 Temperature dependences of dielectric permittivity of $Li_{1+4x}Ti_{2-x}Nb_yP_{3-y}O_{12}$ ceramics.

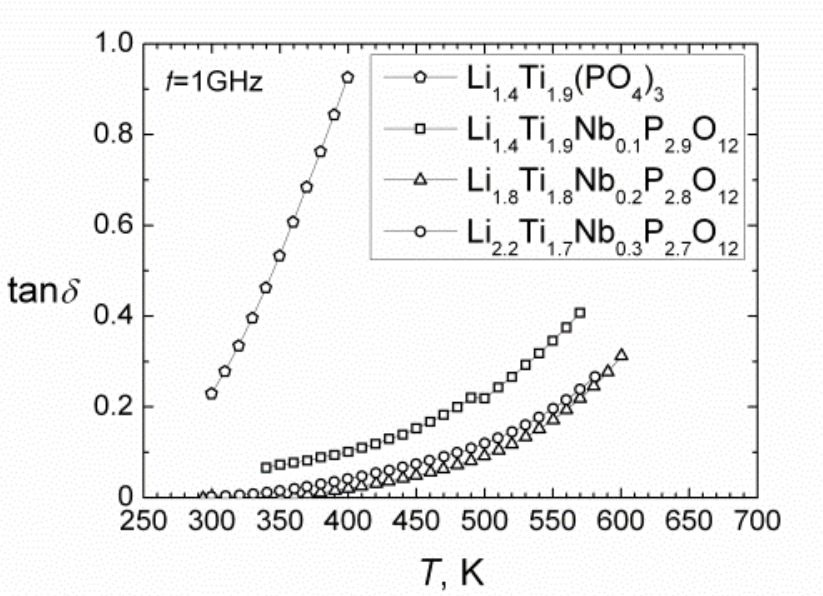

Figure 4.6.13 Temperature dependences of tanδ of $Li_{1+4x}Ti_{2-x}Nb_yP_{3-y}O_{12}$ ceramics.

The characteristic frequency dependences of the real part of complex conductivity (σ') of $Li_{1+4x}Ti_{2-x}(PO_4)_3$ (where x = 0.2, 0.5) ceramics measured at temperature T = 300 K are shown in Figure 4.6.14. In the frequency range from 10 Hz to 100 kHz the ceramics were investigated by four probe method and in the microwave range the measurements were carried out by coaxial technique.

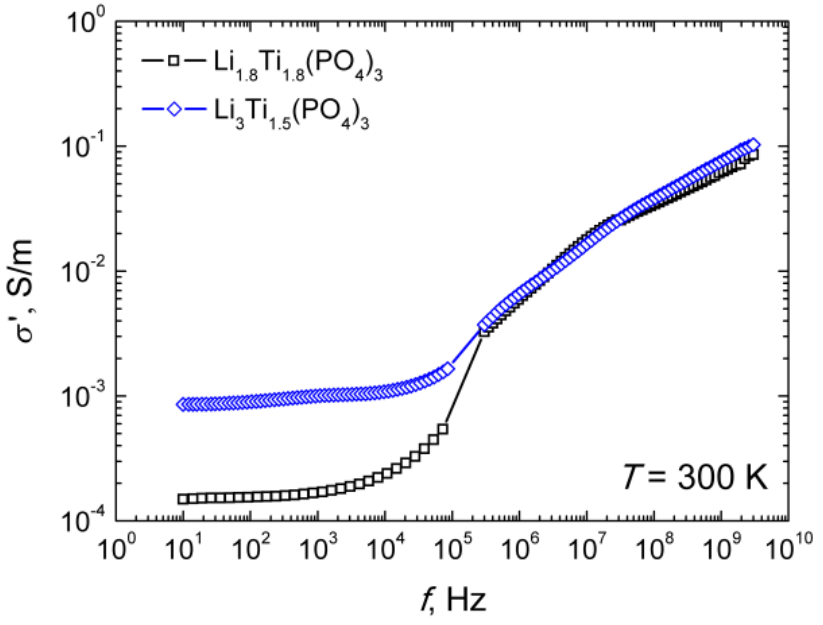

Figure 4.6.14 Frequency dependences of total conductivities of $Li_{1+4x}Ti_{2-x}(PO_4)_3$ (where x = 0.2, 0.5) measured at T = 300 K temperature.

Two dispersion regions in σ' spectra for all investigated compounds were found. The low frequency dispersion range of σ' is caused by ion transport in grain boundary because high frequency range is attributed to ion transport in grains as in [83-85, 87]. The processes are thermally activated and dispersion regions shift towards higher frequencies as temperature increases. This phenomenon is typical for relaxation type dispersions. In Figure 4.6.15 the characteristic frequency dependences of the real part of complex conductivity (σ') of $Li_3Ti_{1.5}(PO_4)_3$ ceramics measured at different temperatures are shown.

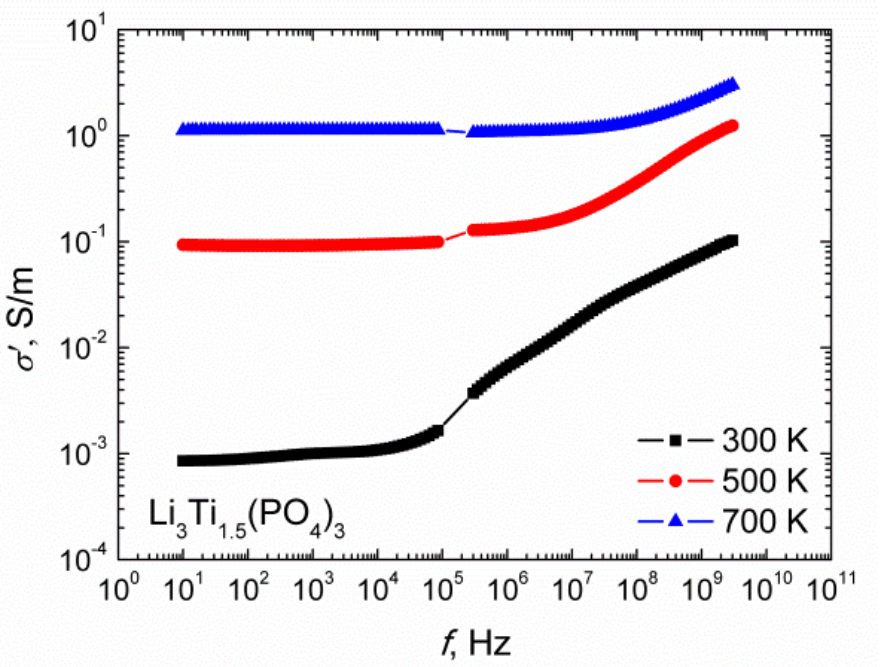

Figure 4.6.15 Characteristic frequency dependences of the real part of complex conductivity of $Li_3Ti_{1.5}(PO_4)_3$ ceramics measured at different temperatures.

The total conductivities (σ_{tot}) of the ceramics were derived from temperature dependences of the plateau of $\sigma'(f)$ dependences and complex specific resistance $\rho''(\rho')$ plots (see Figure 4.6.16 a)). The temperature dependences of bulk ionic conductivities (σ_b) have been found from complex plain plots of conductivity at different temperatures as shown in Figure 4.6.16 b). The temperature dependences of σ_{tot} and σ_b of $Li_{1+4x}Ti_{2-x}(PO_4)_3$ (where x = 0.2, 0.5) ceramic samples are shown in Figure 4.6.17. The maximal value of σ_{tot} was found for compound with parameter x = 0.5. The increase of the

parameter x leads to the increase of the value of σ_b. The activation energies of σ_{tot} and σ_b were found from the slopes of the Arrhenius plots.

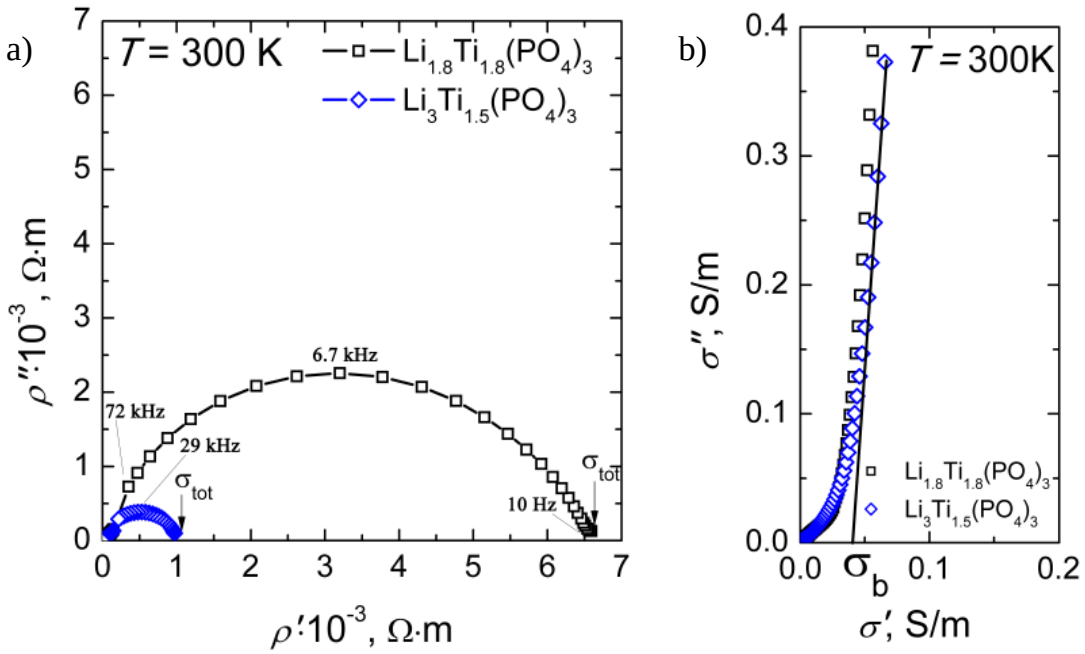

Figure 4.6.16 a) Complex specific electrical resistivity and b) complex specific electrical conductivity plots of $Li_{1+4x}Ti_{2-x}(PO_4)_3$ (where x = 0.2, 0.5) ceramics at temperature T = 300 K.

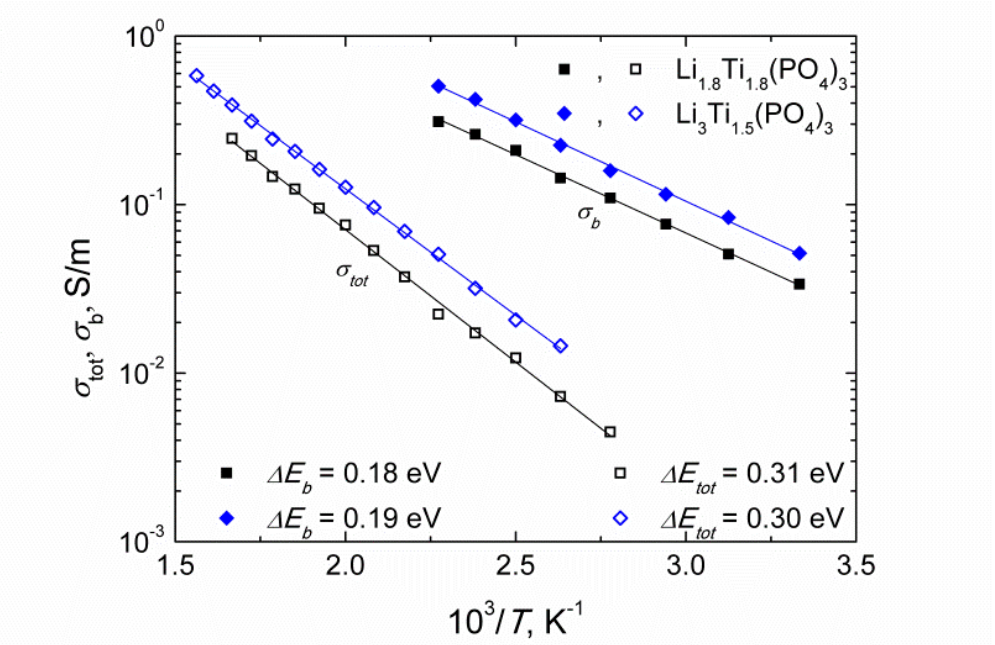

Figure 4.6.17 Arrhenius plots of total and bulk conductivities of $Li_{1+4x}Ti_{2-x}(PO_4)_3$ (where x = 0.2, 0.5) ceramics.

From the maxima of $\rho''(f)$ at different temperatures, the characteristic relaxation frequency (f_b) in the grain was determined as in [86, 88]. In Figure 4.6.18 the characteristic frequency dependences of ρ'' at temperature 300 K of $Li_{1+4x}Ti_{2-x}(PO_4)_3$ (where x = 0.2, 0.5) compounds are shown.

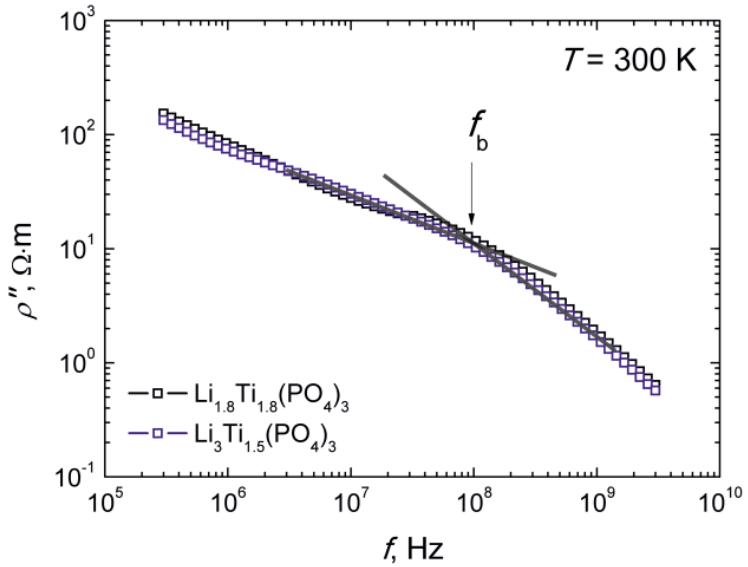

Figure 4.6.18 Frequency dependences of the imaginary part of complex resistivity of $Li_{1+4x}Ti_{2-x}(PO_4)_3$ (where x = 0.2, 0.5) ceramics at temperature T = 300 K.

The relaxation frequency is thermally activated and increase with temperature according to Arrhenius law: $f_b = f_0\exp(-\Delta E_f/kT)$, where f_0 is an attempt frequency related to the lattice vibrations, ΔE_f – activation energy of f_b, k – Boltzmann constant. The activation energies (ΔE_f) were calculated from the slopes of the Arrhenius plots of f_b. Figure 4.6.19 shows the temperature dependences of f_b. Table 4.6.3 summarizes our experimental results of the investigation of σ_{tot}, σ_b, their activation energies and f_b and activation energy of characteristic relaxation frequency ΔE_f. The values of the activation energy of ionic conductivity in grains ΔE_b, and the activation energy of characteristic relaxation frequency ΔE_f are similar. The activation energy ΔE_f associates with the activation energy of mobility of charge carriers in grains. As we found that the values of activation energies of the bulk ionic conductivities of investigated ceramics are similar to the activation energies of relaxation frequency, which

can be attributed to mobility of Li^+ ions, the concentration of charge carriers remains constant with changing temperature.

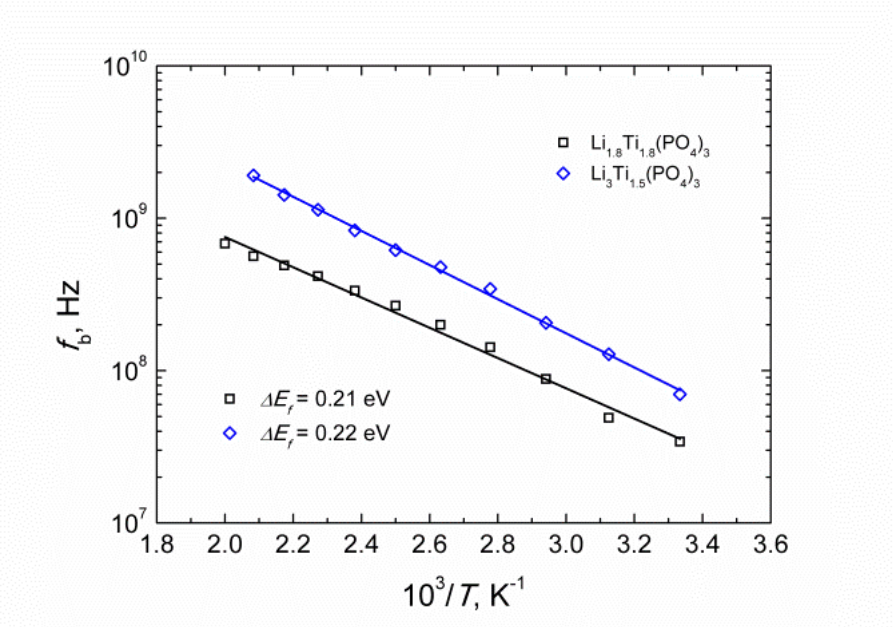

Figure 4.6.19 Temperature dependences of relaxation frequency in the bulk of $Li_{1+4x}Ti_{2-x}(PO_4)_3$ (where x = 0.2, 0.5) ceramics.

The temperature dependences of the dielectric permittivity (ε') were investigated at the frequency of 1 GHz. The values of ε' at temperature 300 K of $Li_{1+4x}Ti_{2-x}(PO_4)_3$ ceramics where x = 0.2 and 0.5 found to be 9.69 and 10.82 respectively. These ε' values at room temperature are characteristic for NASICON – type compounds [83, 89]. For example the values of dielectric permittivity of Li^+ conducting NASICON – type compounds $Li_{1+x}Y_yTi_{2-y}(PO_4)_3$ (where x, y = 0.3; 0.4) were found to be ε' = 10 and increase with temperature [83]. This frequency at temperature T = 400 K is higher than Maxwell relaxation frequency $f_M = \sigma_b / 2\pi\varepsilon'\varepsilon_0$ (where $\varepsilon_0 = 8.85 \times 10^{-12}$ F/m is dielectric constant of the vacuum).

Table 4.6.3 σ_b (T = 300 K), σ_{tot} (T = 380 K), f_b (T = 300 K) and their activation energies of $Li_{1+4x}Ti_{2-x}(PO_4)_3$ (where x = 0.2, 0.5) samples.

Compound	σ_b, S/m (300 K)	$\Delta E_{\sigma b}$, eV	σ_{tot}, S/m (380 K)	$\Delta E_{\sigma tot}$, eV	f_b, MHz (300 K)	ΔE_f, eV	ε′ (300 K)
$Li_{1.8}Ti_{1.8}(PO_4)_3$	0.0338	0.18	0.0073	0.31	34	0.21	9.69
$Li_3Ti_{1.5}(PO_4)_3$	0.0515	0.19	0.0146	0.30	70	0.22	10.82

The frequency dependences of ε' for $Li_{1+4x}Ti_{2-x}(PO_4)_3$ (where x = 0.2, 0.5) ceramics at temperatures 300 K and 400 K are shown in Figure 4.6.20. The results of the measurements of dependences $\varepsilon'(f)$ showed that the frequency of 1 GHz is higher than the frequency dispersion regions for both compounds. The calculated Maxwell relaxation frequency at temperature T = 400 K for compounds with x = 0.2 and 0.5 were found to be 332 MHz and 426 MHz respectively.

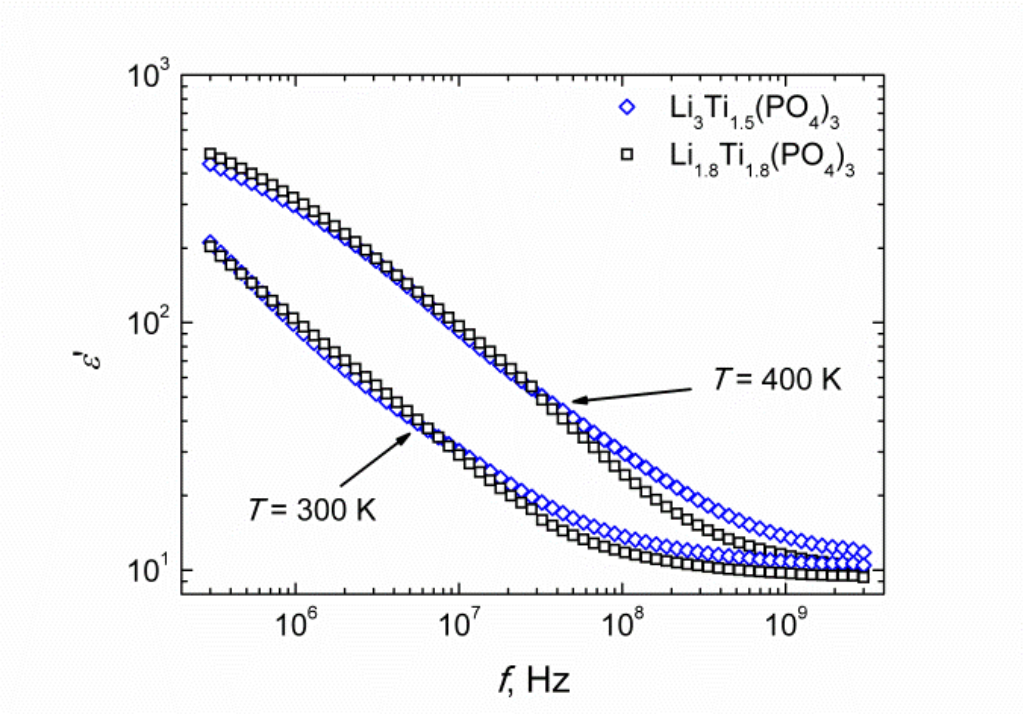

Figure 4.6.20 The frequency dependences of $\varepsilon'(f)$ for $Li_{1+4x}Ti_{2-x}(PO_4)_3$ (where x = 0.2, 0.5) ceramics at temperatures 300 K and 400 K.

The temperature dependences of ε' of $Li_{1+4x}Ti_{2-x}(PO_4)_3$ (where x = 0.2, 0.5) ceramics are shown in Figure 4.6.21. The values ε' at temperature 300 K of the $Li_{1+4x}Ti_{2-x}(PO_4)_3$ (where x = 0.2, 0.5) ceramics are summarized in Table 4.6.3 too. The increase of the values of ε' with temperature of the investigated compounds can be caused by contribution of the migration polarization of lithium ions, vibration of the lattice and electronic polarization.

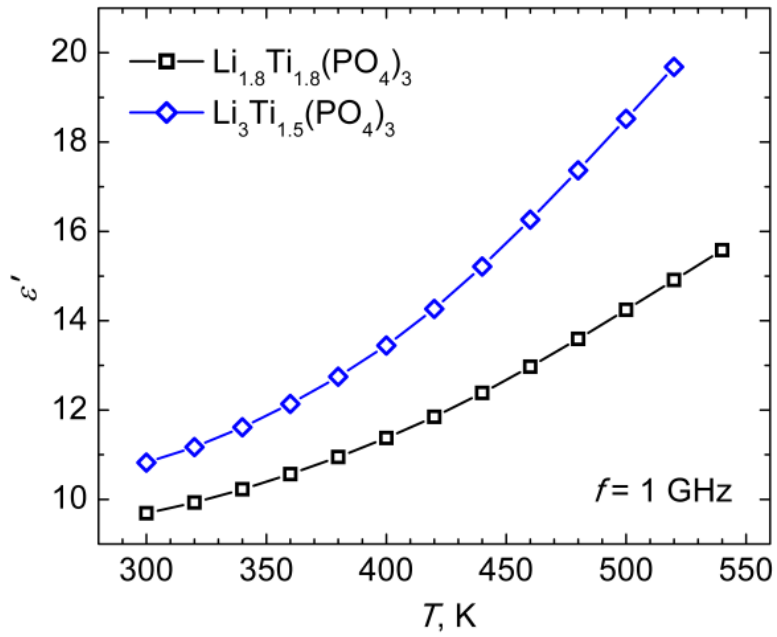

Figure 4.6.21 Temperature dependences of the real part of complex dielectric permittivity measured at 1 GHz frequency.

4.7. **Anomalies of electrical properties of $LiFeP_2O_7$ and $Li_{0.9}Fe_{0.9}Ti_{0.1}P_2O_7$ pyrophosphate ceramics [A5]**

The characteristic frequency dependences of the real part of complex conductivity (σ') of the $LiFeP_2O_7$ and $Li_{0.9}Fe_{0.9}Ti_{0.1}P_2O_7$ ceramics measured at temperatures 560 K and 660 K are shown in Figure 4.7.1. The dispersion regions in σ' spectra for both investigated ceramics were found. The processes are thermally activated and dispersion regions shift towards higher frequencies as temperature increases. This phenomenon is typical for relaxation type dispersions which are general in the solid electrolyte ceramics [83, 84, 87]. It wasn't possible to distinguish grain boundary and bulk conductivities of the ceramics in the measured temperature and frequency ranges as they were separated in the previous works [90, 91].

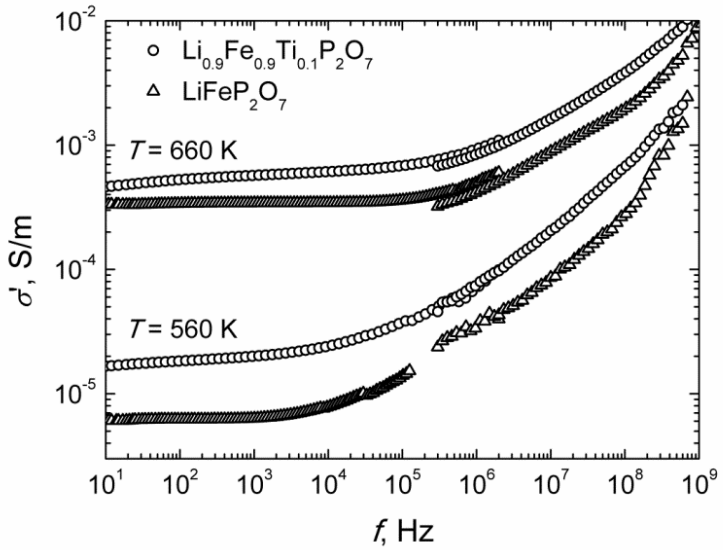

Figure 4.7.1 The frequency dependence of the real part of complex electrical conductivity at 560 K and 660 K temperature for investigated ceramics.

The total conductivities (σ_{tot}) of the ceramics were derived from frequency dependences of the σ' at different temperatures (see Figure 4.7.1) and complex specific resistance $\rho''(\rho')$ plots (Figure 4.7.2) where semicircle intercepts with the real axis ρ'.The temperature dependences of σ_{tot} of $LiFeP_2O_7$ and $Li_{0.9}Fe_{0.9}Ti_{0.1}P_2O_7$ ceramic samples are shown in Figure 4.7.3. The activation energies (ΔE) of σ_{tot} were found from the slopes of the Arrhenius plots. The partial changes of Fe^{3+} by Ti^{4+} in the compounds lead the increase of the value of σ_{tot} and decrease their activation energy of the investigated ceramics. The activation energy of σ_{tot} for $LiFeP_2O_7$ and $Li_{0.9}Fe_{0.9}Ti_{0.1}P_2O_7$ ceramics was found to be 1.11 eV and 0.94 eV respectively. At temperature T = 550 K for $LiFeP_2O_7$ and at T = 528 K for $Li_{0.9}Fe_{0.9}Ti_{0.1}P_2O_7$ compounds the change of activation energy of σ_{tot} was found. The values of ΔE of σ_{tot} above 550 K for $LiFeP_2O_7$ and above 528 K for $Li_{0.9}Fe_{0.9}Ti_{0.1}P_2O_7$ were found to be 1.25 eV and 1.06 eV respectively. The changes of activation energy of σ_{tot} of the investigated compounds are related to structure phase transitions detected by XRD measurements. The experimental results of the investigation of σ_{tot}, their activation energies and temperatures of the changes of ΔE are summarized in Table 4.7.1.

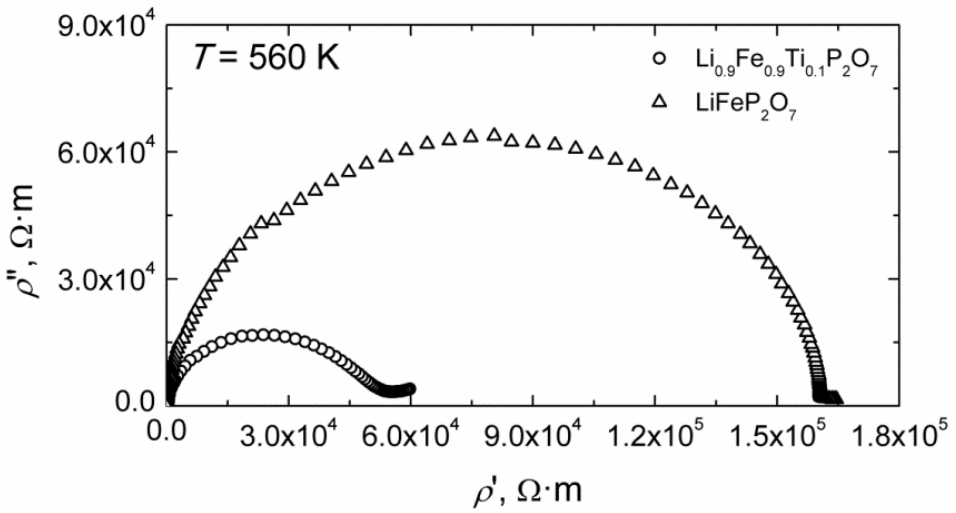

Figure 4.7.2 Complex plots of electrical impedance at 560 K temperature for $Li_{0.9}Fe_{0.9}Ti_{0.1}P_2O_7$ and $LiFeP_2O_7$ ceramics.

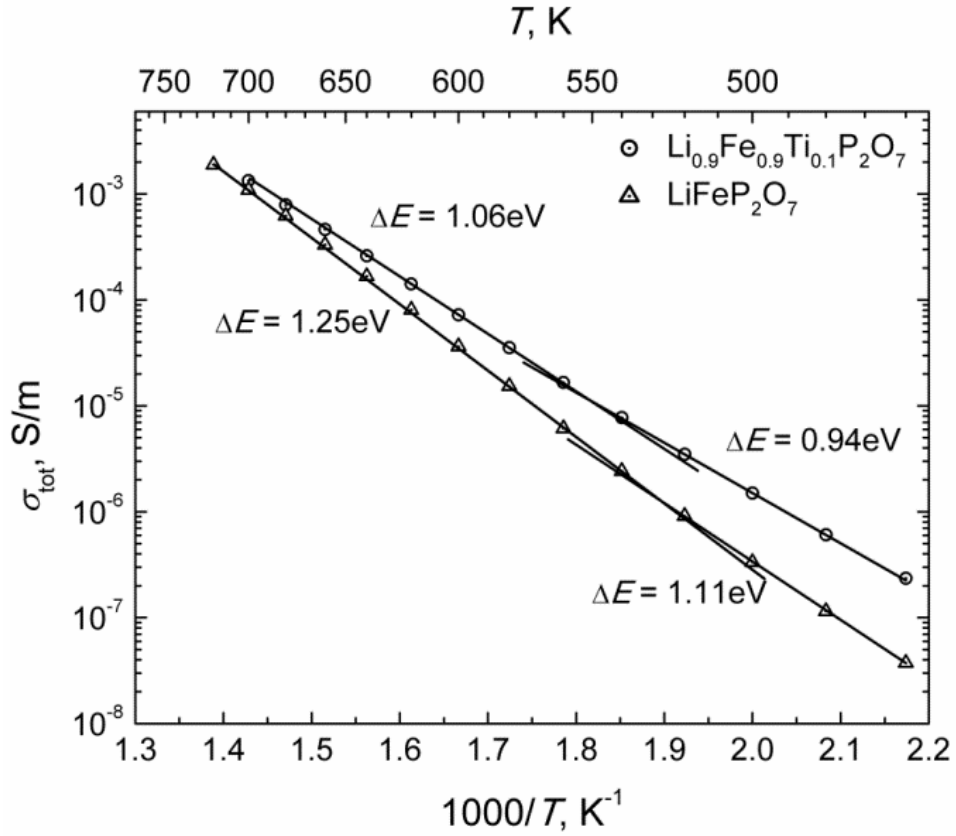

Figure 4.7.3 Total conductivity of $Li_{0.9}Fe_{0.9}Ti_{0.1}P_2O_7$ and $LiFeP_2O_7$ compound ceramics dependences on reciprocal temperature.

Table 4.7.1 Summary of electrical properties: total conductivity (σ_{tot}), activation energy (ΔE_a), Maxwell relaxation frequency (f_M), dielectric permittivity (ε'), tangent loss (tanδ) investigation at different temperatures (T).

Compound	T, K	σ_{tot}, S/m	ΔE_a, eV	f_M, MHz	ε'	tanδ
$Li_{0.9}Fe_{0.9}Ti_{0.1}P_2O_7$	460-550	$1.5 \cdot 10^{-6}$ (500 K)	0.94		6.63 (500 K)	0.0075 (500 K)
	550-700	$1.34 \cdot 10^{-3}$ (700 K)	1.06	3.28 (700 K)	7.35 (700 K)	0.049 (700 K)
$LiFeP_2O_7$	460-528	$3.33 \cdot 10^{-7}$ (500 K)	1.11		6.74 (500 K)	0.0074 (500 K)
	528-720	$1.09 \cdot 10^{-3}$ (700 K)	1.25	2.62 (700 K)	7.48 (700 K)	0.031 (700 K)

The temperature dependences of the dielectric permittivity (ε') and tangent losses (tanδ) of the $LiFeP_2O_7$ and $Li_{0.9}Fe_{0.9}Ti_{0.1}P_2O_7$ ceramic samples were investigated at the frequency of 1 GHz. This frequency at temperature T = 700 K is higher than Maxwell relaxation frequency $f_M = \sigma_b / 2\pi\varepsilon'\varepsilon_0$ (where $\varepsilon_0 = 8.85 \times 10^{-12}$ F/m is dielectric constant of the vacuum). The Maxwell relaxation frequency (f_M) at temperature T = 700 K for $LiFeP_2O_7$ and $Li_{0.9}Fe_{0.9}Ti_{0.1}P_2O_7$ compounds was found to be 2.62 MHz and 3.28 MHz respectively.

The temperature dependences of ε' of $LiFeP_2O_7$ and $Li_{0.9}Fe_{0.9}Ti_{0.1}P_2O_7$ ceramics are shown in Figure 4.7.4. The values ε' and tanδ below and above the temperatures 550 K and 528 K of the $LiFeP_2O_7$ and $Li_{0.9}Fe_{0.9}Ti_{0.1}P_2O_7$ ceramics are summarized in Table 4.7.1 too. The increase of the values of ε' with temperature of the investigated compounds can be caused by contribution of the migration polarization of lithium ions, vibration of the lattice and electronic polarization as in $Li_3Fe_2(PO_4)_3$ [92] and $Li_{3x}La_{2/3-x}TiO_3$ solid electrolytes crystals [93]. The increase of the values of tanδ with increase of the temperature can be related to the contribution of σ_{tot}.

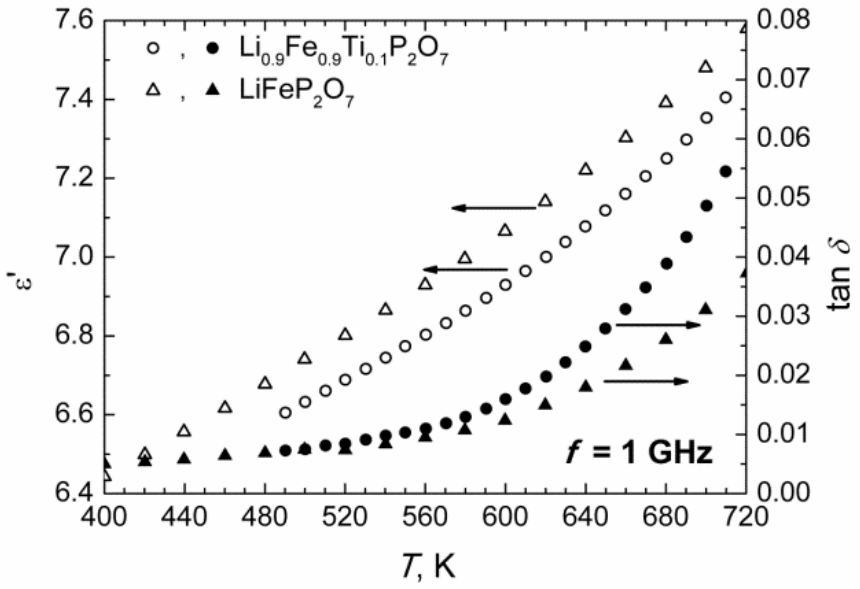

Figure 4.7.4 The temperature dependences of dielectric permittivity and tangent loss in investigated compounds at f = 1 GHz frequency.

4.8. Influence of stoichiometry on the electrical properties of $Li_{4x}Ti_{1-x}P_2O_7$ pyrophosphate ceramics [A6].

The frequency dependences of the real part of complex conductivity of $Li_{4x}Ti_{1-x}P_2O_7$ with x = 0 and x = 0.06 samples are shown in Figure 4.8.1 (a) and (b), respectively. Wide plateau region of σ' is observed in the investigated frequency range. The electrode blocking effects appear in low frequencies only at elevated temperatures. One dispersion region in conductivity spectra of $Li_{4x}Ti_{1-x}P_2O_7$ (x = 0, 0.06, 0.1, 0.2) ceramics was found. The dispersion process in the investigated compounds is thermally activated and dispersion region shifts towards higher frequencies as temperature increases. This phenomenon is typical for relaxation type dispersions.

The temperature dependences of total conductivities (σ_{tot}) of the ceramics were derived from complex impedance plots $\rho''(\rho')$ (see Figure 4.8.2) obtained at different temperatures. The total conductivity (σ_{tot}) values were calculated from the formula $\sigma_{tot} = 1/\rho_{tot}$, where ρ_{tot} is the ρ' value at the point where the semicircular arc intercepts x-axis. The temperature dependences of σ_{tot} are presented in Figure 4.8.3. The activation energies (ΔE_{tot}) of σ_{tot} were calculated according to Arrhenius law. The anomalies of activation energies of σ_{tot} of $Li_{4x}Ti_{1-x}P_2O_7$ (x = 0.06, 0.1, 0.2) compounds in the temperature range from 520 to 580 K were found. The changes of ΔE_{tot} can be related to some disordering in the supercell associated with phase transitions previously reported in [35]. The results of the investigation of σ_{tot} are summarized in Table 4.8.1. The values of total conductivity are higher for samples with lithium ($Li_{4x}Ti_{1-x}P_2O_7$, x = 0.06, 0.1, 0.2) than for host TiP_2O_7 compound (see Table 4.8.1). Also, σ_{tot} values increase with increasing amount of lithium in the samples. The increase of the values of total conductivity in $Li_{4x}Ti_{1-x}P_2O_7$ (x = 0.06, 0.1, 0.2) compared with TiP_2O_7 can be caused by lithium ion transport contribution to σ_{tot}. The total proton conductivity of TiP_2O_7 compound increase with temperature according to Arrhenius law with activation energy ΔE_{tot} = 0.73 eV.

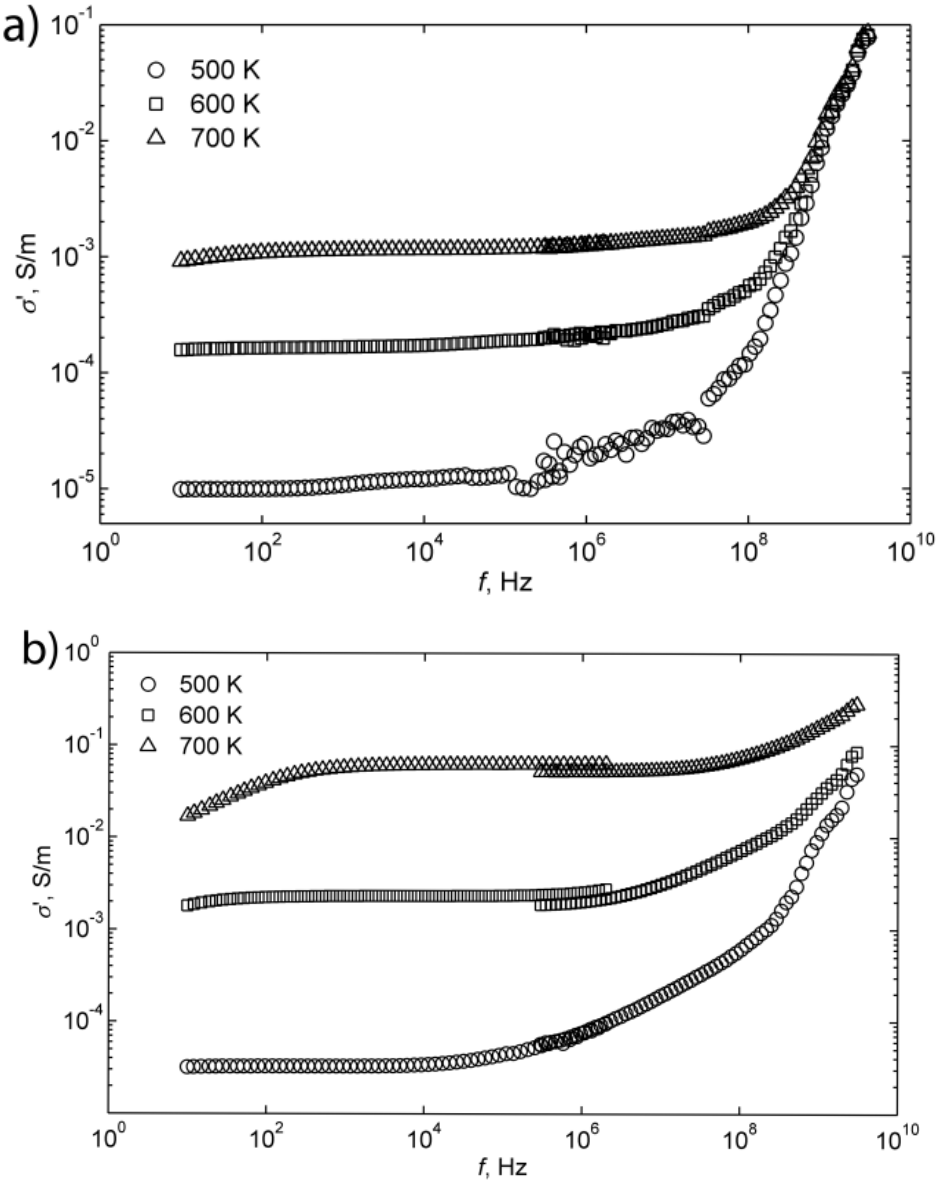

Figure 4.8.1 Frequency dependences of the real part of complex conductivity of TiP_2O_7 (a) and $Li_{0.24}Ti_{0.94}P_2O_7$ (b) ceramics at various temperatures.

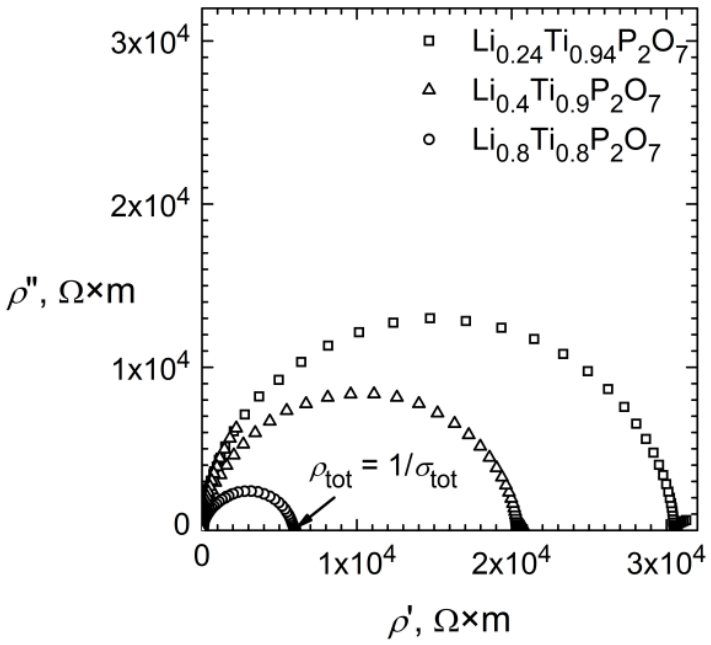

Figure 4.8.2 Complex resistivity plots of $Li_{4x}Ti_{1-x}P_2O_7$ (x = 0.06, 0.1, 0.2) ceramics measured at 500 K.

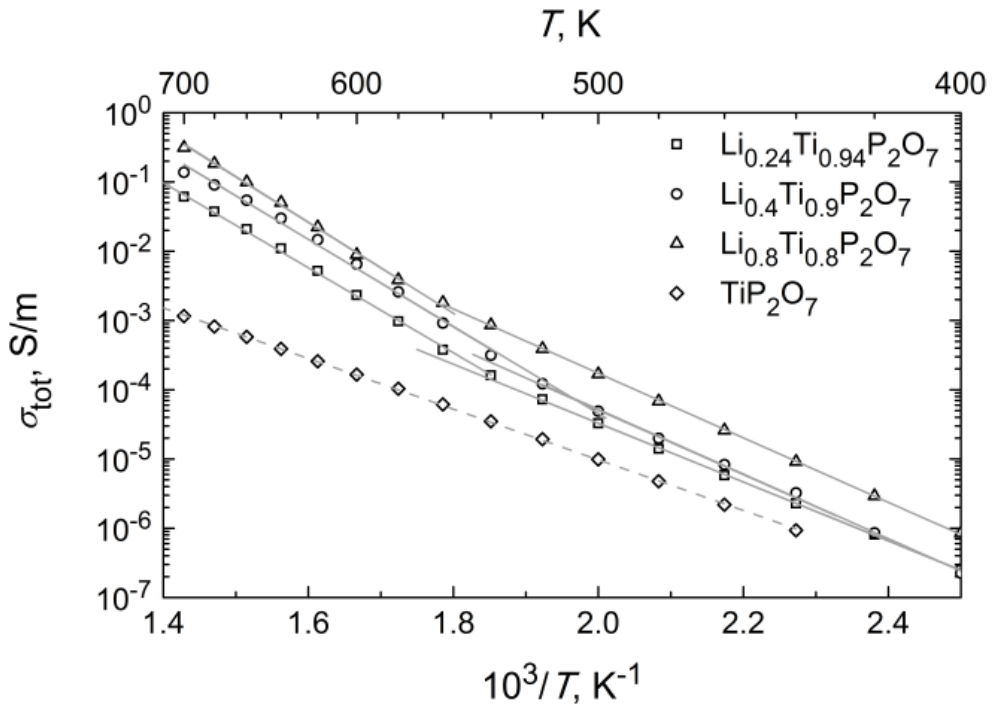

Figure 4.8.3 Temperature dependences of total conductivity of $Li_{4x}Ti_{1-x}P_2O_7$ (x = 0, 0.06, 0.1, 0.2) ceramics.

Table 4.8.1 Total conductivities and their activation energies of $Li_{4x}Ti_{1-x}P_2O_7$ (where x = 0, 0.06, 0.1, 0.2) ceramics.

x in $Li_{4x}Ti_{1-x}P_2O_7$	Total conductivity σ_{tot}, S/m (440 K)	Activation energy ΔE_{tot}, eV	Total conductivity σ_{tot}, S/m (600 K)	Activation energy ΔE_{tot}, eV
0	$9.34 \cdot 10^{-7}$	0.73 (440-720 K)	$1.66 \cdot 10^{-4}$	
0.06	$2.29 \cdot 10^{-6}$	0.85 (400-530 K)	$2.33 \cdot 10^{-3}$	1.23 (530-720 K)
0.1	$3.24 \cdot 10^{-6}$	0.93 (400-510 K)	$6.52 \cdot 10^{-3}$	1.26 (510-700 K)
0.2	$9.12 \cdot 10^{-6}$	0.93 (400-567 K)	$8.87 \cdot 10^{-3}$	1.31 (567-700 K)

The frequency dependences of the real part of dielectric permittivity (ε') of $Li_{4x}Ti_{1-x}P_2O_7$ with x = 0 and x = 0.06 are presented in Figure 4.8.4 (a) and (b), respectively. The dispersion region is observed at lower frequencies and the wide plateau was found at higher frequencies. The static value of the real part of dielectric permittivity can be obtained at frequency higher than Maxwell relaxation frequency $f_M = \sigma_{tot} / 2\pi\varepsilon'\varepsilon_0$, where $\varepsilon_0 = 8.85 \times 10^{-12}$ F/m is dielectric constant of the vacuum. These frequencies at 700 K for $Li_{4x}Ti_{1-x}P_2O_7$ ceramics with x = 0, 0.06, 0.1 and 0.2 were found to be 2.79 MHz, 83.93 MHz, 234.91 MHz and 400.63 MHz, respectively. Therefore the temperature dependences of static ε' values could be found from the measurement results and they have been obtained at 1 GHz. The temperature dependences of ε' of $Li_{4x}Ti_{1-x}P_2O_7$ (x = 0, 0.06, 0.1, 0.2) ceramics are shown in Figure 4.8.5. Static ε' of TiP_2O_7 is independent on temperature, while the values of ε' for $Li_{4x}Ti_{1-x}P_2O_7$ with x = 0.06, 0.1, and 0.2 ceramics are higher and increase with an

increase of the temperature. The temperature dependent dielectric permittivity can be explained by the contribution of Li^+ migration polarization.

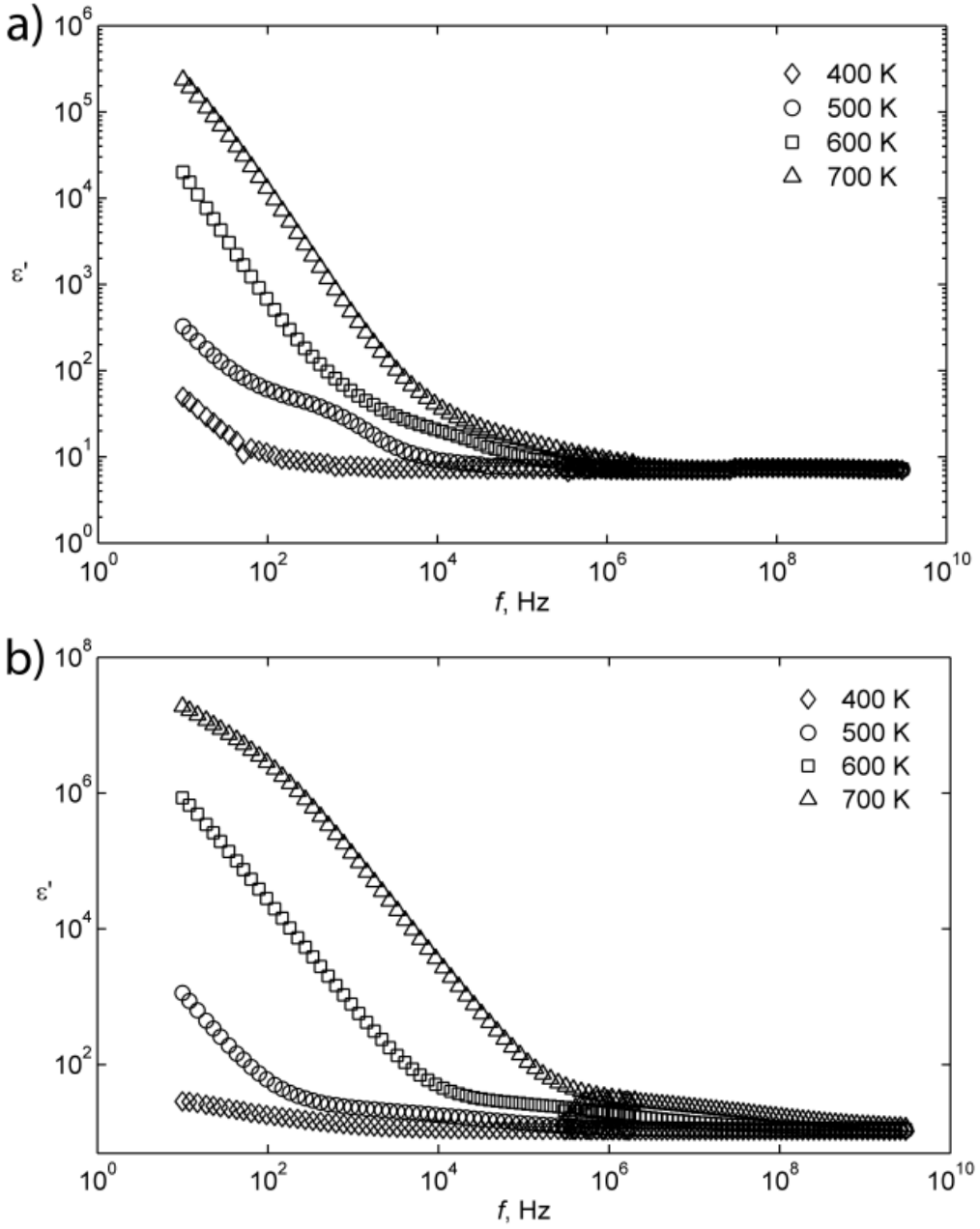

Figure 4.8.4 Frequency dependences of the real part of dielectric permittivity of TiP_2O_7 (a) and $Li_{0.24}Ti_{0.94}P_2O_7$ (b) ceramics at various temperatures.

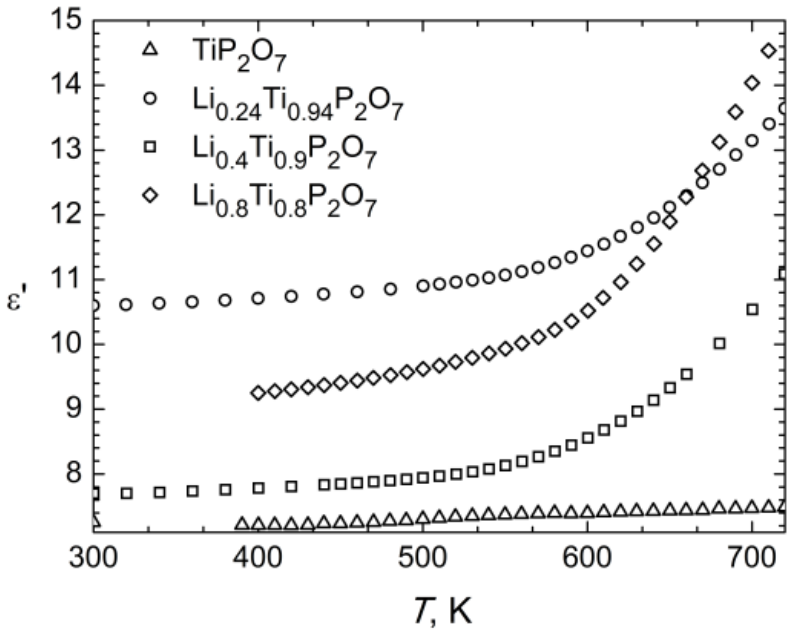

Figure 4.8.5 Temperature dependences of the real part of dielectric permittivity of $Li_{4x}Ti_{1-x}P_2O_7$ (x = 0, 0.06, 0.1, 0.2) ceramics measured at 1 GHz.

4.9. Ionic transport of $Li_4Ti_5O_{12}$, $Li_4Ti_{4.95}Nb_{0.05}O_{12}$ and $Li_4Ti_{4.95}Ta_{0.05}O_{12}$ ceramics[A7]

Electrical properties of LTO, LTO+Nb and LTO+Ta compounds were investigated in the temperature range from 300 to 780 K. The characteristic frequency dependences of the real part of complex conductivity (σ') of LTO ceramic measured at various temperatures with two and four probe methods are shown in Figure 4.9.1 Frequency dependences of the real part of complex conductivity, measured by 2- and 4-probe methods, at various temperatures.. The electrode blocking effects in low frequencies are eliminated by applying four electrode method. Two dispersion regions in conductivity spectra of all $Li_4Ti_{5-x}A_xO_{12}$ (x =0, 0.05, A = Nb, Ta) ceramics were found. The dispersion processes in investigated compounds are thermally activated and dispersion regions shift towards higher frequencies as temperature is increased. This phenomenon is typical for relaxation type dispersions. The low frequency dispersion is caused by ion transport in grain boundaries and high frequency dispersion is attributed to ion migration in grains as in [84, 94].

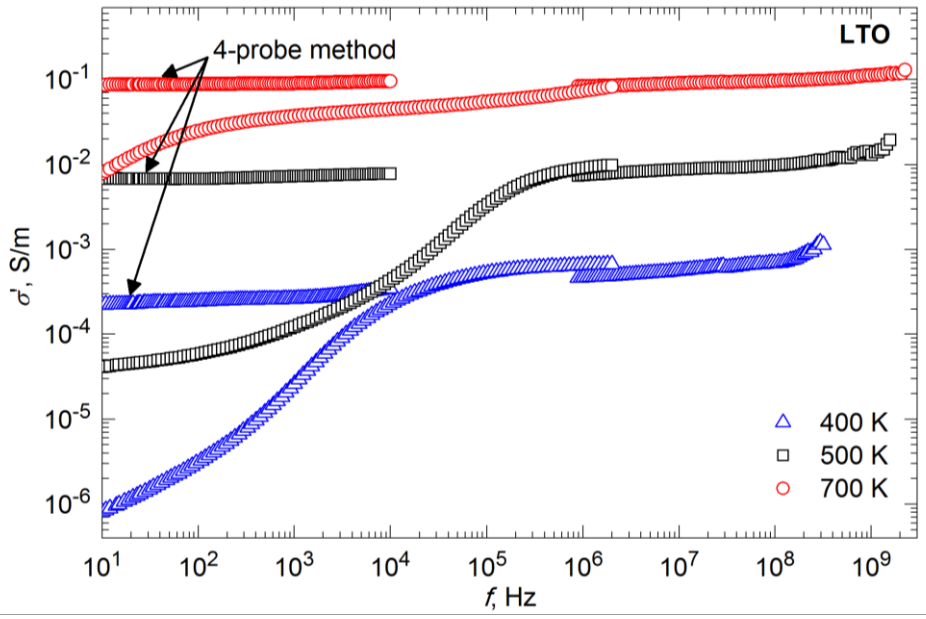

Figure 4.9.1 Frequency dependences of the real part of complex conductivity, measured by 2- and 4-probe methods, at various temperatures.

The temperature dependences of total conductivities (σ_{tot}) of the ceramics were derived from the plateau of σ'(*f*) dependences, complex impedance ρ''(ρ'), and complex conductivity σ''(σ') plots obtained at different temperatures. The characteristic σ''(σ') plot, measured with two probe method, of LTO ceramic at temperature 400 K is presented in Figure 4.9.2. The bulk conductivity (σ_b) values were derived from σ''(σ') plots.

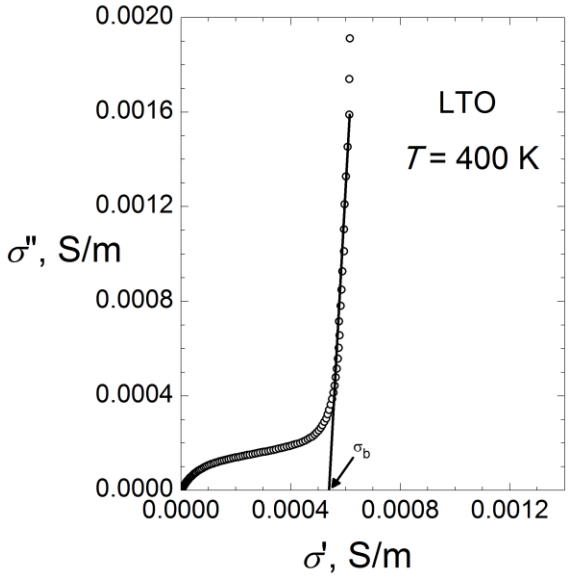

Figure 4.9.2 Characteristic complex conductivity plot at temperature 400 K for LTO ceramic.

The temperature dependences of σ_{tot} and σ_b of LTO, LTO+Nb and LTO+Ta ceramics are presented in Figure 4.9.3 a) and b). The activation energies ΔE_{tot} of σ_{tot} and ΔE_b of σ_b were found from the slopes of Arrhenius plots. The results of the measurements of σ_{tot}, σ_b at different temperatures and their activation energies of LTO, LTO+Nb and LTO+Ta ceramics are summarized in Table 4.9.1.

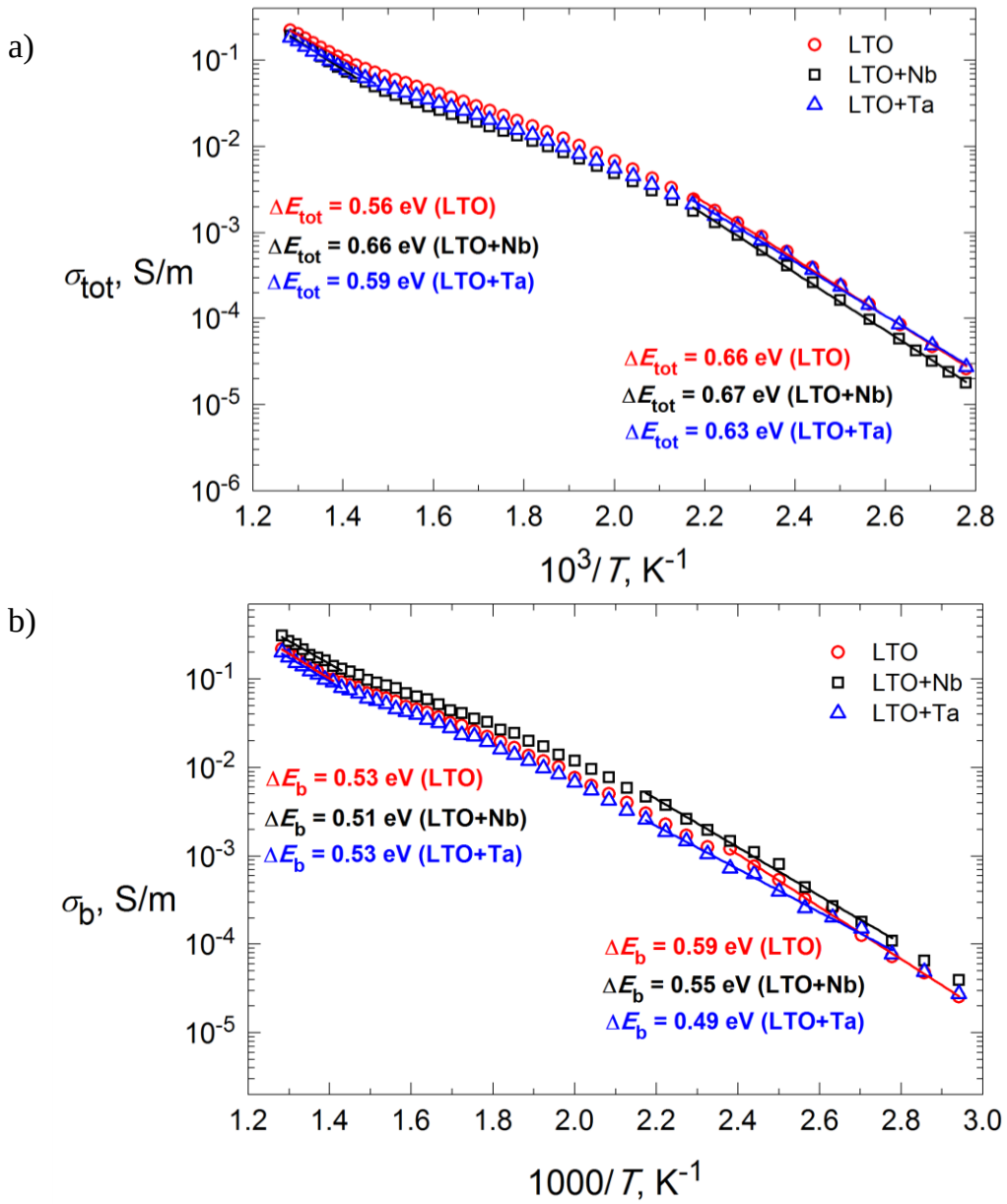

Figure 4.9.3 Temperature dependences of total conductivity a) and bulk conductivity b) of LTO, LTO+Nb, LTO+Ta ceramics.

Table 4.9.1 Summary of electrical properties (activation energies of total conductivity ΔE_{tot}, bulk conductivity ΔE_b, relaxation frequency ΔE_{fr} and total and bulk conductivities, real part of dielectric permittivity, tangent loss at temperature 400 K) investigation.

Compound	ΔE_{tot}, eV	ΔE_b, eV	ΔE_{fr}, eV	σ_{tot}, S/m (400 K)	σ_b, S/m (400 K)	ε' (400 K)	$\tan\delta$ (400 K)
LTO	0.56 (T>700 K) 0.66 (T<480 K)	0.53 (T>700 K) 0.59 (T<480 K)	0.52 (T>700 K) 0.57 (T<480 K)	$2.5\cdot10^{-4}$	$5.4\cdot10^{-4}$	22.1	$3.1\cdot10^{-4}$
LTO+Nb	0.66 (T>700 K) 0.67 (T<480 K)	0.51 (T>700 K) 0.55 (T<480 K)	0.53 (T>700 K) 0.55 (T<480 K)	$1.7\cdot10^{-4}$	$8.1\cdot10^{-4}$	24.9	$1.53\cdot10^{-3}$
LTO+Ta	0.59 (T>700 K) 0.63 (T<480 K)	0.53 (T>700 K) 0.49 (T<480 K)	0.52 (T>700 K) 0.47 (T<480 K)	$2.4\cdot10^{-4}$	$4.0\cdot10^{-4}$	22.9	$2.24\cdot10^{-3}$

The substitution of Ti^{4+} in LTO by Nb^{5+} leads the increase of the values of σ_b and decrease ΔE_b. Such substitution increases the amount of Ti^{3+} ions in the lattice (see Table 4.5.1) and it is known that this stimulates the increase of electronic conductivity part [45]. The substitution of LTO by Ta and Nb varies conductivity values only slightly, and this is in good agreement with the results of other authors, where electronic conductivity contribution to total electrical conductivity in LTO and LTO+Ta ceramics is only minor [45, 95]. In LTO, LTO+Nb and LTO+Ta ceramics at temperatures about 480 and 700 K the anomalies of σ_{tot}, σ_b and their activation energies were found. In the temperature range (480 – 700) K the σ_{tot} and σ_b changes cannot be described according to Arrhenius law. The results of XRD measurements have shown that in the temperature range (300-1270) K the lattices of investigated compounds remain cubic spinels. It is possible that detected anomalies of electrical properties are caused by different distributions of Li atoms and Li^+ vacancies in the cubic spinel type structure as previously were observed in [42, 96].

The temperature dependences of relaxation frequency (f_r) were determined from the maximum of the $\rho''(f)$ spectra measured at different temperatures. The characteristic $\rho''(f)$ spectra at temperature T = 400 K is presented in Figure 4.9.4. The maximum shifts towards high frequencies when temperature is increased. The temperature dependences of f_r are presented in Figure 4.9.5. In the same temperature range as for electrical conductivities, the anomalies of f_r and their activation energies (ΔE_{fr}) were found Table 4.9.1. The values of ΔE_{fr} and ΔE_b were similar and this suggests that charge transport in the investigated compounds may be described mainly by the temperature dependent ion mobility, while concentration of mobile Li^+ ions is independent on temperature.

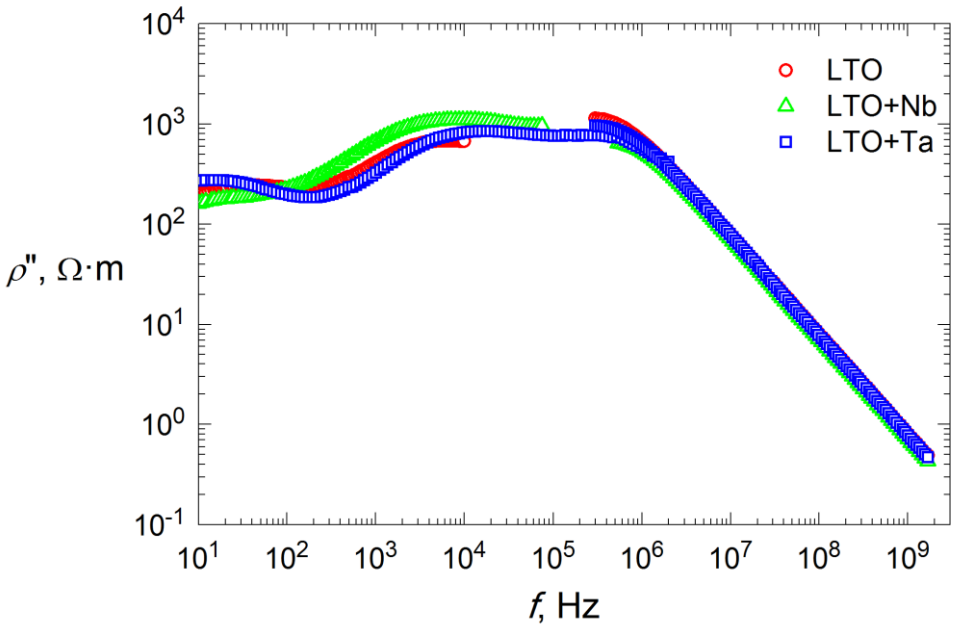

Figure 4.9.4 The frequency dependence of the imaginary part of impedance at temperature 400 K of LTO, LTO+Nb, LTO+Ta ceramics.

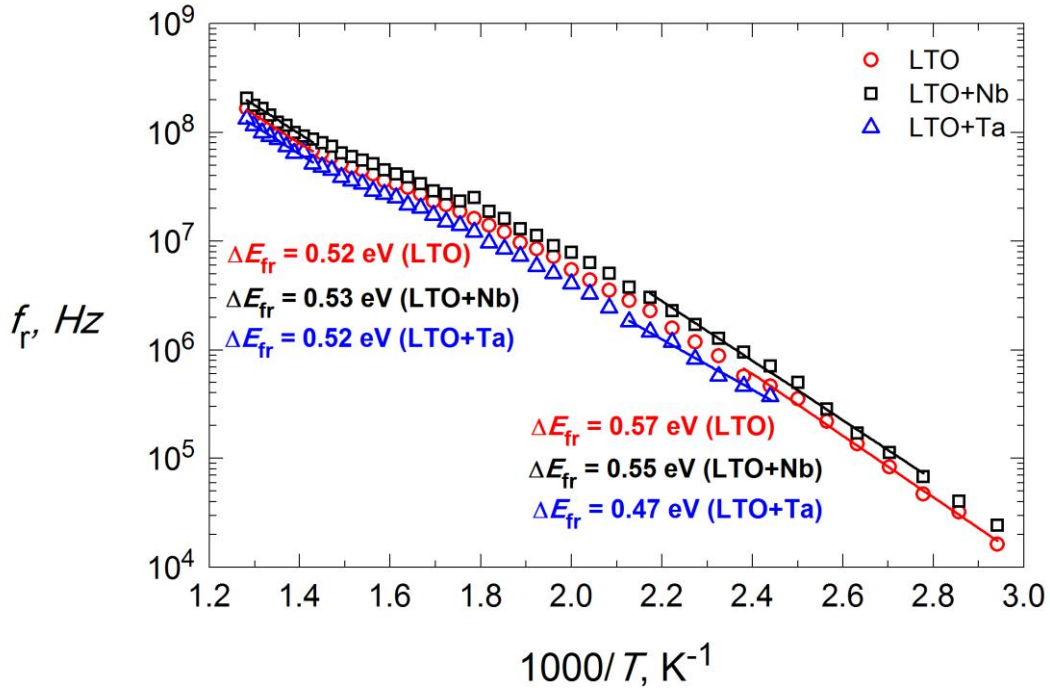

Figure 4.9.5 The temperature dependences of relaxation frequency of LTO, LTO+Nb, LTO+Ta ceramics.

The temperature dependences of the real part of dielectric permittivity (ε') and dielectric loss (tanδ) were investigated at 1 GHz frequency. This frequency at 720 K is higher than Maxwell relaxation frequency f_M =

$\sigma_{tot}/2\pi\varepsilon'\varepsilon_0$, where $\varepsilon_0 = 8.85 \times 10^{-12}$ F/m is dielectric constant of the vacuum. The calculated Maxwell relaxation frequencies at 720 K for LTO, LTO+Nb and LTO+Ta compounds are in the range (70.6-98.4) MHz. The temperature dependences of ε' and tanδ of investigated ceramics are shown in Figure 4.9.6 a) and b). The increase of ε' values with temperature can be caused by the contributions of electron polarization, vibration of the lattice and migration polarization of lithium ions in LTO, LTO+Nb and LTO+Ta. The increase of tanδ with temperature can be caused by increase of bulk conductivity in the ceramics. Substitution of LTO by Nb and Ta increase the values of ε' and tanδ (see Table 4.9.1 and Figure 4.9.6 a) and b)).

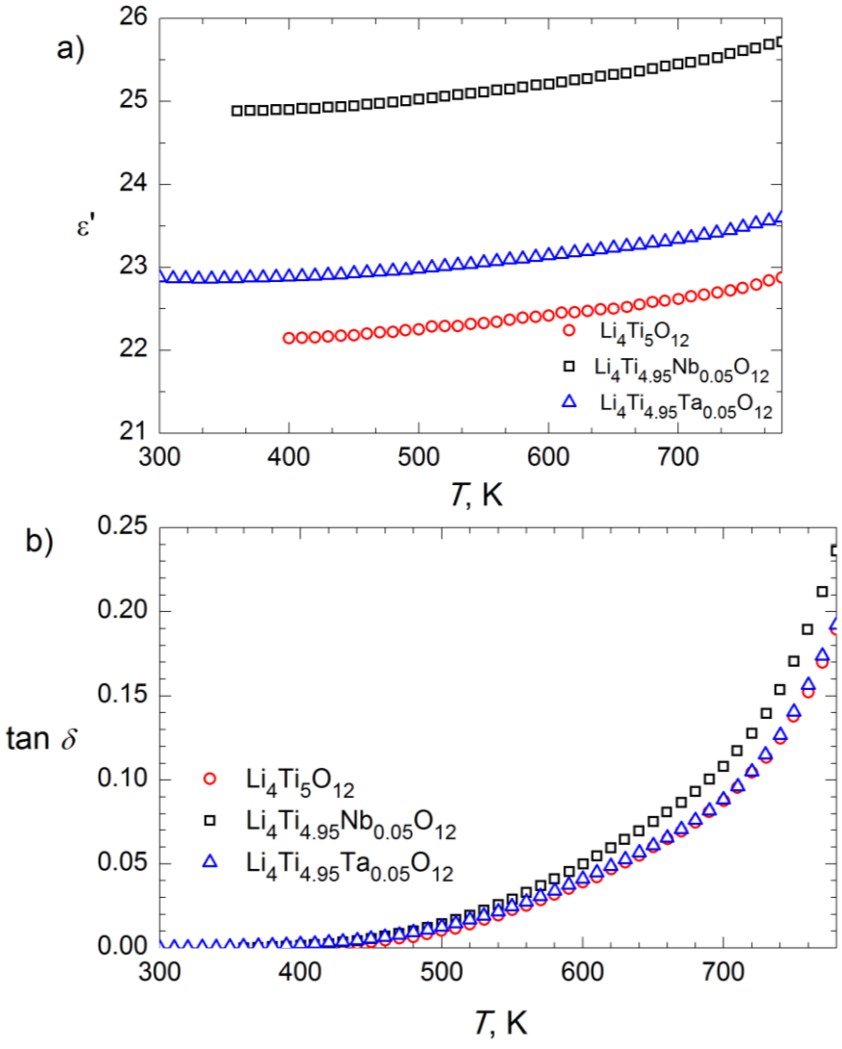

Figure 4.9.6 Temperature dependences of the real part of dielectric permitivity a) and tanδ b) at 1 GHz frequency for LTO, LTO+Nb, LTO+Ta ceramics.

4.10. Electrical properties of $LiFePO_4$ and $LiFePO_4$/C ceramics in the broad frequency range [A4].

The characteristic frequency dependences of the real part of complex conductivity (σ') of the $LiFePO_4$ ceramics measured at different temperatures are showed in Figure 4.10.1. The thermally activated dispersion regions in σ' spectra for both investigated samples were found. The dispersion regions shift towards higher frequencies as temperature increases. This phenomenon is typical for relaxation type dispersions [84, 87]. The low frequency dispersion regions can be associated with relaxation processes in the grain boundary of the ceramics. The dispersion at high frequencies is caused by ionic transport in the bulk of the ceramics.

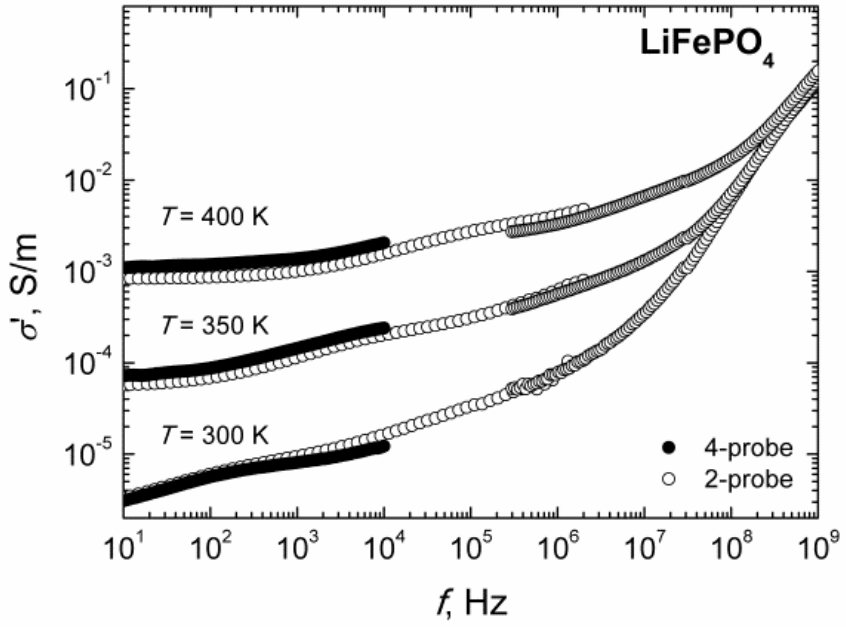

Figure 4.10.1 The characteristic frequency dependences of the conductivity of the $LiFePO_4$ ceramics at different temperatures.

Grain boundary (f_{gb}) and bulk (f_b) relaxation frequencies were determined from the maxima of the imaginary part of the complex specific resistivity ($\rho''(f)$) measured in the investigated frequency range at different temperatures. In Figure 4.10.2 the characteristic frequency dependences of ρ'' at temperatures 300, 350 and 400 K of $LiFePO_4$ compound are shown. The temperature

dependences of f_{gb} and f_b for $LiFePO_4$ ceramics and $LiFePO_4$/C composite are presented in Figure 4.10.3. The activation energies (ΔE_{fgb}) and (ΔE_{fb}) were calculated from the slopes of the Arrhenius plots of f_{gb} and f_b.

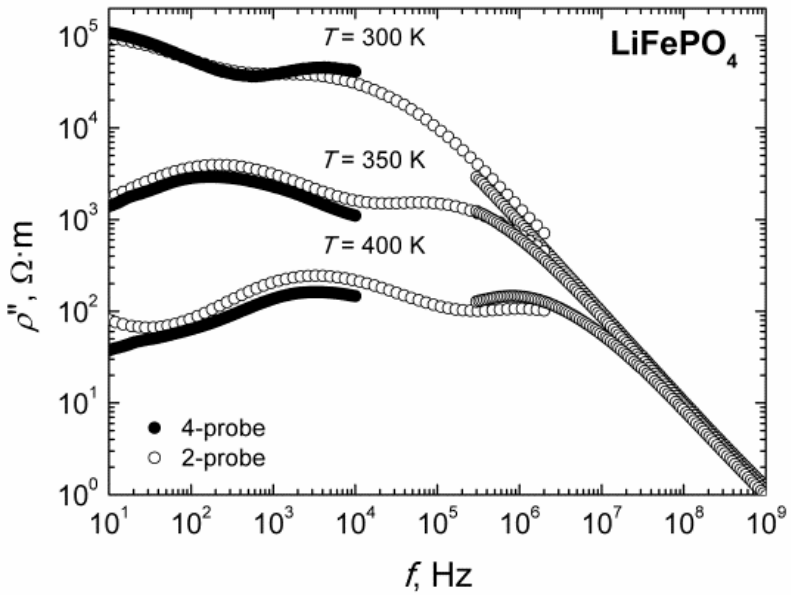

Figure 4.10.2 The characteristic frequency dependences of imaginary part of complex resistivity at different temperatures of $LiFePO_4$ ceramics.

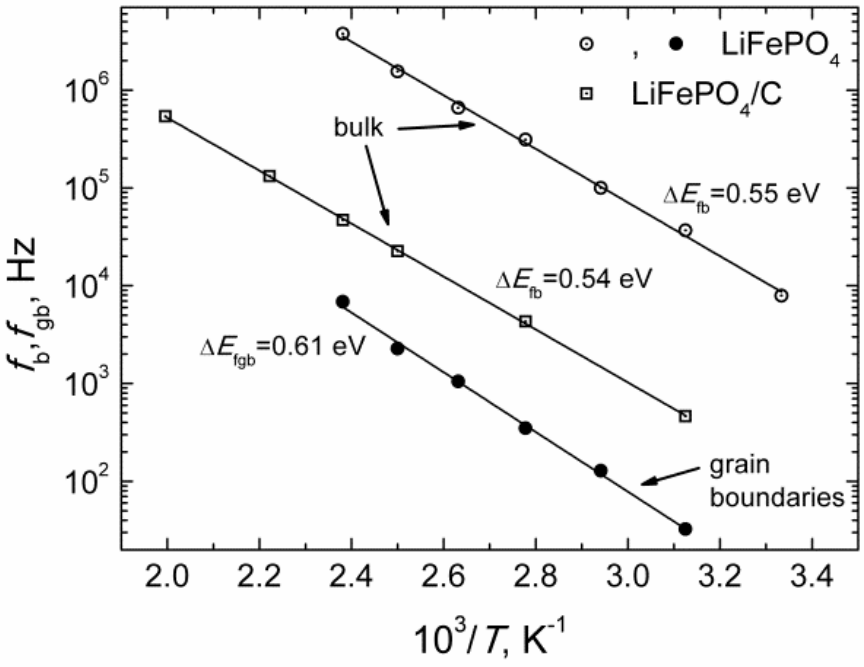

Figure 4.10.3 The temperature dependences of the relaxation frequencies in bulk and grain boundaries of $LiFePO_4$ and $LiFePO_4$/C ceramics.

The total conductivities (σ_{tot}) of the ceramics were derived from the plateaus of $\sigma'(f)$ dependences obtained by the four-probe method at different temperatures and bulk conductivities (σ_b) were obtained from complex resistivity plots ($\rho''(\rho')$) at different temperatures. The characteristic ($\rho''(\rho')$) plots of $LiFePO_4$ ceramics at different temperatures are shown in Figure 4.10.4.

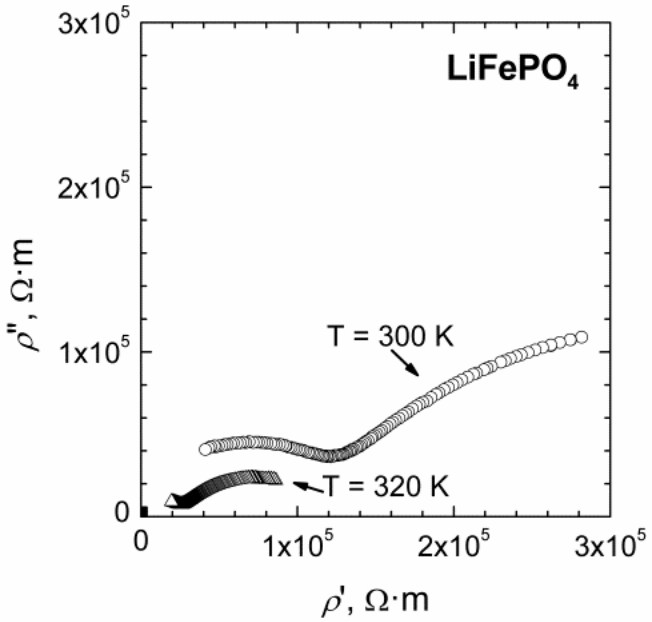

Figure 4.10.4 Impedance spectra of $LiFePO_4$ ceramics at different temperatures.

The temperature dependences of σ_{tot} and σ_b of the $LiFePO_4$ ceramic and the $LiFePO_4$/C composite samples are shown in Figure 4.10.5. The activation energies of σ_{tot} (ΔE_{tot}) and of σ_b (ΔE_b) were found from the slopes of the Arrhenius plots. The experimental results of the investigation of σ_{tot},σ_b, their activation energies are summarized in Table 4.10.1.

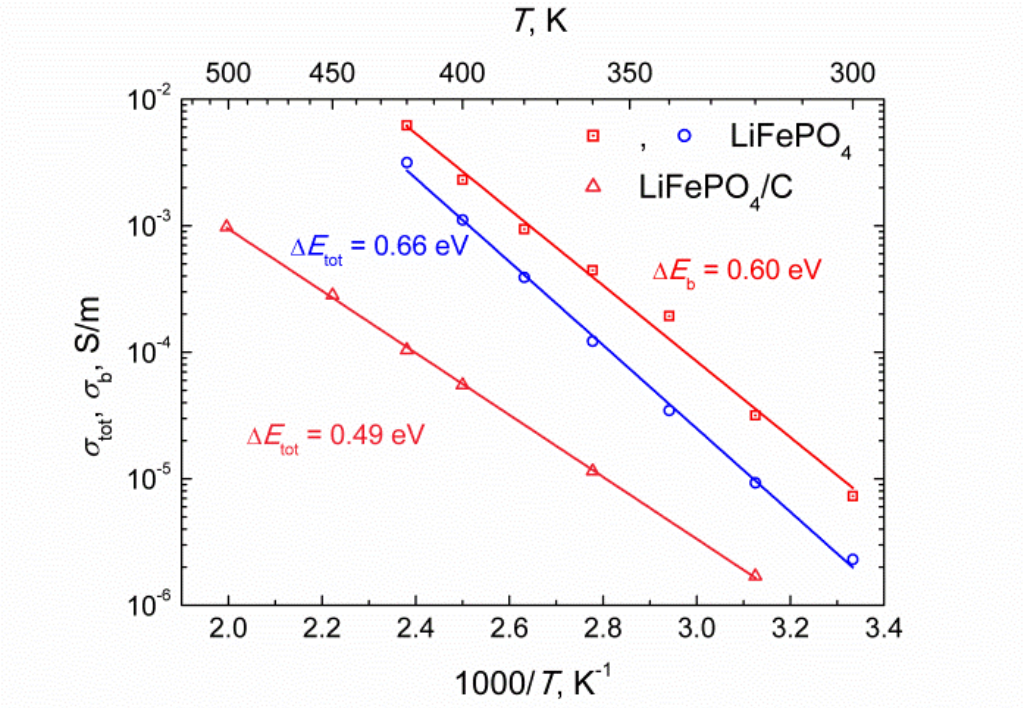

Figure 4.10.5 The temperature dependences of total and bulk conductivities of the $LiFePO_4$ and the $LiFePO_4$/C ceramics.

The temperature dependences of the dielectric permittivity (ε') and dielectric losses ($\tan\delta$) were investigated only for $LiFePO_4$ ceramic samples at 1 GHz frequency. This frequency at 420 K is higher than Maxwell relaxation frequency

$$f_M = \sigma_b / 2\pi\varepsilon'\varepsilon_0 , \qquad (4.10.1)$$

where $\varepsilon_0 = 8.85 \cdot 10^{-12}$ F/m is vacuum permittivity). The Maxwell relaxation frequency (f_M) at 420 K for $LiFePO_4$ compound was found to be 5.92 MHz. The temperature dependences of ε' and $\tan\delta$ of $LiFePO_4$ ceramics are shown in Figure 4.10.6. The values of ε' and $\tan\delta$ are summarized in Table 4.10.1 too. The increase of the ε'values with temperature can be caused by contribution of the migration polarization of lithium ions, vibration of the lattice and electronic polarization. The increase of the values of $\tan\delta$ with increase of the temperature can be related to the contribution of σ_b.

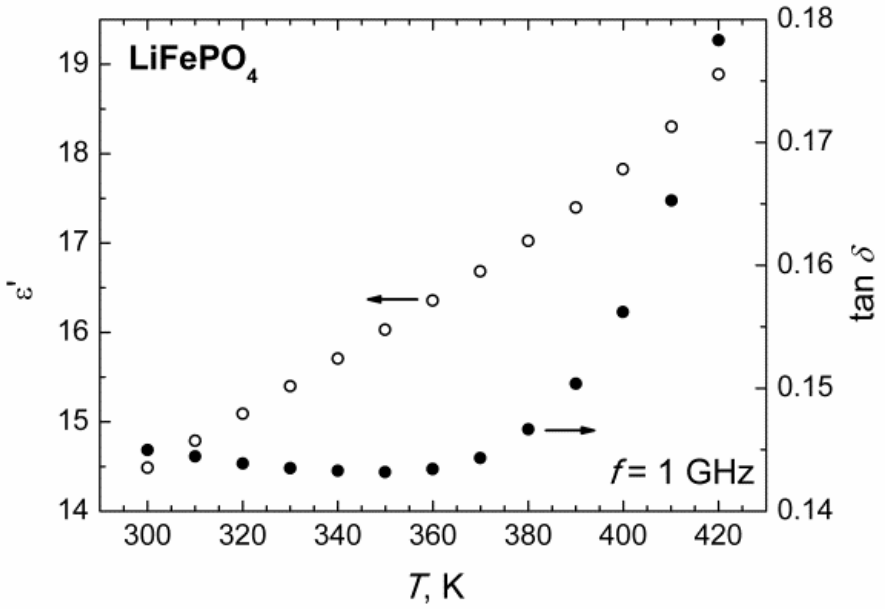

Figure 4.10.6 The temperature dependences of dielectric permittivity and tanδ of $LiFePO_4$ ceramics.

Table 4.10.1 Summary of the electrical characteristic at different temperatures for $LiFePO_4$ and $LiFePO_4$/C samples.

Compound	σ_b, S/m (320 K)	ΔE_b, eV	σ_{tot}, S/m (320 K)	ΔE_{tot}, eV	ε´ (1 GHz) (320 K)	tanδ (1GHz) (320 K)	f_M, MHz (420 K)	ΔE_{fb}, eV	ΔE_{fgb}, eV
$LiFePO_4$	$3.17 \cdot 10^{-5}$	0.60	$9.3 \cdot 10^{-6}$	0.66	15.09	0.14	5.92	0.55	0.61
$LiFePO_4$/C			$1.65 \cdot 10^{-6}$	0.49				0.54	

5. CONCLUSIONS

Lithium solid electrolytes were synthesized and their ceramics were sintered. Structural peculiarities of the compounds were investigated by X-ray diffraction technique. Surfaces of the ceramics were investigated by X-ray Photoelectron Spectroscopy, Scanning Electron Microscopy and Energy dispersive X-ray Spectroscopy. Electrical properties of the ceramics were investigated by Impedance Spectroscopy in broad frequency range. The following conclusions were obtained from the investigation:

1) X-ray diffraction analysis has shown, that a partial substitution of Al^{3+} by Y^{3+} in $Li_{1.3}Al_yY_{x-y}Ti_{1.7}(PO_4)_3$ (x = 0.3; y = 0.1, 0.2), which belongs to NASICON-type compounds, causes the increase in the lattice parameters and theoretical density of the compound. This variation can be caused by different values of the ionic radii of Y^{3+} and Al^{3+} ions.
2) The results of the investigation of electrical conductivities have shown that increase of stoichiometric parameter y in $Li_{1.3}Al_yY_{x-y}Ti_{1.7}(PO_4)_3$ (x = 0.3; y = 0, 0.1, 0.15, 0.2, 0.3) system leads to the increase of bulk conductivity (σ_b) values.
3) The partial substitution of Ti^{4+} in $Li_4Ti_5O_{12}$ by Nb^{5+} and Ta^{5+} leads the increase of amount of titanium ions in Ti^{3+}valence state and decrease the amount of ions in Ti^{4+}valence state in the ceramics surfaces.
4) The increase of the stoichiometric parameters x, y and amount of impurities $LiTiPO_5$ in the $Li_{1+4x}Ti_{2-x}Nb_yP_{3-y}O_{12}$ (x = 0.1, 0.2, 0.3; y =0, 0.1, 0.2, 0.3) compounds lead to the decrease of total and bulk conductivities and increase of their activation energies.
5) An increase of lithium content in $Li_{1+4x}Ti_{2-x}(PO_4)_3$ (where x = 0.2, 0.5) compounds leads to the increase of the volume of the lattice, decrease of the theoretical density of the compounds and increase of total and bulk electrical conductivities.
6) The changes of activation energy of σ_{tot} (ΔE_{tot}) at temperatures 550 K and at 528 K for $LiFeP_2O_7$ and $Li_{0.9}Fe_{0.9}Ti_{0.1}P_2O_7$ respectively can be

related to the structure phase transitions detected by XRD measurements.

7) The anomalies of ΔE_{tot} of $Li_{4x}Ti_{1-x}P_2O_7$ (x = 0.06, 0.1, 0.2) compounds in the temperature range from 520 to 580 K were found. The changes of ΔE_{tot} can be related to some disordering in the supercell.

REFERENCE LIST

[1] H. Aono, E. Sugimoto, Y. Sadaoka, N. Imanaka, G.-y. Adachi, *Solid State Ionics* **47** (1991) 257.

[2] P. Barpanda, S.-i. Nishimura, A. Yamada, *Advanced Energy Materials* **2** (2012) 841.

[3] J.B. Goodenough, H.Y.P. Hong, J.A. Kafalas, *Materials Research Bulletin* **11** (1976) 203.

[4] T. Salkus, I. Steins, M. Barre, A. Kezionis, A.F. Orliukas, *Mater Sci-Medzg* **19** (2013) 250.

[5] H.Y.P. Hong, *Materials Research Bulletin* **11** (1976) 173.

[6] Y. Miyajima, T. Miyoshi, J. Tamaki, M. Matsuoka, Y. Yamamoto, C. Masquelier, M. Tabuchi, Y. Saito, H. Kageyama, *Solid State Ionics* **124** (1999) 201.

[7] M.A. Subramanian, R. Subramanian, A. Clearfield, *Solid State Ionics* **18–19, Part 1** (1986) 562.

[8] H. Aono, Studies on Li+ ionic conducting solid electrolyte composed of NASICON-type structure, PhD thesis, 1994.

[9] H. Aono, E. Sugimoto, Y. Sadaoka, N. Imanaka, G. Adachi, *Solid State Ionics* **40-1** (1990) 38.

[10] H. Aono, E. Sugimoto, Y. Sadaoka, N. Imanaka, G. Adachi, *Journal of The Electrochemical Society* **137** (1990) 1023.

[11] H. Aono, E. Sugimoto, Y. Sadaoka, N. Imanaka, G.Y. Adachi, *Journal of The Electrochemical Society* **136** (1989) 590.

[12] K.D. Kreuer, H. Kohler, U. Warhus, H. Schulz, *Materials Research Bulletin* **21** (1986) 149.

[13] H.-B. Kang, N.H. Cho, *J Mater Sci* **34** (1999) 5005.

[14] R.O. Fuentes, F.M. Figueiredo, F.M.B. Marques, J.I. Franco, *Solid State Ionics* **140** (2001) 173.

[15] N.V. Kosova, D.I. Osintsev, N.F. Uvarov, E.T. Devyatkina, *Chemistry of Sustainable Development* **13** (2005) 8.

[16] Y. Kobayashi, T. Takeuchi, M. Tabuchi, K. Ado, H. Kageyama, *Journal of Power Sources* **81–82** (1999) 853.

[17] C.-M. Chang, Y.I. Lee, S.-H. Hong, H.-M. Park, *Journal of the American Ceramic Society* **88** (2005) 1803.

[18] H. Kim, S. Lee, Y.-U. Park, H. Kim, J. Kim, S. Jeon, K. Kang, *Chemistry of Materials* **23** (2011) 3930.

[19] C. Wurm, M. Morcrette, G. Rousse, L. Dupont, C. Masquelier, *Chemistry of Materials* **14** (2002) 2701.

[20] A.K. Padhi, K.S. Nanjundaswamy, C. Masquelier, S. Okada, J.B. Goodenough, *Journal of The Electrochemical Society* **144** (1997) 1609.

[21] S.-i. Nishimura, M. Nakamura, R. Natsui, A. Yamada, *Journal of the American Chemical Society* **132** (2010) 13596.

[22] H. Zhou, S. Upreti, N.A. Chernova, G. Hautier, G. Ceder, M.S. Whittingham, *Chemistry of Materials* **23** (2010) 293.

[23] D. Riou, N. Nguyen, R. Benloucif, B. Raveau, *Materials Research Bulletin* **25** (1990) 1363.
[24] D. Tran Qui, S. Hamdoune, Y. Le Page, *Acta Crystallographica Section C* **43** (1987) 201.
[25] Y. Uebou, S. Okada, M. Egashira, J.-I. Yamaki, *Solid State Ionics* **148** (2002) 323.
[26] Ģ. Vītiņš, Z. Kaņepe, A. Vītiņš, J. Ronis, A. Dindūne, A. Lūsis, *Journal of Solid State Electrochemistry* **4** (2000) 146.
[27] L. Adam, A. Guesdon, B. Raveau, *Journal of Solid State Chemistry* **181** (2008) 3110.
[28] M. Tamaru, S.C. Chung, D. Shimizu, S.-i. Nishimura, A. Yamada, *Chemistry of Materials* **25** (2013) 2538.
[29] І.В. Затовський, *Reports of the National Academy of Sciences of Ukraine* **11** (2008) 5.
[30] Y. Uebou, S. Okada, M. Egashira, J.-I. Yamaki, *The Reports of Institute of Advanced Material Study, Kyushu University* **15** (2001) 5.
[31] S.T. Norberg, G. Svensson, J. Albertsson, *Acta Crystallographica Section C* **57** (2001) 225.
[32] H. Wang, K. Huang, Y. Zeng, S. Yang, L. Chen, *Electrochimica Acta* **52** (2007) 3280.
[33] N.G. Chernorukov, M.I. Zhuk, E.P. Moskvichev, *Trudy po Khimii i Khimicheskoi Tekhnologii* (1974) 2.
[34] V. Nalini, M.H. Sørby, K. Amezawa, R. Haugsrud, H. Fjellvåg, T. Norby, *Journal of the American Ceramic Society* **94** (2011) 1514.
[35] C.H. Kim, H.S. Yim, *Solid State Communications* **110** (1999) 137.
[36] V. Nalini, R. Haugsrud, T. Norby, *Solid State Ionics* **181** (2010) 510.
[37] Е.А. Генкина, Б.А. Максимов, В.А. Тимофеева, А.Б. Быков, О.К. Мельников, *Доклады Академии наук СССР. Кристаллография* **284** (1985) 4.
[38] C.M. Julien, K. Zaghib, *Electrochimica Acta* **50** (2004) 411.
[39] T. Ohzuku, A. Ueda, N. Yamamoto, *Journal of The Electrochemical Society* **142** (1995) 1431.
[40] K. Zaghib, M. Simoneau, M. Armand, M. Gauthier, *Journal of Power Sources* **81–82** (1999) 300.
[41] K.T. Fehr, M. Holzapfel, A. Laumann, E. Schmidbauer, *Solid State Ionics* **181** (2010) 1111.
[42] I.A. Leonidov, O.N. Leonidova, L.A. Perelyaeva, R.F. Samigullina, S.A. Kovyazina, M.V. Patrakeev, *Phys. Solid State* **45** (2003) 2183.
[43] C.Y. Ouyang, Z.Y. Zhong, M.S. Lei, *Electrochemistry Communications* **9** (2007) 1107.
[44] T.-F. Yi, L.-J. Jiang, J. Shu, C.-B. Yue, R.-S. Zhu, H.-B. Qiao, *Journal of Physics and Chemistry of Solids* **71** (2010) 1236.
[45] J. Wolfenstine, J.L. Allen, *Journal of Power Sources* **180** (2008) 582.
[46] A.K. Padhi, K.S. Nanjundaswamy, J.B. Goodenough, *Journal of The Electrochemical Society* **144** (1997) 1188.
[47] B. Wu, Y. Ren, N. Li, *LiFePO4 Cathode Material* (2011).

[48] J. Li, W. Yao, S. Martin, D. Vaknin, *Solid State Ionics* **179** (2008) 2016.
[49] D. Morgan, A. Van der Ven, G. Ceder, *Electrochem. Solid-State Lett.* **7** (2004) A30.
[50] C. Wang, J. Hong, *Electrochemical and Solid-State Letters* **10** (2007) A65.
[51] S.-Y. Chung, J.T. Bloking, Y.-M. Chiang, *Nat Mater* **1** (2002) 123.
[52] F. Kremmer, A. Schonhals, *Broadband Dielectric Spectroscopy*, Springer-Verlag Berlin Heidelberg (2003).
[53] E. Barsoukov, J.R. Macdonald, *Impedance Spectroscopy: Theory, Experiment, and Applications*, John Wiley & Sons, Inc., Hoboken, New Jersey (2005).
[54] A. Kežionis, E. Kazakevičius, T. Šalkus, A. Orliukas, *Solid State Ionics* **188** (2011) 110.
[55] A. Kezionis, P. Butvilas, T. Salkus, S. Kazlauskas, D. Petrulionis, T. Zukauskas, E. KazakeviCius, A.F. Orliukas, *Review of Scientific Instruments* **84** (2013) 013902.
[56] R. Shannon, *Acta Crystallographica Section A* **32** (1976) 751.
[57] A. Dindune, Z. Kanepe, E. Kazakevičius, A. Kežionis, J. Ronis, A. Orliukas, *Journal of Solid State Electrochemistry* **7** (2003) 113.
[58] T. Salkus, E. Kazakevicius, A. Kezionis, V. Kazlauskiene, J. Miskinis, A. Dindune, Z. Kanepe, J. Ronis, M. Dudek, M. Bucko, J.R. Dygas, W. Bogusz, A.F. Orliukas, *Ionics* **16** (2010) 631.
[59] H. Bih, I. Saadoune, H. Ehrenberg, H. Fuess, *Journal of Solid State Chemistry* **182** (2009) 821.
[60] L.K. Elbouaanani, B. Malaman, R. Gérardin, *Journal of Solid State Chemistry* **148** (1999) 455.
[61] P. Sébastien, M. Christian, *Chemistry of Materials* **14** (2002) 5057.
[62] Q.-H. Wu, J.-M. Xu, Q.-C. Zhuang, S.-G. Sun, *Solid State Ionics* **177** (2006) 1483.
[63] B.V.R. Chowdari, G.V. Subba Rao, G.Y.H. Lee, *Solid State Ionics* **136–137** (2000) 1067.
[64] J.-Y. Luo, L.-J. Chen, Y.-J. Zhao, P. He, Y.-Y. Xia, *Journal of Power Sources* **194** (2009) 1075.
[65] Q. Xu, D.-p. Huang, W. Chen, H. Wang, B.-t. Wang, R.-z. Yuan, *Applied Surface Science* **228** (2004) 110.
[66] I.V. Sieber, H. Hildebrand, S. Virtanen, P. Schmuki, *Corrosion Science* **48** (2006) 3472.
[67] J. Światowska-Mrowiecka, S. de Diesbach, V. Maurice, S. Zanna, L. Klein, E. Briand, I. Vickridge, P. Marcus, *The Journal of Physical Chemistry C* **112** (2008) 11050.
[68] M.S. Bhuvaneswari, S. Selvasekarapandian, S. Fujihara, S. Koji, *Solid State Ionics* **177** (2006) 121.
[69] A. Robertson, J.G. Fletcher, J.M.S. Skakle, A.R. West, *Journal of Solid State Chemistry* **109** (1994) 53.

[70] T. Šalkus, A. Kežionis, V. Kazlauskienė, J. Miškinis, A. Dindune, Z. Kanepe, J. Ronis, A.F. Orliukas, *Materials Science and Engineering: B* **172** (2010) 156.
[71] V. Simon, D. Eniu, A. Takacs, K. Magyari, M. Neumann, S. Simon, *Journal of Optoelectronics and Advanced Materials* **7** (2005) 5.
[72] S.A. Barve, Jagannath, N. Mithal, M.N. Deo, N. Chand, B.M. Bhanage, L.M. Gantayet, D.S. Patil, *Surface and Coatings Technology* **204** (2010) 3167.
[73] G.S.A.M. Theunissen, A.J.A. Winnubst, A.J. Burggraaf, *J Mater Sci* **27** (1992) 5057.
[74] X.-G. Wang, *Surface Science* **602** (2008) L5.
[75] C.-W. Cheng, E.A. Fitzgerald, *Applied Physics Letters* **93** (2008) 031902.
[76] R.J. Iwanowski, M. Heinonen, I. Pracka, J. Raczyńska, K. Fronc, J.W. Sobczak, *Journal of Alloys and Compounds* **286** (1999) 162.
[77] B.-E. Jun, C.-S. Kim , H.-K. Kim, J.-N. Kim, Y.-H. Hwang, *Journal of Korean Physical Society* **46** (2005) 3.
[78] L. Shi, X. Hu, Y. Huang, *J Nanopart Res* **16** (2014) 1.
[79] J. Liu, S. Cheng, M. Liao, M. Imura, A. Tanaka, H. Iwai, Y. Koide, *Diamond and Related Materials* **38** (2013) 24.
[80] A.P. Grosvenor, B.A. Kobe, M.C. Biesinger, N.S. McIntyre, *Surface and Interface Analysis* **36** (2004) 1564.
[81] M. Manickam, P. Singh, S. Thurgate, K. Prince, *Journal of Power Sources* **158** (2006) 646.
[82] M. Mullet, Y. Guillemin, C. Ruby, *Journal of Solid State Chemistry* **181** (2008) 81.
[83] R. Sobiestianskas, A. Dindune, Z. Kanepe, J. Ronis, A. Kežionis, E. Kazakevičius, A. Orliukas, *Materials Science and Engineering: B* **76** (2000) 184.
[84] W. Bogusz, J.R. Dygas, F. Krok, A. Kezionis, R. Sobiestianskas, E. Kazakevicius, A. Orliukas, *physica status solidi (a)* **183** (2001) 323.
[85] M. Gödickemeier, B. Michel, A. Orliukas, P. Bohac, K. Sasaki, L.J. Gauckler, H. Heinrich, P. Schwander, G. Kostorz, a. Hofmann et, *J. Mater. Res.* **9** (1994) 1228.
[86] T. Šalkus, A. Dindune, Z. Kanepe, J. Ronis, A. Určinskas, A. Kežionis, A.F. Orliukas, *Solid State Ionics* **178** (2007) 1282.
[87] M. Cretin, P. Fabry, *Journal of the European Ceramic Society* **19** (1999) 2931.
[88] A.F. Orliukas, T. Šalkus, A. Dindune, Z. Kanepe, J. Ronis, A. Určinskas, E. Kazakevičius, A. Kežionis, V. Kazlauskienė, J. Miškinis, *Solid State Ionics* **179** (2008) 159.
[89] A.F. Orliukas, A. Dindune, Z. Kanepe, J. Ronis, B. Bagdonas, A. Kežionis, *Electrochimica Acta* **51** (2006) 6194.
[90] A.F. Orliukas, O. Bohnke, A. Kežionis, S. Kazlauskas, V. Venckutė, D. Petrulionis, T. Žukauskas, T. Šalkus, A. Dindune, Z. Kanepe, J. Ronis, V. Kunigėlis, *Advanced Electromagnetics* **1** (2012) 6.

[91] A.F. Orliukas, T. Šalkus, A. Kežionis, A. Dindune, Z. Kanepe, J. Ronis, V. Venckutė, V. Kazlauskienė, J. Miškinis, A. Lukauskas, *Solid State Ionics* **225** (2012) 620.
[92] A. Orliukas, R. Vaitkus, A. Kezionis, S. Aukselis, *Solid State Ionics* **40–41, Part 1** (1990) 158.
[93] T. Salkus, O. Bohnke, J. Macutkevic, A.F. Orliukas, S. Greicius, A. Kezionis, A. Krotkus, R. Suzanoviciene, R. Adomavicius, *Phys Status Solidi C* **6** (2009) 2756.
[94] A.F. Orliukas, V. Venckute, J. Miskinis, V. Kazlauskiene, D. Petrulionis, T. Salkus, A. Dindune, Z. Kanepe, J. Ronis, T. Zukauskas, A. Maneikis, A. Kezionis, *Lithuanian Journal of Physics* **53** (2013) 244.
[95] B. Tian, H. Xiang, L. Zhang, Z. Li, H. Wang, *Electrochimica Acta* **55** (2010) 5453.
[96] X. Lu, L. Zhao, X. He, R. Xiao, L. Gu, Y.-S. Hu, H. Li, Z. Wang, X. Duan, L. Chen, J. Maier, Y. Ikuhara, *Advanced Materials* **24** (2012) 3233.